ABSTRACT

INTERACTION OF A VORTEX PAIR AND A FREE-SURFACE: NUMERICAL SIMULATIONS

by
Haisheng Ruan

The interaction between a submerged vortex pair with a deformable free-surface in a viscous, incompressible fluid is directly simulated and the flow is thoroughly analyzed. This is a time-dependent nonlinear free-surface problem which we solve numerically by integrating the two-dimensional Navier-Stokes equations and using boundary-fitted coordinates capable of handling large free-surface deformations. In particular, the numerical simulation of the flow at relatively high Reynolds numbers ($Re = 500, 1000, 2000$) and relatively high Froude numbers (Fr = 1.125, Fr = 2.0) is investigated and analyzed for the first time. Details are given regarding the space-time deformation of the free-surface, the path of the primary vortices, the formation of strong free-surface vorticity and kinetic energy, and the generation of turbulence in the flow. In particular, the turbulence characteristics have been explored at Reynolds number Re = 1000. In this flow, we identified a thin free-surface layer characterized by very fast variations of the turbulence intensity, the kinetic energy dissipation and velocity fluctuations. The turbulence intensity reaches a maximum at the level of the center of the primary vortex, and then decreases significantly as the free-surface is approached. This decay is due to a very large increase of the turbulent kinetic energy dissipation at the free-surface and the formation of large vorticity peaks at the free-surface. Contrarily to previous findings, there is no redistribution of the turbulence intensity at the free-surface, that is a large increase of the horizontal velocity fluctuation at the expense of the vertical velocity fluctuation. Instead, the horizontal velocity fluctuation is smaller than the

vertical velocity fluctuation. This is due to the fact that our Froude number is relatively large and that the free-surface undergoes large (particularly vertical) deformations, as permitted by our numerical scheme, as the primary vortices approach the free-surface.

INTERACTION OF A VORTEX PAIR AND A FREE-SURFACE: NUMERICAL SIMULATIONS

by
Haisheng Ruan

A Dissertation
Submitted to the Faculty of
New Jersey Institute of Technology
In Partial Fulfillment of the Requirements for the Degree of
Doctor of Philosophy in Mechanical Engineering

Department of Mechanical Engineering

May 2000

APPROVAL PAGE

INTERACTION OF A VORTEX PAIR AND A FREE-SURFACE: NUMERICAL SIMULATIONS

Haisheng Ruan

Dr. Nadine Aubry, Dissertation Advisor — Date
Professor/Jacobus Chair of Mechanical Engineering
Professor of Mathematical Sciences, NJIT

Dr. Demetrius T. Papageorgiou, Committee Member — Date
Associate Professor of Mathematical Sciences, NJIT

Dr. Anthony D. Rosato, Committee Member — Date
Associate Professor of Mechanical Engineering, NJIT

Dr. Pushpendra Singh, Committee Member — Date
Assistant Professor of Mechanical Engineering, NJIT

Dr. Chao Zhu, Committee Member — Date
Assistant Professor of Mechanical Engineering, NJIT

BIOGRAPHICAL SKETCH

Author: Haisheng Ruan

Degree: Doctor of Philosophy in Mechanical Engineering

Date: May 2000

Undergraduate and Graduate Education:

- Doctor of Philosophy in Mechanical Engineering,
  New Jersey Institute of Technology, Newark, NJ, 2000

- Master of Science in Mechanical Engineering,
  The City College of New York/City University of New York, New York, NY, 1995

- Bachelor of Science in Physics,
  University of Science and Technology of China, Hefei, P. R. China, 1969

Major: Mechanical Engineering

This dissertation is dedicated to my parents
and my grandmother

ACKNOWLEDGEMENT

I would like to express my deepest appreciation to Dr. Nadine Aubry, who not only served as my research supervisor, providing valuable guidance, insight and resources, but also gave me support, encouragement, self-confidence and strength.

I would also like to thank Dr. George S. Triantafyllou for his support and advice during my studies at the Benjamin Levich Institute, the City College of the City University of New York.

Special thanks are given to Dr. Demetrius T. Papageogiou, Dr. Anthony D. Rosato, Dr. Pushpendra Singh and Dr. Chao Zhu for serving as committee members.

I wish to thank Ms. Sharyn Serafin for her assistance in the formatting of this dissertation.

TABLE OF CONTENTS

TABLE OF CONTENTS
(Continued)

LIST OF FIGURES

LIST OF FIGURES
(Continued)

Figure **Page**

LIST OF FIGURES
(Continued)

LIST OF FIGURES
(Continued)

LIST OF SYMBOLS

a	the initial distance between the two vortices
g	gravitational acceleration
h	initial depth of the vortex pair ($h = 3a$ in this work)
κ	vortex strength
ν	kinematic viscosity
Re	Reynolds number
Fr	Froude number
V_0	initial translational velocity of the vortices
ρ	density of the fluid
p	pressure
u, v	velocity components
ξ, η	computational-space coordinates
x, y	physical-space coordinates
J	Jacobian of the coordinate transformation
$Y(x,t)$	free surface elevation
$\vec{\zeta}$	vorticity
r	distance between observer and source
t	time
δ_{ij}	Kronecker delta symbol, $\delta_{ij} = 1$ if $i = j$, otherwise $\delta_{ij} = 0$
u_i	velocity components in tensor notation
Γ	circulation
$\tilde{\eta}$	self-similarity variable, $\tilde{\eta} = r(\nu t)^{-1/2}$

LIST OF SYMBOLS
(Continued)

P^*, Q^*	coordinate-system control functions for adaptive gridding
w_1, w_2	weight functions used to determine the control functions P^*, Q^*
$\vec{u}$	velocity vector
$\overline{u}$	mean velocity
q	norm of the velocity $\vec{u}$, $q = \sqrt{u^2 + v^2}$
$\tilde{f}$	function of self-similarity variable $\tilde{\eta}$, $\tilde{f} = \tilde{f}(\tilde{\eta})$
ζ	vorticity component in the z-direction
ζ_i	vorticity components in tensor notation
x_i	coordinates in tensor notation

CHAPTER 1

INTRODUCTION

Recently, the study of the interaction between vortices and a free-surface has been strongly motivated by the need to gain a physical understanding of the flow around ships and submarines as they approach the free-surface. From a practical point of view, such a need is motivated by the interpretation of experimental data from remote sensing of ship and submarine wakes. In particular, the fundamental problem of a two-dimensional vortex pair (two counter-rotating vortices of equal strength) interacting with a free-surface has become of great interest. Such approach is motivated by experimental studies of wave signatures at a water-air interface caused by the vortex-induced wake of a ship (Sarpkaya & Henderson (1984); Willmarth *et al.*(1989)). Another area of interest is free-surface turbulence in which vortex pairs can develop spontaneously, travel with great speed, and carry mass and momentum over significant distances. It is crucial to understand and predict the effect of the presence of a free-surface on the traveling speed and transport properties of vortices, as well as on the generation of new flow structures.

Other experimental works include those of Barker and Crow (1977) and Sarpkaya *et al.* (1984). While Barker and Crow (1977) studied the motion of vortex pairs near a water-air surface, they did not give any information on the deformation of the free-surface. Experiments explicitly designed for this purpose were performed later by Sarpkaya *et al.* (1984) with underwater vortices generated by a moving hydrofoil. They observed two types of straight, sharp surface depressions, which they named 'scars' and 'striations'. While scars are perpendicular to the hydrofoil's motion, striations are parallel. In addition, Sarpkaya *et al.* (1988) and Christian and Morteza (1997) used counter-rotating flaps to generate vortices. Of particular interest to the present work are the findings of Christian and Morteza (1997) who investigated High Reynolds number flows (up to $Re \sim 8000$).

In contrast, numerical simulations dealing with fully non-linear free-surface deformations have been limited to Reynolds numbers smaller than or equal to $Re = 100$ (Samuel and Hans, 1991). Attempts to compute the flow at higher Reynolds numbers have been made. In many cases, however, the surface boundary conditions are greatly simplified. Most of these investigations use the "rigid lid" or "free-slip" approximation of the free-surface, i.e. a flat surface with zero stresses but also zero normal velocity. This corresponds to the limit of zero Froude number. For instance, J. F. Garten *et al.* discussed the dynamics of counter-rotating vortex pairs in stratified and sheared environments at relatively high Reynolds number values ($Re = 1500$), but their free-surface boundary conditions were either periodic or stress-free with zero normal vorticity, thus preventing both free-surface deformations and complex interface/fluid flow interactions. Another type of flow studied numerically in the past is the flow between a rigid (no-slip) wall and a free slip plate, a model for the open-channel flow. Approximation of the free surface by a flat slip-free plate, corresponding to the zero Froude number limit, has been used extensively in numerical simulations (Lam and Banerjee (1988), Handler *et al.* (1991), Leighton *et al.* (1991), Swean *et al.* (1991), Handler *et al.* (1993), Pan and Banerjee (1995), Perot and Moin (1995), Walker *et al.* (1996), among others). In particular, Leighton *et al.* (1991) investigate the interaction of vorticity with the free surface and propose two models, the "spin" model and the "splat" model, which follow a description by Bradshaw and Koh (1981). More recently, the extension of numerical simulations to non-zero (but still small) Froude numbers has been considered by Borue *et al.* (1995) and Shen *et al.* (1999), although these works both use linearized free surface motions, thus assuming that the free-surface elevation remains small during the flow dynamics.

The goal of the present work is to investigate the full interaction between an incompressible, viscous vortex pair and the *nonlinear deformations of the free-surface*, at higher Reynolds numbers and Froude numbers than those investigated numerically in the past. Although the vortices decay in strength, the flow dynamics is quite complex partly due to the fact that the vortices lead to large free-surface deformations during their approach.

The present numerical scheme is based on the Navier-Stokes equations and uses boundary-fitted coordinates to accommodate both the local high vorticity generated by the moving vortices and the nonlinear deformation of the free-surface. The numerical scheme is explained in details. In particular, we found that a fully implicit numerical scheme is desirable and that it is crucial to carefully select numerical parameters, especially for flows at high Reynolds and Froude numbers. In this work, we have performed flow simulations at various Reynolds numbers up to $Re = 2000$ and various Froude numbers up to $Fr = 3.0$.

A comparison of our results with other researchers' numerical findings was performed at low Reynolds number values while available experimental data were used at both low and high Reynolds numbers, whenever possible.

CHAPTER 2

FORMULATION OF THE PROBLEM

2.1 Mathematical Formulation of the Physical Problem: Governing Equations

A pair of point vortices of equal strength κ but opposite sign are initially located at points $(\pm a/2, h)$ in an incompressible Newtonian fluid with a free-surface. Hereafter, V_0 denotes the initial translational velocity of the vortices and p the scaled dynamic pressure. Figure 1 represents a sketch of the flow. If the fluid has density ρ and kinematic viscosity ν, we choose a, $a^2/\kappa(=a/V_0)$, $\kappa/a(=V_0)$, $\rho(\kappa^2/a^2)(p-y/Fr^2)$, as characteristic length, time, velocity and pressure, respectively. The dimensionless governing differential equations can then be written as:

$$\frac{\partial u}{\partial t}+u\frac{\partial u}{\partial x}+v\frac{\partial u}{\partial y}=-\frac{\partial p}{\partial x}+\frac{1}{Re}\left(\frac{\partial^2 u}{\partial x^2}+\frac{\partial^2 u}{\partial y^2}\right) \tag{2.1}$$

$$\frac{\partial v}{\partial t}+u\frac{\partial v}{\partial x}+v\frac{\partial v}{\partial y}=-\frac{\partial p}{\partial y}+\frac{1}{Re}\left(\frac{\partial^2 v}{\partial x^2}+\frac{\partial^2 v}{\partial y^2}\right) \tag{2.2}$$

$$\frac{\partial u}{\partial x}+\frac{\partial v}{\partial y}=0 \tag{2.3}$$

or, in conservative form,

$$\frac{\partial u}{\partial t}+\frac{\partial (u)^2}{\partial x}+\frac{\partial (uv)}{\partial y}=-\frac{\partial p}{\partial x}+\frac{1}{Re}\left(\frac{\partial^2 u}{\partial x^2}+\frac{\partial^2 u}{\partial y^2}\right) \tag{2.4}$$

$$\frac{\partial v}{\partial t}+\frac{\partial (uv)}{\partial x}+\frac{\partial (v)^2}{\partial y}=-\frac{\partial p}{\partial y}+\frac{1}{Re}\left(\frac{\partial^2 v}{\partial x^2}+\frac{\partial^2 v}{\partial y^2}\right) \tag{2.5}$$

$$\frac{\partial u}{\partial x} + \frac{\partial v}{\partial y} = 0 \tag{2.3}$$

where the Reynolds number is defined as

$$\mathrm{Re} = \frac{\frac{\kappa}{a} \cdot a}{\nu} = \frac{\kappa}{\nu}.$$

The other dimensionless parameter involved in the problem is Froude number, Fr, which can be written as

$$Fr = \frac{\kappa/a}{(ga)^{\frac{1}{2}}} = \frac{\kappa}{(ga^3)^{\frac{1}{2}}}.$$

It will appear in the expression of the boundary conditions specified below.

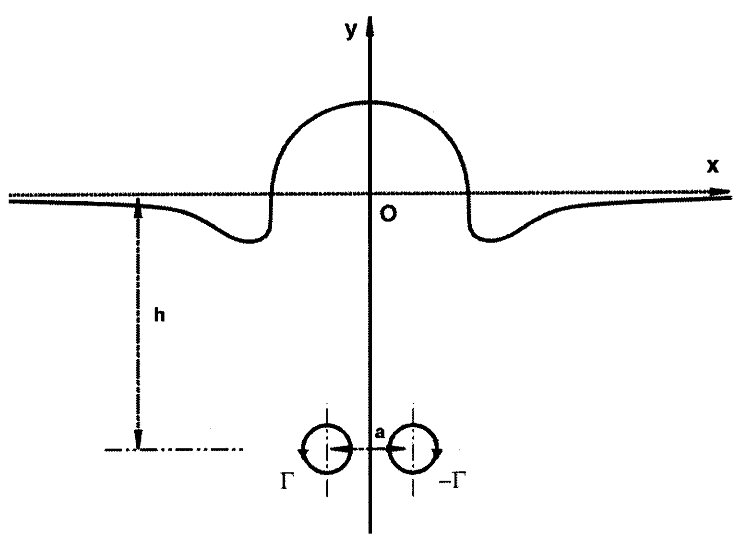

Figure 1. Sketch of the flow.

Using boundary-fitted coordinates, the physical space (x, y) is mapped onto the computational domain (ξ,η) as shown in Figure 2. The latter is a uniformly spaced Cartesian mesh with a unit mesh spacing in each coordinate direction.

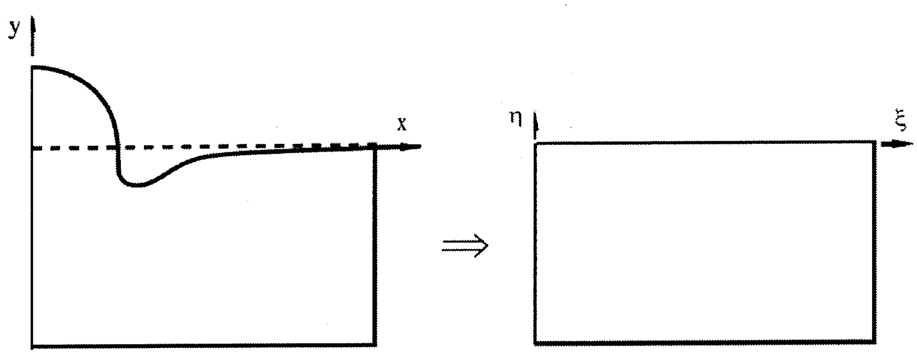

Figure 2. Mapping of the physical plane (x, y) onto the computational plane (ξ,η).

As the flow field evolves in time, the grid in physical space will move, with its lines being attracted to regions of high flow gradients through the use of an adaptive-grid technique. However, the Cartesian grid in computational space always remains fixed and uniform.

In curvilinear coordinates (ξ,η), Equations (2.4) and (2.5) become

$$u_t - x_t(y_\eta u_\xi - y_\xi u_\eta)/J - y_t(x_\xi u_\eta - x_\eta u_\xi)/J$$

$$+[y_\eta(u^2)_\xi - y_\xi(u^2)_\eta]/J + [x_\xi(uv)_\eta - x_\eta(uv)_\xi]/J + (y_\eta p_\xi - y_\xi p_\eta)/J$$

$$= (\alpha u_{\xi\xi} - 2\beta u_{\xi\eta} + \gamma u_{\eta\eta} + \sigma^* u_\eta + \tau^* u_\xi)/\mathrm{Re}J^2 \tag{2.6}$$

$$v_t - x_t(y_\eta v_\xi - y_\xi v_\eta)/J - y_t(x_\xi v_\eta - x_\eta v_\xi)/J$$

$$+[y_\eta(uv)_\xi - y_\xi(uv)_\eta]/J + [x_\xi(v^2)_\eta - x_\eta(v^2)_\xi]/J + (x_\xi p_\eta - x_\eta p_\xi)/J$$

$$= (\alpha v_{\xi\xi} - 2\beta v_{\xi\eta} + \gamma v_{\eta\eta} + \sigma^* v_\eta + \tau^* v_\xi) / \mathrm{Re}\, J^2 \tag{2.7}$$

where J is the Jacobian matrix associated with the transformation of coordinates, that is

$$J = \frac{D(x,y)}{D(\xi,\eta)} = \begin{vmatrix} x_\xi & x_\eta \\ y_\xi & y_\eta \end{vmatrix}.$$

The quantities α, β, γ, σ^* and τ^* are defined as follows

$$\left.\begin{aligned} \alpha &= x_\eta^2 + y_\eta^2 \\ \beta &= x_\xi x_\eta + y_\xi y_\eta \\ \gamma &= x_\xi^2 + y_\xi^2 \end{aligned}\right\} \tag{2.8}$$

$$\left.\begin{aligned} \sigma^* &= \gamma Q^*(\xi,\eta) \\ \tau^* &= \alpha P^*(\xi,\eta) \end{aligned}\right\} \tag{2.9}$$

where $P^*(\xi,\eta)$ and $Q^*(\xi,\eta)$ denote the control functions for the system of coordinates. Their specific form will be given below.

The details of the derivation of Equations (2.6) and (2.7) are given in Appendix A.

2.2 The Boundary Conditions

We have four boundary conditions which can be expressed as follows.

2.2.1 First Boundary Condition

The free-surface, described by $y = Y(x,t)$, is a part of the solution. Neglecting surface tension, the boundary conditions at $y = Y(x,t)$ are

$$\frac{\partial Y}{\partial t} = v - u\frac{\partial Y}{\partial x}, \tag{2.10}$$

$$(p-\frac{Y}{Fr^2}-\frac{2}{Re}\frac{\partial u}{\partial x})\frac{\partial Y}{\partial x}+\frac{1}{Re}(\frac{\partial u}{\partial y}+\frac{\partial v}{\partial x})=0 \tag{2.11}$$

$$(p-\frac{Y}{Fr^2}-\frac{2}{Re}\frac{\partial v}{\partial y})+\frac{1}{Re}(\frac{\partial u}{\partial y}+\frac{\partial v}{\partial x})\frac{\partial Y}{\partial x}=0\,. \tag{2.12}$$

where surface tension has been neglected.

In the computational space (ξ,η), the kinematic boundary condition (2.10), expressing the fact that the free surface moves as a material surface, becomes:

$$\text{at } y=Y,\quad (\frac{\partial Y}{\partial t})_x = v-u\frac{Y_\xi}{x_\xi} \tag{2.13a}$$

or,

$$\text{at } y=Y,\qquad \frac{\partial y}{\partial t}=v\;,\qquad \frac{\partial x}{\partial t}=u\,. \tag{2.13b}$$

Here, the subscript x refers to the grid points in physical space that are located at the free-surface; these points are not allowed to move in the x-direction. Equations (2.13a) and (2.13b) are used to calculate the free-surface elevation at every longitudinal location x, and at every time step.

The free-surface in physical space (x,y) maps onto a constant $\eta-line$ in the computational domain (ξ,η). For the constant $\eta-line$, the needed conditions for the velocity components, u and v, in the computational domain can be obtained from Equations (2.11) and (2.12), i.e.

at $y=Y$,

$$u_\eta=\frac{1}{\gamma}[\beta u_\xi - Jv_\xi - ReJy_\xi(p-\frac{Y}{Fr^2})]\,, \tag{2.14}$$

and

$$v_\eta = \frac{1}{\gamma}[Ju_\xi + \beta v_\xi + ReJx_\xi(p - \frac{Y}{Fr^2})] \tag{2.15}$$

The conditions for the pressure p at the free-surface $y = Y$ in the computational space (ξ, η) can be obtained from Equations (2.14) and (2.15) as follows.

at $y = Y$,

$$p = \frac{\mathrm{Y}}{Fr^2} + \frac{1}{ReJ}(x_\xi v_\eta - y_\xi u_\eta) - \frac{1}{\gamma Re}[u_\xi x_\xi + v_\xi y_\xi + \frac{\beta}{J}(v_\xi x_\xi - u_\xi y_\xi)] \tag{2.16}$$

2.2.2 Second Boundary Condition

On the centerline, i.e. at $x = 0$, due to the symmetry, we have

$$\left.\begin{aligned} &u = 0 \\ &\frac{\partial v}{\partial x} = 0 \\ &\frac{\partial p}{\partial x} = 0 \end{aligned}\right\}. \tag{2.17}$$

In the computational space (ξ, η), Equations (2.17) gives at $\xi = 0$

$$u = 0, \tag{2.18}$$

$$\frac{\partial v}{\partial \xi} = 0, \tag{2.19}$$

$$\frac{\partial p}{\partial \xi} = 0. \tag{2.20}$$

2.2.3 Third Boundary Condition

At $x \to \infty$, $-\infty < y \le 0$, we have the boundary conditions

$$u = v = 0\,, \qquad p = 0\,. \tag{2.21}$$

2.2.4 Fourth Boundary Condition

At $y \to -\infty$, we have

$$u = v = 0\,, \qquad p = 0\,. \tag{2.22}$$

In practice, it is not possible to consider an infinite domain. We thus consider a finite region $(0 \le x \le x_a\,,\ \ -y_a \le y \le 0)$, where the third and fourth boundary conditions are replaced by

New Third Boundary Condition

At $x = +x_a$, $-y_a \le y \le 0$, we have $p = 0$, and u and v are obtained by means of a second-order extrapolation along a coordinate line into the interior.

New Fourth Boundary Condition

At $y = -y_a$, we have $p = 0$, and u, v are obtained by means of a second-order extrapolation along a coordinate line into the interior.

2.3 The Initial Condition

The initial condition ($t = t_0$) corresponds to an undisturbed free-surface. At this time, the boundary $y = 0$ is still a plane boundary with zero shear stress boundary condition and zero velocity, i.e. $u = v = 0$. The flow field is irrotational except in the vicinity of the vortex centers.

2.3.1. The Flow in the Vicinity of the Vortex Center

The point vortex (or a line vortex along the z-direction) represents a singularity with infinite vorticity in the flow field. The effect of viscosity is to diffuse vorticity rapidly from the singular point. We now construct a solution describing this process.

For an incompressible fluid flow, the Navier-Stokes equation can be written as

$$\frac{\partial \vec{u}}{\partial t} + \frac{1}{2}\nabla q^2 - \vec{u} \times \vec{\zeta} = -\frac{1}{\rho}\nabla p - \nu \nabla \times \vec{\zeta}. \qquad (2.23)$$

Taking the curl of this equation, i.e. $\nabla \times$ Equation (2.23), and noticing that $\nabla \times (\rho \nabla p) = 0$ for constant density, we can write

$$\frac{\partial \vec{\zeta}}{\partial t} + \frac{1}{2}\nabla \times \nabla q^2 - \nabla \times \vec{u} \times \vec{\zeta} = -\nu \nabla \times \nabla \vec{\zeta}. \qquad (2.24)$$

The following manipulation

$$\nabla \times \vec{u} \times \vec{\zeta} = \varepsilon_{ijk} \frac{\partial}{\partial x_j} \varepsilon_{klm} u_l \zeta_m = (\delta_{il}\delta_{jm} - \delta_{im}\delta_{jl})(u_l \frac{\partial \zeta_m}{\partial x_j} + \zeta_m \frac{\partial u_l}{\partial x_j})$$

$$= u_i \frac{\partial \zeta_j}{\partial x_j} - u_j \frac{\partial \zeta_i}{\partial x_j} + \zeta_j \frac{\partial u_i}{\partial x_j} - \zeta_i \frac{\partial u_j}{\partial x_j}$$

$$= -\vec{u} \cdot \nabla \vec{\zeta} + \vec{\zeta} \cdot \nabla \vec{u},$$

together with,

$$\nabla \times \nabla \times \vec{\zeta} = \varepsilon_{ijk} \frac{\partial}{\partial x_j} \varepsilon_{klm} \frac{\partial \zeta_m}{\partial x_l} = (\delta_{il}\delta_{jm} - \delta_{im}\delta_{jl}) \frac{\partial}{\partial x_j} \frac{\partial \zeta_m}{\partial x_l}$$

$$= \frac{\partial}{\partial x_i}\frac{\partial \zeta_j}{\partial x_j} - \frac{\partial^2 \zeta_i}{\partial x_j \partial x_j}$$

$$= -\nabla^2 \vec{\zeta},$$

and

$$\nabla \times \nabla q^2 = 0,$$

lead to the well-known vorticity equation

$$\frac{\partial \vec{\zeta}}{\partial t} + \vec{u} \cdot \nabla \vec{\zeta} = \vec{\zeta} \cdot \nabla \vec{u} + \nu \nabla^2 \vec{\zeta} \tag{2.25}$$

or, in a more compact, symbolic, form,

$$\frac{D\vec{\zeta}}{Dt} = \vec{\zeta} \cdot \nabla \vec{u} + \nu \nabla^2 \vec{\zeta}. \tag{2.26}$$

This equation expresses that the rate of change of particle vorticity is due to two factors: the rate of deforming vortex lines and the net rate of diffusion of vorticity.

In the 2-D case, we can simplify this expression by writing $\vec{\zeta} = \zeta \vec{k}$, $\vec{u} = u\vec{i} + v\vec{j}$ with

$$\zeta = \frac{\partial v}{\partial x} - \frac{\partial u}{\partial y}.$$

The vortex line turning and stretching term then becomes:

$$\vec{\zeta} \cdot \nabla \vec{u} = \zeta \vec{k} \cdot (\vec{i}\frac{\partial}{\partial x} + \vec{j}\frac{\partial}{\partial y} + \vec{k}\frac{\partial}{\partial z})(u\vec{i} + v\vec{j})$$

$$= \zeta \frac{\partial}{\partial z}(u\vec{i} + v\vec{j})$$

$$= 0.$$

Here, we recover the well-known result that the vortex line turning and stretching is absent in plane flows. Equation (2.25) then reduces to

$$\frac{\partial \vec{\zeta}}{\partial t} + \vec{u} \cdot \nabla \vec{\zeta} = \nu \nabla^2 \vec{\zeta} . \tag{2.27}$$

We now consider the radially-symmetric diffusion of a singer line vortex, whose axis coincides with the z-axis in cylindrical coordinates. Then, the only non-zero velocity component is the z-component, which depends only on r and t. The vorticity diffusion equation becomes

$$\frac{\partial \zeta}{\partial t} = \nu \frac{1}{r} \frac{\partial}{\partial r}(r \frac{\partial \zeta}{\partial r}) . \tag{2.28}$$

We now look for a self-similar solution of this problem, in the form

$$\zeta = \Gamma (\nu t)^{-1} \tilde{f}(\tilde{\eta}) \tag{2.29}$$

where $\tilde{\eta}$ is the self-similarity variable $\tilde{\eta} = r(\nu t)^{-1/2}$. Here, Γ denotes the circulation of the line vortex. Substitution of this solution in the diffusion equation leads to

$$\frac{\nu}{r} \frac{\partial}{\partial r}(r \frac{\partial \zeta}{\partial r}) = \Gamma (\nu t^2)^{-1} \frac{(\tilde{\eta} \tilde{f}')'}{\tilde{\eta}}$$

where $\tilde{f}' = \dfrac{\partial \tilde{f}}{\partial \tilde{\eta}}$, etc. The final equation can be written as

$$2(\tilde{\eta} \tilde{f}')' + \tilde{\eta}(2\tilde{f} + \tilde{\eta} \tilde{f}') = 0 \tag{2.30}$$

or, in a more compact form,

$$(2\tilde{\eta} \tilde{f}' + \tilde{\eta}^2 \tilde{f}')' = 0 . \tag{2.31}$$

Integrating once gives

$$2\tilde{\eta}\tilde{f}' + \tilde{\eta}^2\tilde{f} = \tilde{A}$$

where $\tilde{A}$ is a constant. For the present physical problem, $\tilde{f}'(0)$ and $\tilde{f}(0)$ should be finite at all values of $\tilde{\eta}$, and therefore, $\tilde{A} = 0$. This implies

$$\frac{d\tilde{f}}{\tilde{f}} = -\frac{\tilde{\eta}}{2}d\tilde{\eta}. \tag{2.32}$$

A straightforward integration leads to the solution of the form

$$\tilde{f}(\tilde{\eta}) = B\exp(-\frac{\tilde{\eta}^2}{4})$$

where B is determined by the expression the vorticity

$$\Gamma = \int_0^\infty \zeta 2\pi r dr,$$

that is

$$\Gamma = \int_0^\infty \zeta 2\pi r dr = 2\pi\int_0^\infty B\exp(-\frac{r^2}{4\nu t})rdr = 4\pi\nu t \cdot B\,(t).$$

This immediately gives the expression of B(t)

$$B(t) = \frac{\Gamma}{4\pi\nu t},$$

which, in turn, leads to the expression of the vorticity

$$\zeta(r,t) = \frac{\Gamma}{4\pi\nu t}\exp(-\frac{r^2}{4\nu t}). \tag{2.33}$$

The corresponding distribution for $q(r,t) = \sqrt{u^2 + v^2}$ is obtained by means of the following integration

$$\int_0^{2\pi} q(r,t)\cdot r d\theta = \int_0^{\infty} \zeta \cdot 2\pi r dr = \int_0^{\infty} \frac{\Gamma}{4\pi \nu t} \exp(-\frac{r^2}{4\nu t})\cdot 2\pi r dr .$$

This results in the expression of $q(r,t)$ as follows.

$$q(r,t) = \frac{\Gamma}{2\pi r}\left[1 - \exp\left(-\frac{r^2}{4\nu t}\right)\right] \tag{2.34}$$

Since the strength of the point vortex is $\kappa = \Gamma/2\pi$, $q(r,t)$ can be expressed in terms of κ:

$$q(r,t) = \frac{\kappa}{r}\left[1 - \exp\left(-\frac{r^2}{4\nu t}\right)\right] \tag{2.35}$$

whose dimensionless form is

$$q(r,t) = \frac{1}{r}\left[1 - \exp\left(-\frac{r^2 Re}{4t}\right)\right]. \tag{2.36}$$

It can be seen that as time t increases from 0 to ∞, $q(r,t)$ decreases from $\Gamma/2\pi r$ to 0. The vorticity, on the other hand, increases (for $r > 0$) from zero to a maximal value before decreasing asymptotically to zero.

We now seek for an expression of the velocity in the vicinity of the vortex core. For this, we introduce the radius r_s from the vortex core, such that

$$q(r,t_s) = \frac{1}{r}\left[1 - \exp\left(-\frac{r^2 Re}{4t_s}\right)\right], \qquad (r \le r_s) \tag{2.37}$$

where t_s is the time duration over which Equation (2.36) is applied. The velocity components can then be obtained as

$$u(r,\varphi,t) = q(r,t)\sin\varphi, \qquad v(r,\varphi,t) = -q(r,t)\cos\varphi \tag{2.38}$$

where φ is the angle defining the point considered. An acceptable error, which is defined by the ratio between the vorticity at $r = r_s$ and the maximal core vorticity at $r = 0$, at $t = t_s$, needs to be considered when using Equation (2.37). It is advantageous, but not necessary in the present code, to take a non-zero error for increasing numerical stability. It should be chosen as a suitable small positive constant. In the present work, the numerical integration of the Navier-Stokes Equation starts at $t = 0$, using the solution (2.37) around the vortex core as the initial conditions.

2.3.2. The Potential Flow Away from the Vortex Centers

The initial condition away from the vortex core, that is $r > r_s$, is considered to be the potential flow which we now calculate.

Since we have assumed that the free-surface is initially undisturbed, the free-surface vorticity is zero. This implies that, apart from a small neighborhood around the vortices, the flow is irrotational everywhere. For this reason, we can use the image method for the boundary condition. Consequently we can write the complex potential as follows (see sketch below)

$$w = \phi + i\psi = -i\frac{\Gamma}{2\pi}\ln\frac{(z - z_v)(z + z_v)}{(z - \bar{z}_v)(z + \bar{z}_v)},$$

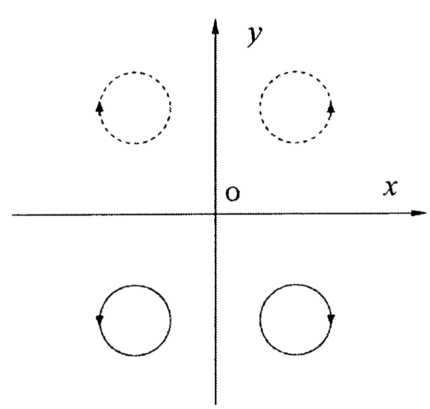

or

$$w = -i\frac{\Gamma}{2\pi}[\ln(z - z_v) + \ln(z + z_v)$$

$$- \ln(z - \bar{z}_v) - \ln(z + \bar{z}_v)],$$

(2.39)

where z refers to the location of the point considered in the complex plane, $z = x + iy$, and ϕ and ψ are the potential and stream functions, respectively. The position of one of the vortices is represented by z_v, while the bar denotes the complex conjugate.

We can then write

$$\frac{dw}{dz} = u - iv$$

$$= -i\frac{\Gamma}{2\pi}\left[\frac{1}{z - z_v} + \frac{1}{z + z_v} - \frac{1}{z - \bar{z}_v} - \frac{1}{z + \bar{z}_v}\right]$$

$$= -i\frac{\Gamma}{2\pi}\left[\frac{1}{(x+iy)-(x_1+iy)} + \frac{1}{(x+iy)-(x_3+iy_3)}\right.$$

$$\left. - \frac{1}{(x+iy)-(x_2+iy_2)} - \frac{1}{(x+iy)-(x_4+iy_4)}\right]$$

$$= -i\frac{\Gamma}{2\pi}\left[\frac{(x-x_1)-i(y-y_1)}{r_1^2} + \frac{(x-x_3)-i(y-y_3)}{r_3^2}\right.$$

$$\left. - \frac{(x-x_2)-i(y-y_2)}{r_2^2} - \frac{(x-x_4)-i(y-y_4)}{r_4^2}\right],$$

which gives us the velocity components

$$u = \frac{\Gamma}{2\pi}\left[-\frac{y-y_1}{r_1^2} + \frac{y-y_2}{r_2^2} - \frac{y-y_3}{r_3^2} + \frac{y-y_4}{r_4^2}\right] \tag{2.40}$$

and

$$v = \frac{\Gamma}{2\pi}\left[\frac{x-x_1}{r_1^2} - \frac{x-x_2}{r_2^2} + \frac{x-x_3}{r_3^2} - \frac{x-x_4}{r_4^2}\right]. \tag{2.41}$$

Taking into account the fact that $\kappa = \Gamma/2\pi$, we can rewrite Equations (2.40) and (2.41) as

$$u = \kappa\left[-\frac{y-y_1}{r_1^2}+\frac{y-y_2}{r_2^2}-\frac{y-y_3}{r_3^2}+\frac{y-y_4}{r_4^2}\right]$$

and

$$v = \kappa\left[\frac{x-x_1}{r_1^2}-\frac{x-x_2}{r_2^2}+\frac{x-x_3}{r_3^2}-\frac{x-x_4}{r_4^2}\right],$$

or, in dimensionless form,

$$u = \left[-\frac{y-y_1}{r_1^2}+\frac{y-y_2}{r_2^2}-\frac{y-y_3}{r_3^2}+\frac{y-y_4}{r_4^2}\right] \tag{2.42}$$

and

$$v = \left[\frac{x-x_1}{r_1^2}-\frac{x-x_2}{r_2^2}+\frac{x-x_3}{r_3^2}-\frac{x-x_4}{r_4^2}\right] \tag{2.43}$$

In Equations (2.42) and (2.43), all variables are non-dimensional. For convenience, we have kept the same symbols for dimensional and non-dimensional variables. Equations (2.42) and (2.43) are used together with Equation (2.37) to calculate the initial conditions.

CHAPTER 3

NUMERICAL SCHEME

In order to solve the previous Navier-Stokes equations subjected to highly nonlinear, moving boundary conditions, we use a fully implicit numerical finite difference scheme. The method used is a backward time, second-order central space formulation, coupled with a numerical generation of adaptive curvilinear, boundary-fitted, coordinates for which one coordinate line coincides with the free-surface. We have used the velocity-pressure (primitive variables) formulation. The solution of the field variables (velocity-pressure) and that of the physical space are obtained simultaneously, and particular attention was paid to their convergence.

More details will be given below.

3.1 Equations

Here, the goal is to obtain p, u, v, x, y by solving a set of equations simultaneously.

In non-conservative form, the two-dimensional Navier-Stokes equations can be written as

$$u_t + uu_x + vu_y = -p_x + (u_{xx} + u_{yy}) / Re \qquad (2.1)$$

$$v_t + uv_x + vv_y = -p_y + (v_{xx} + v_{yy}) / Re \qquad (2.2)$$

with the continuity equation being

$$u_x + v_y = 0 \qquad (2.3)$$

A Poisson equation for pressure can be obtained by taking the divergence of Equations (2.1) and (2.2), that is

$$p_{xx} + p_{yy} = -[(u_x)^2 + 2u_y v_x + (v_y)^2]. \tag{3.1}$$

While for physical space coordinates we have

$$\alpha x_{\xi\xi} - 2\beta x_{\xi\eta} + \gamma x_{\eta\eta} + \alpha \ \ P^* x_\xi + \gamma Q^* x_\eta = 0 \tag{3.2}$$

$$\alpha y_{\xi\xi} - 2\beta y_{\xi\eta} + \gamma y_{\eta\eta} + \alpha \ \ P^* y_\xi + \gamma Q^* y_\eta = 0 \tag{3.3}$$

Considering that the physical space coordinate system moves with time as the free-surface deforms, the equations for physical-space coordinates, velocity components and pressure need to be solved simultaneously at each time step. For this purpose, we use the Successive Over-Relaxation, SOR, iterative technique. In order to obtain the pressure within the domain at any non-zero time, we use an iteration method similar to Chorin's (1967) iteration technique. Equation (3.1) is used to obtain the initial pressure in a manner similar to that used by Ohring and Lugt.

In finite difference form, the previous five equations give

$$u_{i,j}^{n+1} = \lambda_1 \{u_{i,j}^n + \Delta t[(x_t^{'})_{i,j}((y_\eta^{'})_{i,j}^{n+1}(u_\xi^{'})_{i,j}^{n+1} - (y_\xi^{'})_{i,j}^{n+1}(u_\eta^{'})_{i,j}^{n+1})/J^{'}$$

$$+ (y_t^{'})_{i,j}((x_\xi^{'})_{i,j}^{n+1}(u_\eta^{'})_{i,j}^{n+1} - (x_\eta^{'})_{i,j}^{n+1}(u_\xi^{'})_{i,j}^{n+1})/J^{'}$$

$$- ((y_\eta^{'})_{i,j}^{n+1} u_{i,j}^{n+1}(u_\xi^{'})_{i,j}^{n+1} - (y_\xi^{'})_{i,j}^{n+1} u_{i,j}^{n+1}(u_\eta^{'})_{i,j}^{n+1})/J^{'}$$

$$- ((x_\xi^{'})_{i,j}^{n+1} u_{i,j}^{n+1}(v_\eta^{'})_{i,j}^{n+1} - (x_\eta^{'})_{i,j}^{n+1} u_{i,j}^{n+1}(v_\xi^{'})_{i,j}^{n+1})/J^{'}$$

$$+ (\alpha_{i,j}^{'}(u_{i-1,j}^{n+1} + u_{i+1,j}^{n+1}) - \beta_{i,j}^{'}(u_{\xi\eta}^{'})_{i,j}^{n+1}/2 + \gamma_{i,j}^{'}(u_{i,j-1}^{n+1} + u_{i,j+1}^{n+1})$$

$$+ \sigma_{i,j}^{**}(u_\eta^{'})_{i,j}^{n+1} + \tau_{i,j}^{**}(u_\xi^{'})_{i,j}^{n+1})/ReJ^{'2}]\}/DMU$$

$$+(1-\lambda_1)u^n_{i,j} \tag{3.4}$$

and

$$v^{n+1}_{i,j} = \lambda_1\{v^n_{i,j} + \Delta t[(x'_t)_{i,j}((y'_\eta)^{n+1}_{i,j}(v'_\xi)^{n+1}_{i,j} - (y'_\xi)^{n+1}_{i,j}(v'_\eta)^{n+1}_{i,j})/J'$$

$$+(y'_t)_{i,j}((x'_\xi)^{n+1}_{i,j}(v'_\eta)^{n+1}_{i,j} - (x'_\eta)^{n+1}_{i,j}(v'_\xi)^{n+1}_{i,j})/J'$$

$$-((y'_\eta)^{n+1}_{i,j}u^{n+1}_{i,j}(v'_\xi)^{n+1}_{i,j} - (y'_\xi)^{n+1}_{i,j}u^{n+1}_{i,j}(v'_\eta)^{n+1}_{i,j})/J'$$

$$-((x'_\xi)^{n+1}_{i,j}v^{n+1}_{i,j}(v'_\eta)^{n+1}_{i,j} - (x'_\eta)^{n+1}_{i,j}v^{n+1}_{i,j}(v'_\xi)^{n+1}_{i,j})/J'$$

$$+(\alpha'_{i,j}(v^{n+1}_{i-1,j} + v^{n+1}_{i+1,j}) - \beta'_{i,j}(v'_{\xi\eta})^{n+1}_{i,j}/2 + \gamma'_{i,j}(v^{n+1}_{i,j-1} + v^{n+1}_{i,j+1})$$

$$+\sigma^{*'}_{i,j}(v'_\eta)^{n+1}_{i,j} + \tau^{*'}_{i,j}(v'_\xi)^{n+1}_{i,j})/ReJ'^2]\}/DMV$$

$$+(1-\lambda_1)v^n_{i,j} \tag{3.5}$$

where n refers to the time level n, the corresponding time being t^n. .

Similarly, we can write the discretization form of the equations for the pressure p, the physical space coordinates x, y and the position of the free-surface.

3.2 Implicit Time Differencing and Pseudo-Compressibility

The following equations represent the implicit time differencing procedure for advancing the flow solution (p,u,v,x,y) in the interior of the domain over the time step $\Delta t = t^{n+1} - t^n$, that is, from the time level n to the time level $n+1$, by using the pseudo-time step $\Delta\tau = \tau^{n+1} - \tau^n$:

$$x^{n+1,m+1} = \tilde{g}_1(x^{n+1,m+1}, y^{n+1,m+1}, P^{*n}, Q^{*n}), \tag{3.6}$$

$$y^{n+1,m+1} = \tilde{g}_2(x^{n+1,m+1}, y^{n+1,m+1}, P^{*n}, Q^{*n}), \tag{3.7}$$

$$\frac{p^{n+1,m+1} - p^{n+1,m}}{\Delta\tau} = -(\nabla \cdot \vec{u})^{n+1,m+1}, \tag{3.8}$$

$$\frac{u^{n+1,m+1} - u^{n}}{\Delta t} = \tilde{g}_3^{n+1,m+1}, \tag{3.9}$$

$$\frac{v^{n+1,m+1} - v^{n}}{\Delta t} = \tilde{g}_4^{n+1,m+1}. \tag{3.10}$$

Equations (3.6) and (3.7) are derived from Equations (3.2) and (3.3), respectively. Similarly, Equations (3.9), (3.10) are obtained from Equations (2.6) and (2.7).

The continuity Equation (2.3) is replaced by an equation with pseudo-compressibility in order to numerically conserve mass at each time step:

$$\frac{\partial p}{\partial \tau} + \beta^*\left(\frac{\partial u}{\partial x} + \frac{\partial v}{\partial y}\right) = 0. \tag{3.11}$$

Equation (3.8) is obtained from Equation (3.11) and is used to obtain the pressure p by means of an iteration method.

3.3 Boundary-fitted Coordinates

The physical space (x, y) is mapped onto the computational domain (ξ, η). The coordinate lines in physical space are mapped onto a uniformly spaced Cartesian mesh with a unit mesh spacing in each coordinate direction, as shown in Figure 2. As the flow field evolves in time, the mesh in physical space will move and its coordinate lines will be attracted to regions of high flow gradients through the use of an adaptive-grid technique, while the Cartesian grid in the computational domain always remains fixed and uniform.

The relation between curvilinear coordinates (ξ, η) and the physical space coordinates (x, y) is defined by the two following elliptic partial differential equations in which the coordinates (x, y) play the role of independent variables

$$\xi_{xx} + \xi_{yy} = (\xi_x^2 + \xi_y^2) P^*(\xi, \eta), \tag{3.12}$$

$$\eta_{xx} + \eta_{yy} = (\eta_x^2 + \eta_y^2) Q^*(\xi, \eta). \tag{3.13}$$

However, since all calculations are to be performed in the rectangular computational domain, these two elliptic partial differential equations are transformed by interchanging the dependent and independent variables. The transformation yields

$$\alpha x_{\xi\xi} - 2\beta x_{\xi\eta} + \gamma x_{\eta\eta} + \alpha P^* x_\xi + \gamma Q^* x_\eta = 0 \tag{3.2}$$

$$\alpha y_{\xi\xi} - 2\beta y_{\xi\eta} + \gamma y_{\eta\eta} + \alpha P^* y_\xi + \gamma Q^* y_\eta = 0 \tag{3.3}$$

with α, β, γ given by the following equation.

$$\left.\begin{aligned} \alpha &= x_\eta^2 + y_\eta^2 \\ \beta &= x_\xi x_\eta + y_\xi y_\eta \\ \gamma &= x_\xi^2 + y_\xi^2 \end{aligned}\right\} \tag{2.8}$$

In our numerical algorithm, the physical space coordinates (x, y) are determined in terms of the computational space coordinates (ξ, η) at each time step through Equations (3.2) and (3.3).

The finite difference discretization of Equations (3.2) and (3.3) gives the two following equations.

$$\alpha' \frac{x_{i+1,j} - 2x_{i,j} + x_{i-1,j}}{\Delta\xi^2} - 2\beta' \frac{x_{i+1,j+1} - x_{i+1,j-1} - x_{i-1,j+1} + x_{i-1,j-1}}{4\Delta\xi\Delta\eta}$$

$$\gamma' \frac{x_{i,j+1} - 2x_{i,j} + x_{i,j-1}}{\Delta\eta^2} + \alpha' P^* \frac{x_{i+1,j} - x_{i-1,j}}{2\Delta\xi} + \gamma' Q^* \frac{x_{i,j+1} - x_{i,j-1}}{2\Delta\eta} = 0\,, \tag{3.14}$$

$$\alpha' \frac{y_{i+1,j} - 2y_{i,j} + y_{i-1,j}}{\Delta\xi^2} - 2\beta' \frac{y_{i+1,j+1} - y_{i+1,j-1} - y_{i-1,j+1} + y_{i-1,j-1}}{4\Delta\xi\Delta\eta}$$

$$\gamma' \frac{y_{i,j+1} - 2y_{i,j} + y_{i,j-1}}{\Delta\eta^2} + \alpha' P^* \frac{y_{i+1,j} - y_{i-1,j}}{2\Delta\xi} + \gamma' Q^* \frac{y_{i,j+1} - y_{i,j-1}}{2\Delta\eta} = 0\,. \tag{3.15}$$

where

$$\alpha' = \left(\frac{x_{i,j+1} - x_{i,j-1}}{2\Delta\eta}\right)^2 + \left(\frac{y_{i,j+1} - y_{i,j-1}}{2\Delta\eta}\right)^2 , \tag{3.16}$$

$$\beta' = \frac{(x_{i+1,j} - x_{i-1,j})(x_{i,j+1} - x_{i,j-1})}{4\Delta\xi\Delta\eta} + \frac{(x_{i+1,j} - x_{i-1,j})(x_{i,j+1} - x_{i,j-1})}{4\Delta\xi\Delta\eta}, \tag{3.17}$$

$$\gamma' = \left(\frac{x_{i+1,j} - x_{i-1,j}}{2\Delta\xi}\right)^2 + \left(\frac{y_{i+1,j} - y_{i-1,j}}{2\Delta\xi}\right)^2 . \tag{3.18}$$

Equations (3.8) and (3.9) are nonlinear simultaneous algebraic equations that can be solved by means of iteration methods. Here, we use the Successive Over-Relaxation (SOR) technique to achieve this goal. The SOR technique can be described (Fletcher 1991) as

$$v_i^{(n+1)} = \lambda[(B_i - \sum_{j=1}^{i-1} A_{ij} v_j^{(n+1)} - \sum A_{ij} v_j^{(n)}) / A_{ii}] + (1-\lambda) v_i^n\,. \tag{3.19}$$

3.4 Adaptive Gridding

Adaptive gridding can be realized by giving a special form to the control functions P^*, Q^* of the coordinate system. The basic idea is to use the equi-distribution of a weight function along the arc-length elements in the physical-space grid. These equi-distribution laws for weight functions w_1 and w_2 along arc-length elements on constant $\eta-$ and $\xi-$ lines, respectively, are

$$(x_\xi^2 + y_\xi^2)^{\frac{1}{2}} w_1 = const. \tag{3.20}$$

$$(x_\eta^2 + y_\eta^2)^{\frac{1}{2}} w_2 = const. \tag{3.21}$$

It has been shown that if P^* and Q^* have the form

$$P^* = \frac{(w_1)_\xi}{w_1},, \qquad Q^* = \frac{(w_2)_\eta}{w_2},, \tag{3.22}$$

then the mesh-generating equations (3.2) and (3.3) approximate the equi-distribution laws (3.20) and (3.21), respectively. Weight functions are usually taken to be functions of the flow gradient. They can be chosen as

$$w_1 = [1 + B^2 \,|\frac{q_{\xi\xi}}{(1+q_\xi^2)^{3/2}}|]\sqrt{1 + A^2 q_\xi^2}\,, \tag{3.23}$$

$$w_2 = [1 + B^2 \,|\frac{q_{\eta\eta}}{(1+q_\eta^2)^{3/2}}|]\sqrt{1 + A^2 q_\eta^2} \tag{3.24}$$

where $q = \sqrt{u^2 + v^2}$.

On the symmetry line $x = 0$, the weight function w_2 is given by

$$w_2 = 1 + Av_\eta^2 \ . \tag{3.25}$$

Notice that the computation of y and v on the line $x = 0$ requires only the control function Q^* in Equations (3.22), together with Equations (3.3) and (2.7).

Figure 3a shows the adaptive grid in our numerical simulation of the flow at $Re = 100$, $Fr = 0.8$. One can see the automatic generation of a dense mesh in the area of high free-surface curvature where flow gradients are also the highest. This can be compared with the grid used by Ohring and Lugt (1991) displayed in Figure 3b.

3.5 Highly Implicit Numerical Scheme

The SOR iterative technique is utilized to solve the set of discretized equations. Two underrelaxed (i.e. smaller than one) acceleration parameters (weights) are used, one for the field variables, and another one for the physical coordinates. In both cases, a highly implicit scheme is used, with underrelaxed acceleration parameters. This was found important, *especially for the numerical simulation of high Reynolds number free-surface flows*, in order to obtain numerical stability. However, each set of Reynolds and Froude numbers requires suitable acceleration parameters. For instance, our acceleration parameters are smaller than 0.2 for the case of Reynolds number $Re = 1000$, Froude number $Fr = 1.125$.

In this research, the time step is usually chosen to be $\Delta t = 0.001$ and maintained constant during each run. Our numerical scheme was found to be numerically stable, even at very high Reynolds numbers. In addition to the results presented in this thesis, we have performed preliminary runs for the Reynolds and Froude number values $Re = 4000,\ Fr = 1.125$, for which the solution was found to be numerically stable.

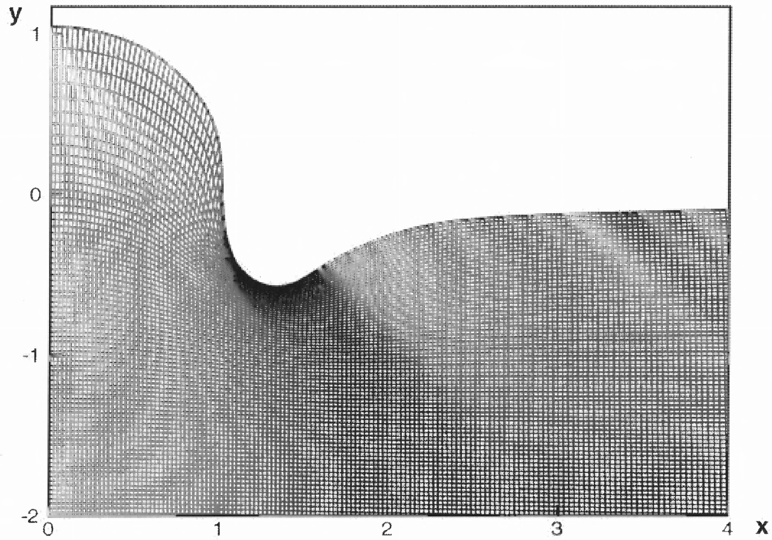

Figure 3a. Section of the computational grid for the Reynolds and the Froude number values Re = 100, Fr = 0.8 at time t = 3.64.

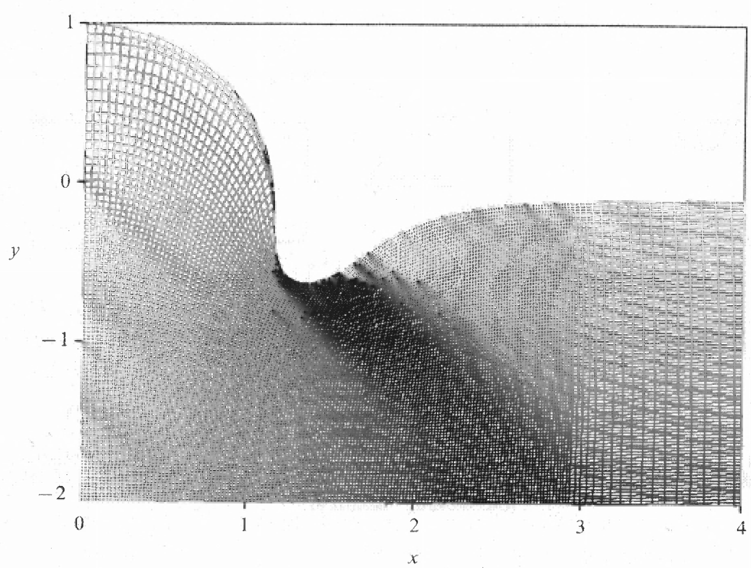

Figure 3b. Section of the grid for the Reynolds and Froude number values Re = 100, Fr = 0.8, at t = 3.475, from Ohring and Lugt's results, 1991.

CHAPTER 4

FLOW SIMULATIONS

Numerical calculations were performed for the following values of Reynolds and Froude numbers:

$Re = 100$, $Fr = 1.125$ and $Fr = 0.8$,

$Re = 500$, $Fr = 1.125$,

$Re = 1000$, $Fr = 1.125$ and $Fr = 2.0$,

$Re = 2000$, $Fr = 1.125$.

In all cases, we neglect surface tension, thus keeping the Weber number zero ($We = 0$). For code validation and comparison with results published in the literature, computations at relatively low values of Reynolds numbers $Re = 10$, $Re = 50$, $Re = 100$ and different Froude number values were performed. In all cases, the initial condition consists of the vortex described in Section 3 surrounded by the potential flow. The initial vortex is shown in Figure 4 for $Re = 100$, $Fr = 0.8$. Before we present our numerical results, it is necessary to define the notion of the center of a vortex, as well as Lamb's potential flow solution for the trajectory of a point vortex in presence of a free-surface.

In an unsteady viscous flow, the center of a vortex can be defined either as the location of local extremal vorticity or as the center of the whirl, that is the center of nested instantaneous streamlines. Whereas the streamlines depend on the particular frame of reference, the vorticity field does not. In all the following figures, the instantaneous streamlines are in a frame of reference fixed with respect to the undisturbed free-surface and the vortex is moving relative to this frame. In general, the center of nested streamlines does not coincide with the location of extremal vorticity. In our study, the

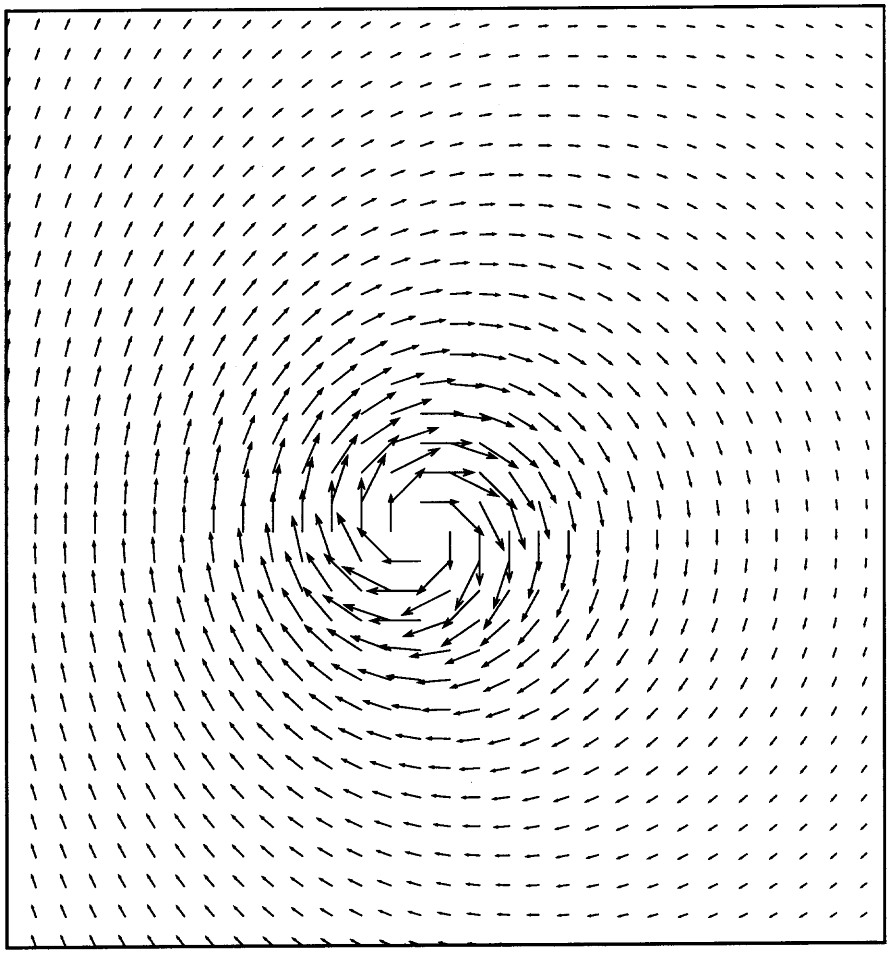

Figure 4. Section of the initial velocity vector field for the Reynolds and Froude number values Re = 100, Fr = 0.8 at time t = 0, The size of the computational grid is 231x191.

"center of the vortex" is defined as the location of the local extremal vorticity. Solid equivorticity lines represent negative values while dashed lines correspond to positive values.

As it is well-known, the classical path of a point vortex with a flat free-surface in a potential flow (Lamb, 1932) is given by

$$x^2 + y^2 = 4x^2y^2, \tag{4.1}$$

with a unit distance between the two vortices located far away from the origin of the system of coordinates. In the findings presented below, we compare the trajectory of the center of the vortex from our computations with the theoretical potential flow result (4.1).

Substituting $\kappa = \Gamma/2\pi$ and $Re = \kappa/\nu$ in Equation (2.33), we can write

$$\zeta(r,t) = \frac{Re}{2t}\exp(-\frac{r^2}{4\nu t}),$$

which gives

$$\zeta(0,t) = \frac{Re}{2t}.$$

This implies that the time decrease of the extremal vorticity $|\zeta_{extremal}|$ at the center of a diffusing point vortex (see Equation (2.33)) follows the equation

$$\frac{|\zeta_{extremal}|}{R_e} = \frac{1}{2t}. \tag{4.2}$$

This result will be compared with the vorticity decay obtained from our numerical simulations.

Convergence of our results with mesh size was investigated at all parameter values presented below. For example, Figure 5 illustrates our study with two different grids, 131x111 points in the left column and 91x91 points in the right column. Here, we report our results for the Reynolds and Froude number values $Re = 100$, $Fr = 0.8$ and at time $t = 3.95$. The first row in Figure 5 shows the two grids, the second row displays both the free-surface elevation and the flow streamlines while the third row exhibits the vorticity contours in both cases.

We now examine the results of our computations in details. In particular, our findings are compared with those of Ohring and Lugt (1991) for Reynolds number values up to $Re = 100$.

4.1 Flow Simulation for $Re = 10,\ Fr = 1.125$

At $Re = 10$, $Fr = 1.125$, the flow is extremely viscous. The time evolution of the vortex path can be observed in Figure 6. It is interesting to notice that the vortex starts its ascension almost vertically, but soon after this, it begins traveling to the right as it raises. The vortex continues its motion, slows down and turns away from the free-surface. This phenomenon was observed experimentally and is referred to in the literature as the "rebounding process". At early times, the vortex path is nearly vertical and is accurately described by Lamb's potential flow solution (Equation 4.1). Soon after this, however, the discrepancy is important, indicating that viscous effects play a major role. The path of the vortex extracted from our computation is compared with Ohring and Lugt's findings. An excellent agreement is found, although our path is slightly smoother than theirs. The free-surface elevation is displayed on a space-time plot in Figure 7. It is interesting to notice that the ascension of the vortex manifests itself as a central standing wave, but that its motion to the right and rebounding correspond to a weak traveling wave on the side of the standing wave. At all times, the free-surface elevation is rather small. The flow was also calculated at $Re = 50$, $Fr = 0.356$. Since good agreement with previous results were observed, details are not reported here.

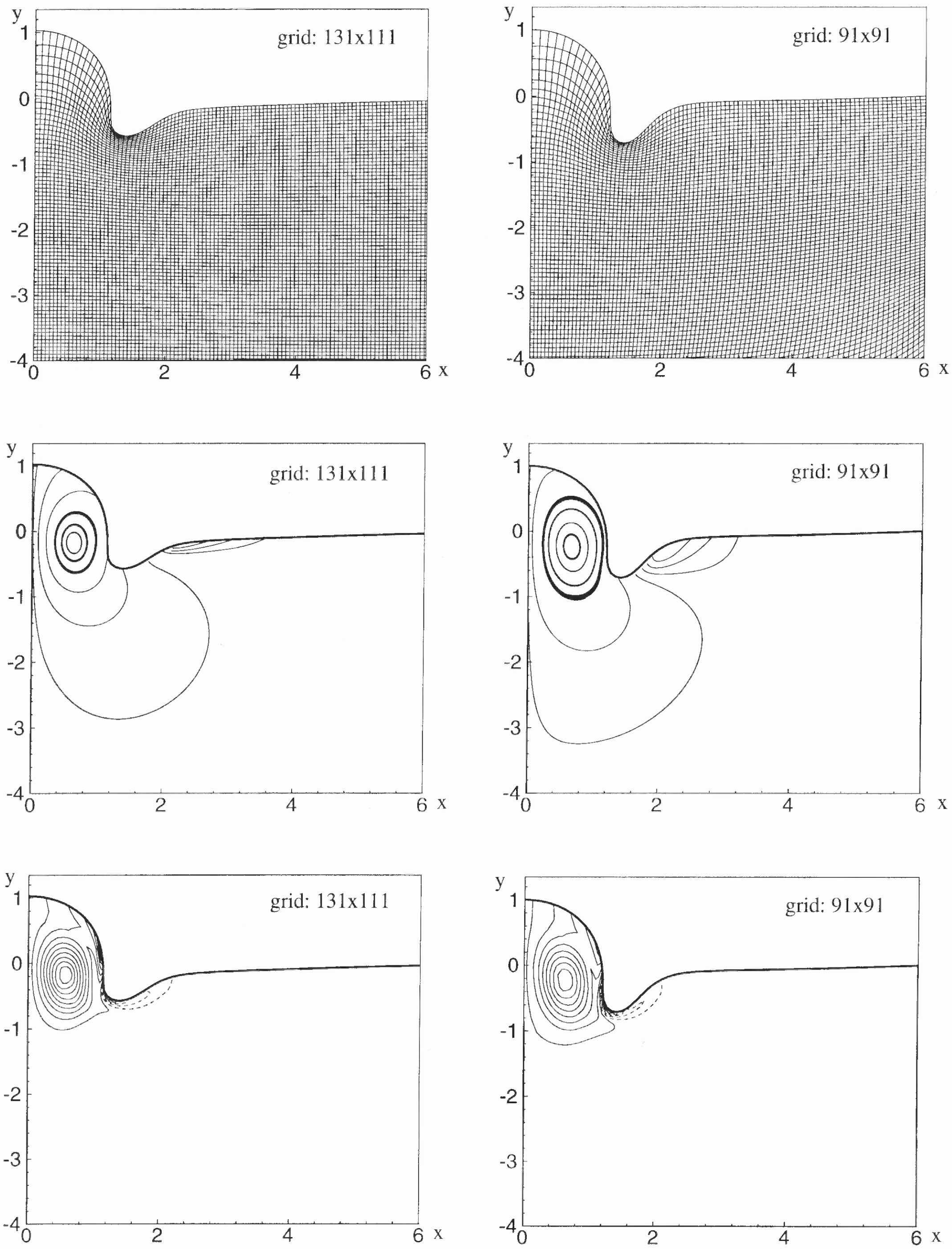

Figure 5. Comparison of the results obtained by using different grids for the Reynolds and Froude values Re = 100, Fr = 0.8, at t = 3.95 (grid 131x111) and t = 4.00 (grid 91x91) respectively. First row: section of the computational mesh; second row: streamlines; third row: vorticity contours (solid lines: negative vorticity, dashed lines: positive vorticity.)

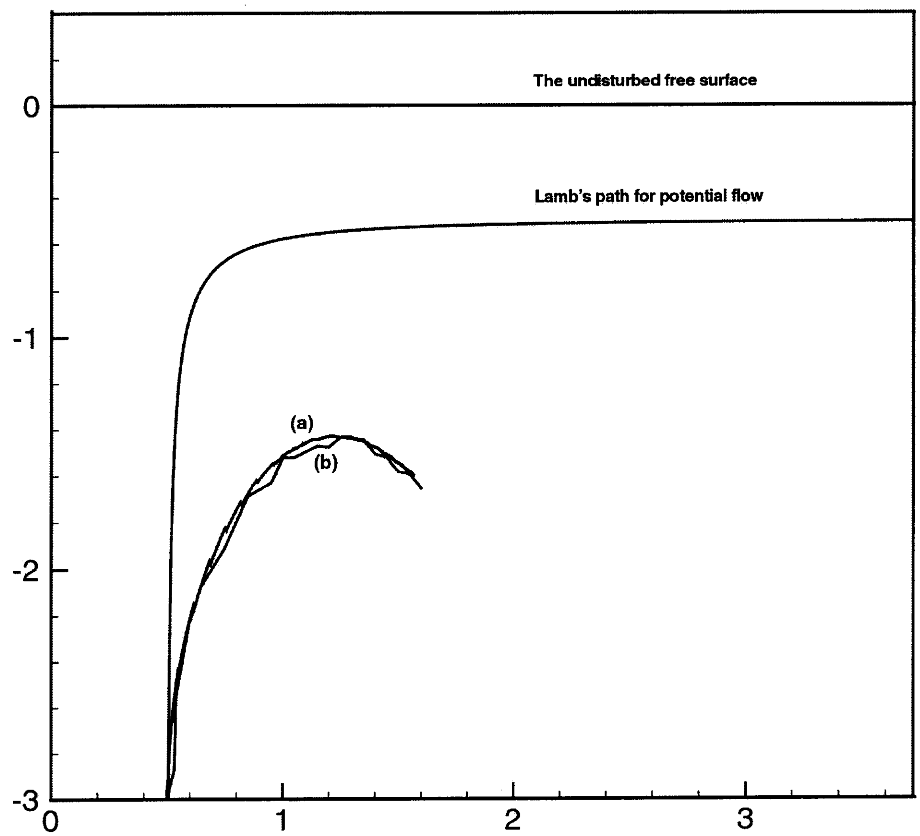

Figure 6. Path of the vortex center for the Reynolds and the Froude number values Re = 10, Fr = 1.125, in the (x, y) plane: (a) our numerical results; (b) Ohring and Lugt's results, 1989.

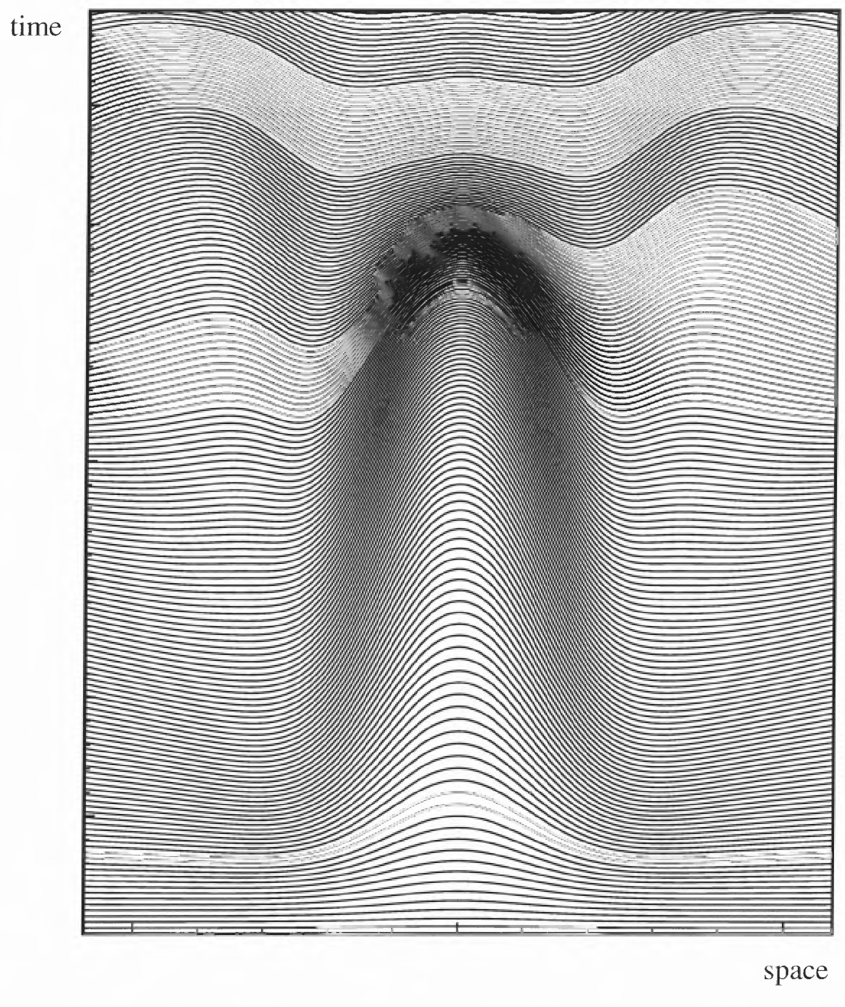

Figure 7. Space -time representation of the free-surface elevation at the Reynolds and Froude number values Re = 10, Fr = 1.125. When the rebounding phenomenon takes place, side traveling waves are produced.

4.2 Flow Simulation for $Re = 100,\ Fr = 0.8$

In this case, a much stronger deformation of the free-surface takes place. Indeed, the vortex pair pushes the free-surface up, creating bumps accompanied by more localized depressions on their sides. These depressions have been observed experimentally by Sarpkaya and Henderson (1984) who named them "scars". Instantaneous streamlines (in a small part of the domain) obtained by our calculations are shown in Figure 8a. For comparison, we have reproduced those reported by Ohring and Lugt (1991) in Figure 8b. The velocity field is shown in Figure 8c. A more global picture of the streamlines and kinetic energy contours is displayed in Figure 9a showing high energy levels in the vicinity of the vortex core, as well as along the scar areas facing the vortex pair. Figure 9b shows the corresponding pressure map, with negative pressure in the vicinity of the vortex core and around the scar. Below and above the vortex, the flow experiences positive pressure whose strength increases just below the free-surface where the elevation of the latter is the highest. The displacement of the vortex core can be followed in Figure 10. The vortex moves straight up, following Lamb's potential flow solution over a much larger distance than at smaller Reynolds numbers. A discrepancy, however, occurs as the vortex approaches the free-surface. While Lamb's solution turns away from the centerline, the viscous vortex continues his quasi-vertical ascension. Figure 10a displays our results while Figure 10b shows Ohring and Lugt's findings (1991). A good agreement is found.

As the free-surface elevation increases, the slope of the resulting wave increases until it reaches such a large amplitude that the computation stops. In nature, the wave will break. Simultaneously, the depression (scar) becomes more and more pronounced. Such a steepening of slopes has a strong effect on the vorticity field, as we now explain. It may be recalled that an approximate formula for the surface vorticity is twice the surface curvature times the tangential surface velocity. This formula implies that an occurrence

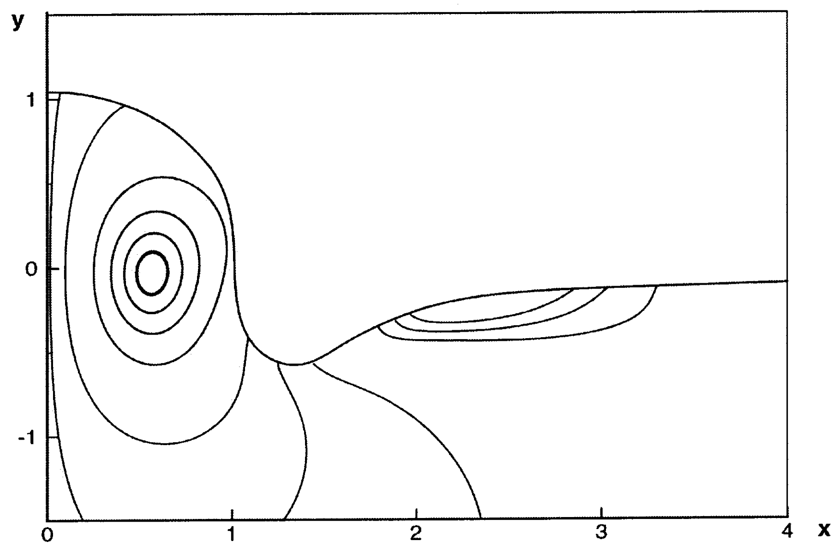

Figure 8a. Streamlines of the flow for the Reynolds and the Froude number values Re = 100, Fr = 0.8 at time t = 3.64

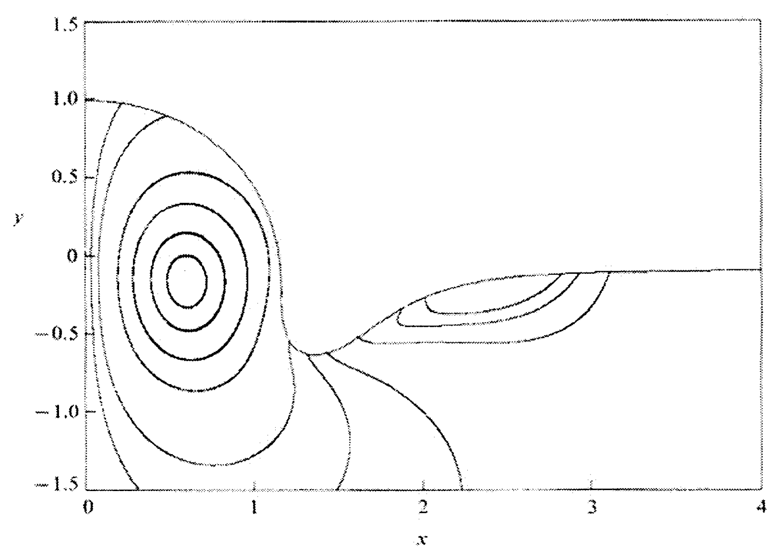

Figure 8b. Streamlines of the flow for the Reynolds and Froude number values Re = 100, Fr = 0.8, at time t = 3.475, from Ohring and Lugt's results, 1991.

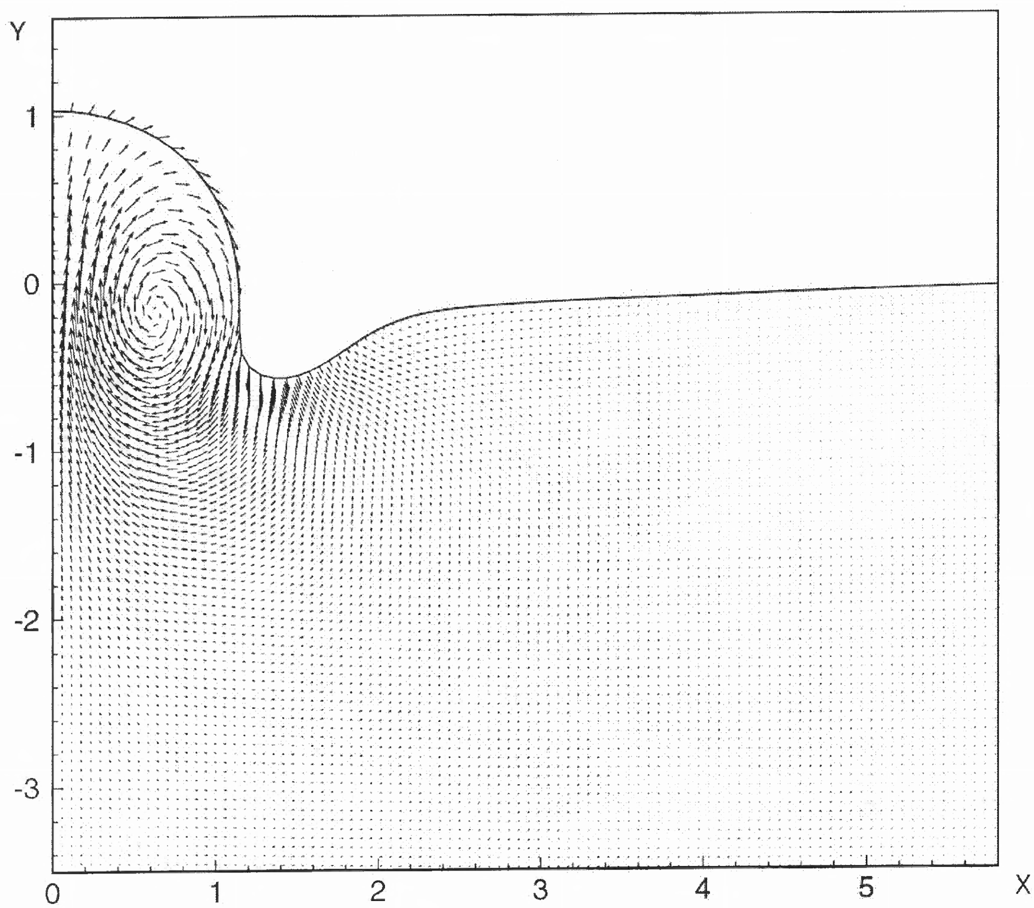

Figure 8c. Vectorial representation of the velocity vector for the Reynolds and Froude number values Re = 100, Fr = 0.8 at t = 4.0. The size of the computational grid is 91x91.

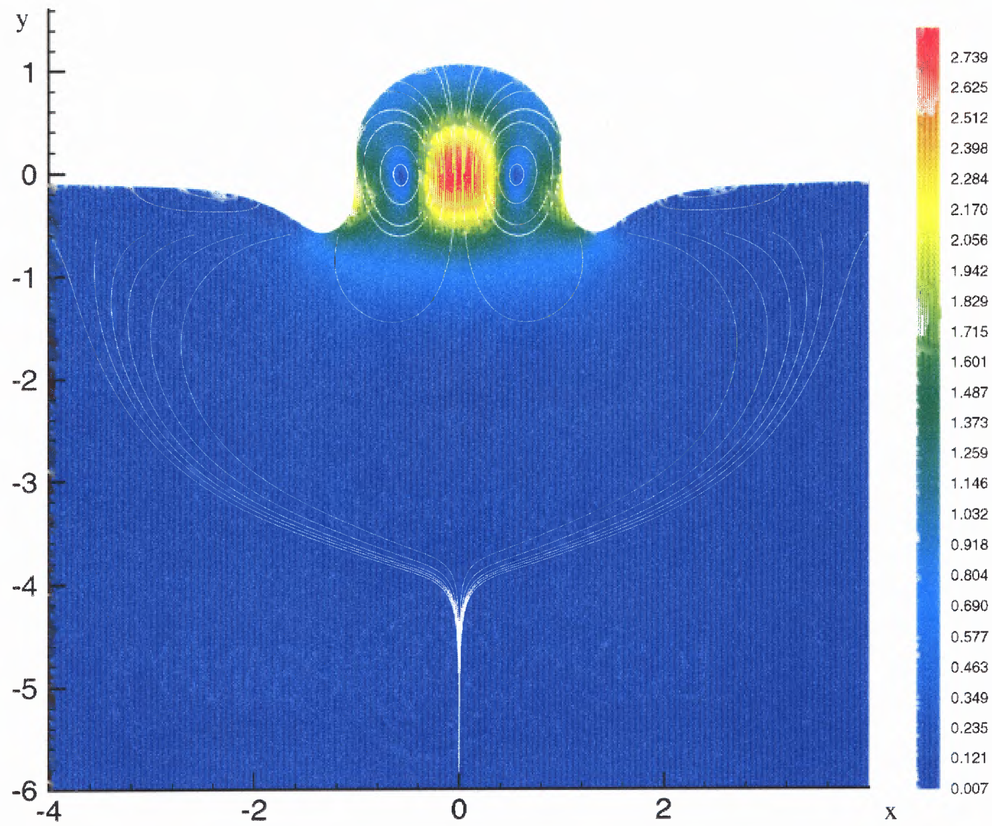

Figure 9a. Streamlines and square root of the kinetic energy distribution for the Reynolds and Froude number values Re = 100, Fr = 0.8, at time t = 3.65.

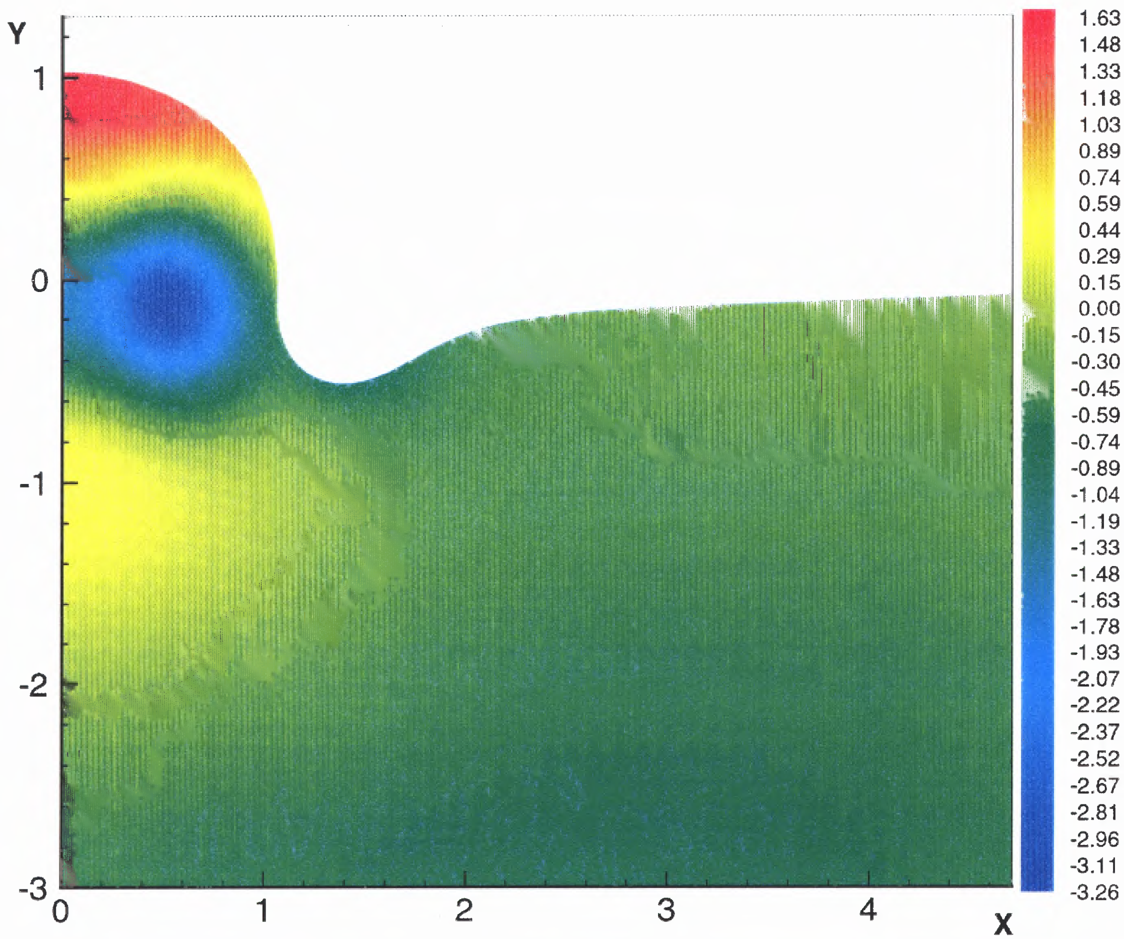

Figure 9b. Pressure distribution for the Reynolds and Froude number values Re = 100, Fr = 0.8, at time t = 3.8. The size of the computational grid is 131x111.

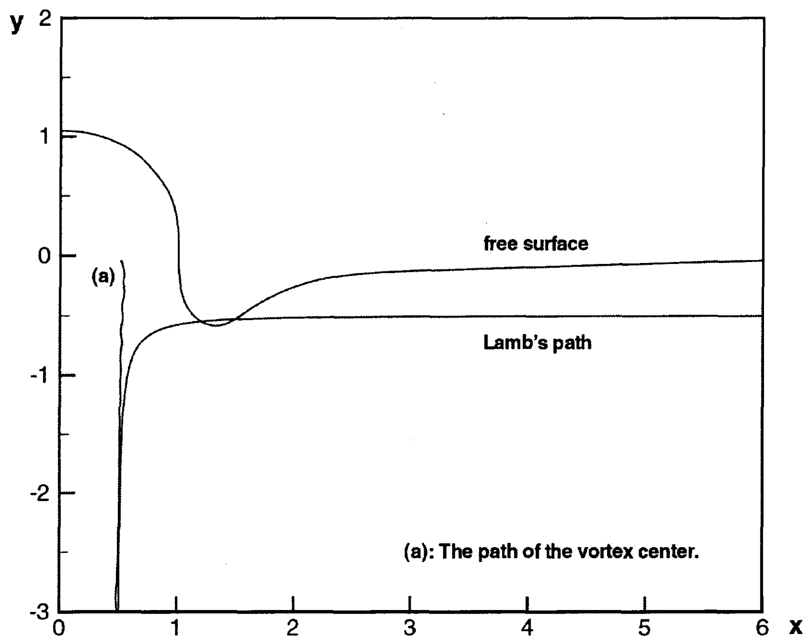

Figure 10a. Path of the vortex center for the Reynolds and the Froude number values Re = 100, Fr = 0.8. For comparison, we have included Lamb's potential flow solution for a flat surface. The free surface is plotted at time t = 3.64.

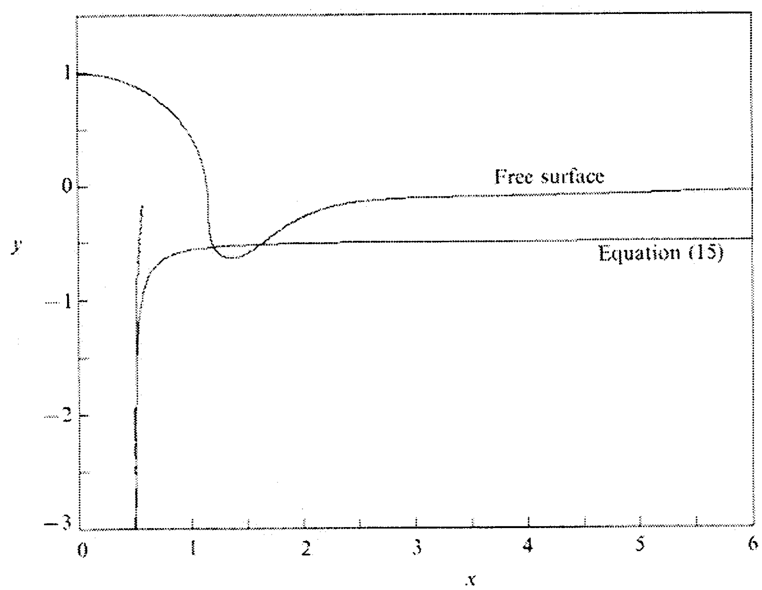

Figure 10b. Path of the vortex center for the Reynolds and Froude number values Re = 100, Fr = 0.8. For comparison, Lamb's potential flow solution for a flat surface is included. The free-surface is plotted at the time t = 3.475, from Ohring and Lugt's results, 1991.

of positive vorticity at the scar should occur due to the changing sign of the surface curvature. This phenomenon can indeed be observed by returning to the vorticity contours of the flow displayed in Figure 5. The transport of the positive vorticity into the fluid is then controlled by the vorticity flux at the surface. This flux is relatively large, as indicated by the proximity of the different equivorticity lines.

A space-time representation of the free-surface wave can be observed in Figure 11. The space-time function is a standing wave, due to the vertical motion of the vortex. Finally, we have plotted the minimal value of vorticity (normalized with Reynolds number) against time in Figure 12. The curve follows a 1/2t decay, according to Equation (4.2), indicating that numerical diffusion is minimal.

4.3 Flow Simulation for $Re = 100,\ Fr = 1.125$

We have also carried out computations at the parameter values Re = 100, Fr = 1.125. The flow obtained is similar to the previous one, although at this higher Froude number, the free-surface can be more easily deformed, not resisting much to the ascension of the vortex. This phenomenon is illustrated in Figure 13 where the peak of the free-surface elevation is higher than 1 in the latest times of the computations (while it was smaller than one in the previous case). The vorticity distribution illustrates, as in the previous flow, the presence of negative vorticity due to the ascending vortex and the formation of positive vorticity around the scar area of the free-surface.

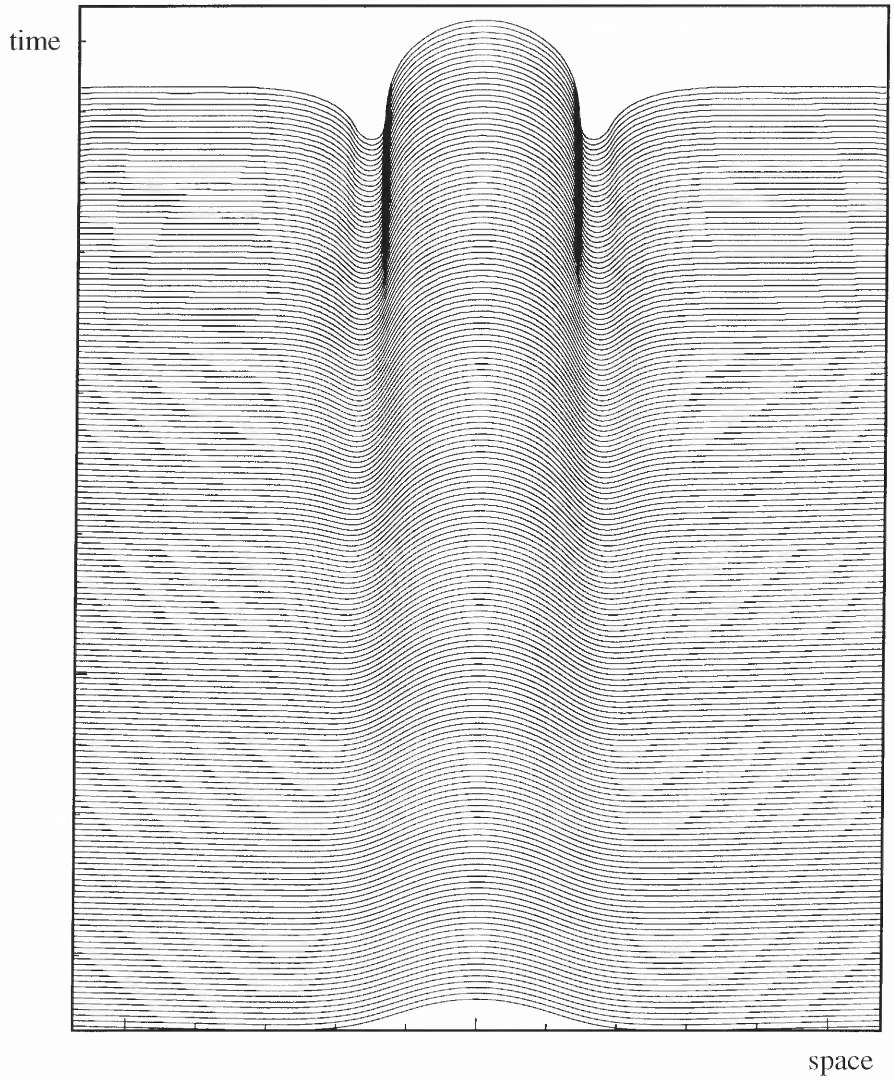

Figure 11. Space-time representation of the free-surface elevation, showing the formation of a standing wave. The Reynolds and the Froude number values are Re = 100, Fr = 0.8.

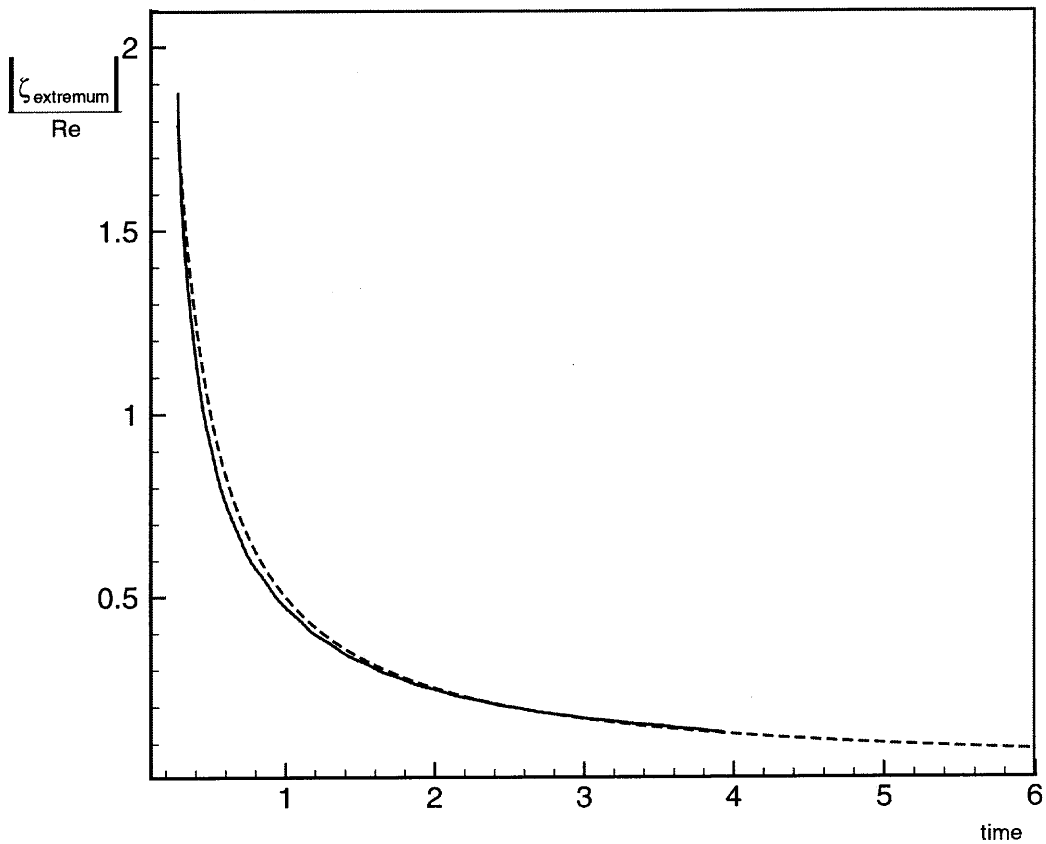

Figure 12. Time decrease of the vorticity value (normalized with the Reynolds number) at the center of the vortex for the Reynolds and the Froude number values Re = 100, Fr = 0.8 (solid line). The dashed line corresponds to 1/2t.

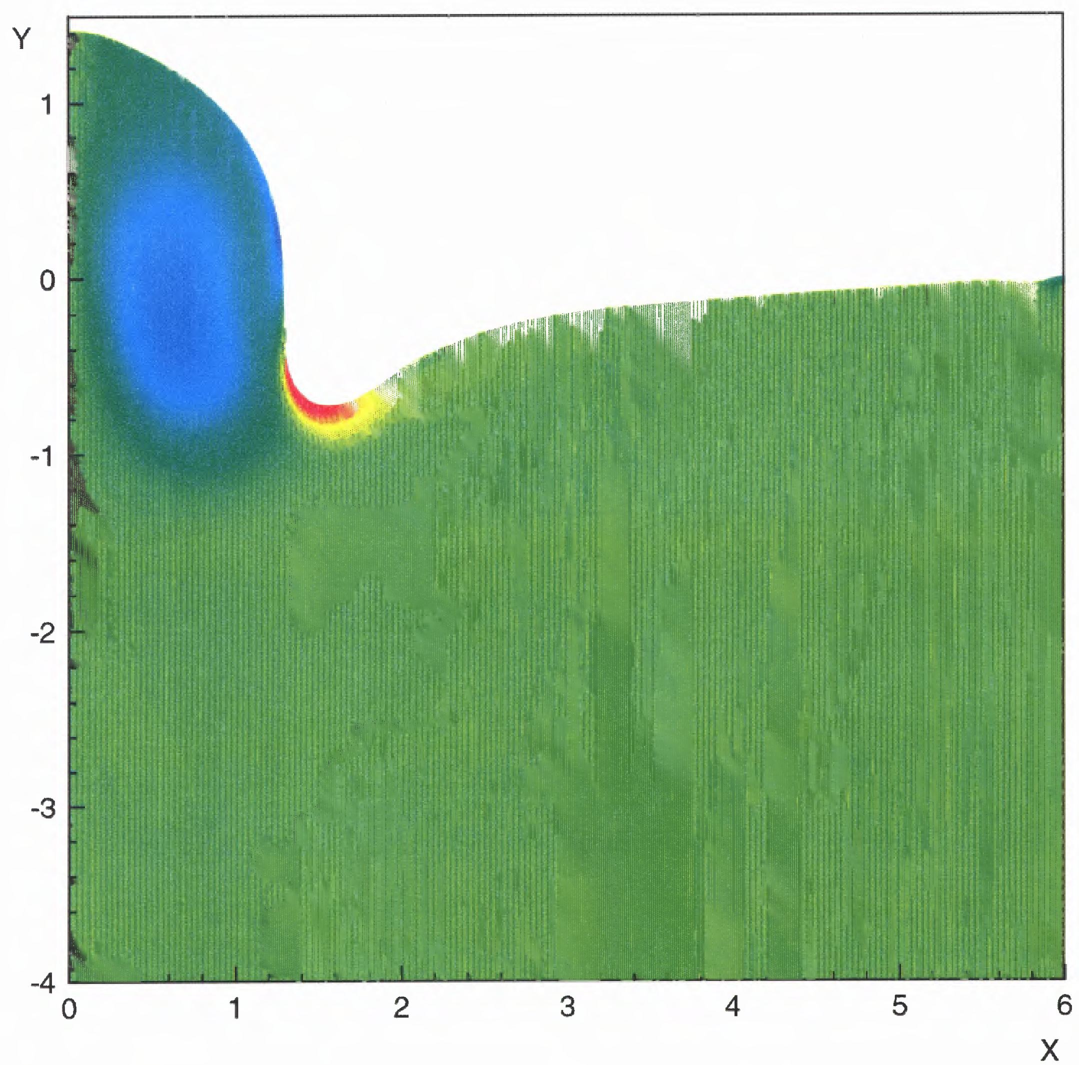

Figure 13. Vorticity distribution for the Reynolds and Froude number values Re = 100, Fr = 1.125, at time t = 4.2.

4.4 Flow Simulation for $Re = 500,\ Fr = 1.125$

Flow simulations were performed at Re = 500, Fr = 1.125 in order to investigate the influence of increasing Reynolds number on the solution. Two computational grids were used for these simulations (see Figure 14a). Figures 14 b,c permit the comparison between the computed flows with the two grids. A good agreement is found. The streamlines and kinetic energy distribution at t = 3.0 are plotted in Figure 14d. The mounded shape of the free-surface is larger than in the previous flow and the scars are more pointed, occupying a much more elongated region of the free-surface. As time increases (see Figure 14e for a similar plot at t = 3.10), the crest of the mound becomes wider, the descent to the scar much more abrupt (quasi-vertical) and the scars themselves more pointed and pronounced (deeper). A plot of the equi-vorticity contours in Figure 15 (top) shows negative vorticity in the primary vortex as well as along the vertical portion of the free-surface, while the positive vorticity region on the outer side of the scar is extremely elongated. The generation of many small, localized vortices of both positive and negative vorticity is also a new phenomenon, compared with flows at smaller Reynolds numbers.

4.5 Flow Simulation for $Re = 1000,\ Fr = 1.125,\ Fr = 2.0$

Our code has allowed us to investigate the flow for the Reynolds and Froude number values $Re = 1000$, $Fr = 1.125$. Figure 15 permits a direct comparison between the equi-vorticity lines of this flow and those of the previous flow. Similar features are observed just before the computation stops, although one can observe the generation of a multitude of secondary vortices in the flow. In addition, the vertical portion of the free-surface is higher, while the curved crest has become flatter. The (quasi-vertical) trajectory of the center of the vortex is plotted in Figure 16 while the velocity field itself is displayed in Figure 17a. The space-time representation of the free-surface displays a standing wave (see Figure 17b). The streamlines and kinetic energy distribution of the flow can be observed in Figures 18 a,b with a zoom on the primary vortex in Figure 18c. The results shown in Figures 18 a,b are obtained by using two different computational grids. We observe that the computations are all numerically stable. Comparable results are obtained for a slightly higher Froude number value, $Fr = 2.0$ (Figure 19).

4.6 Flow simulation for $Re = 2000,\ Fr = 1.125$

Numerical simulations for the Reynolds and Froude number values $Re = 2000$, $Fr = 1.125$ have been performed successfully with different computational grids. The two grids used are displayed in Figure 20a and the two computational flows are shown in Figure 20b. A good agreement between the two computations was found. A vectorial representation of the velocity field is displayed in Figure 20c, showing similarities with previously computed flows. It is difficult to see the effect of increasing Reynolds number on the velocity or kinetic energy of the flow. Indeed, as Reynolds number increases, small scale eddies gain energy and the flow becomes turbulent. These changes can be observed more clearly on vorticity contours (see the third row of Figure 20b). The statistical properties of the turbulent field will be explored in Chapter 5. The increase of Froude number corresponds to a more deformable free-surface as shown by our computation for $Fr = 3.0$ (see Figure 20d).

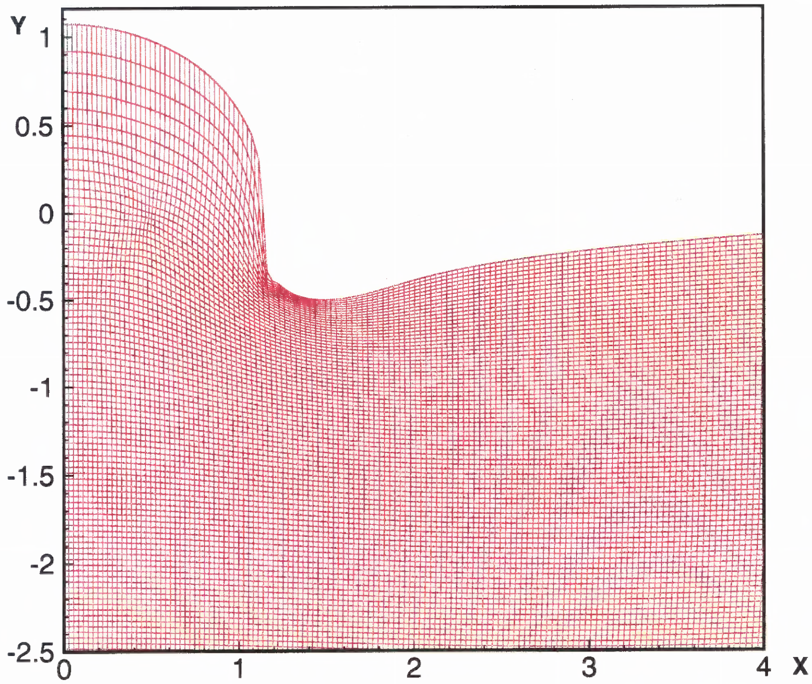

Section of the grid (mesh: 231x191).

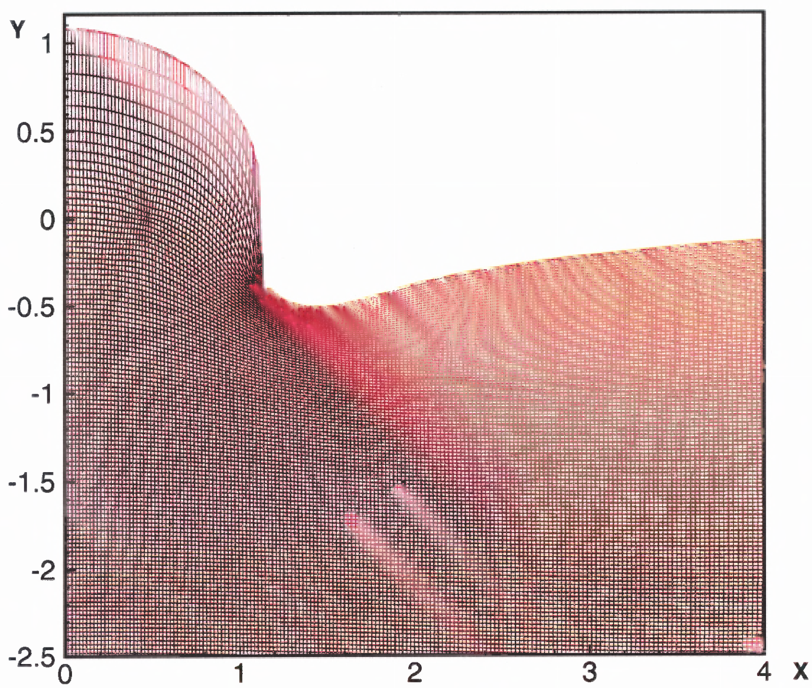

Section of the grid (mesh: 286x236).

Figure14a. Section of the computational grids used for the study of numerical convergence at the Reynolds and Froude number values Re = 500, Fr = 1.125, at time t = 3.00.

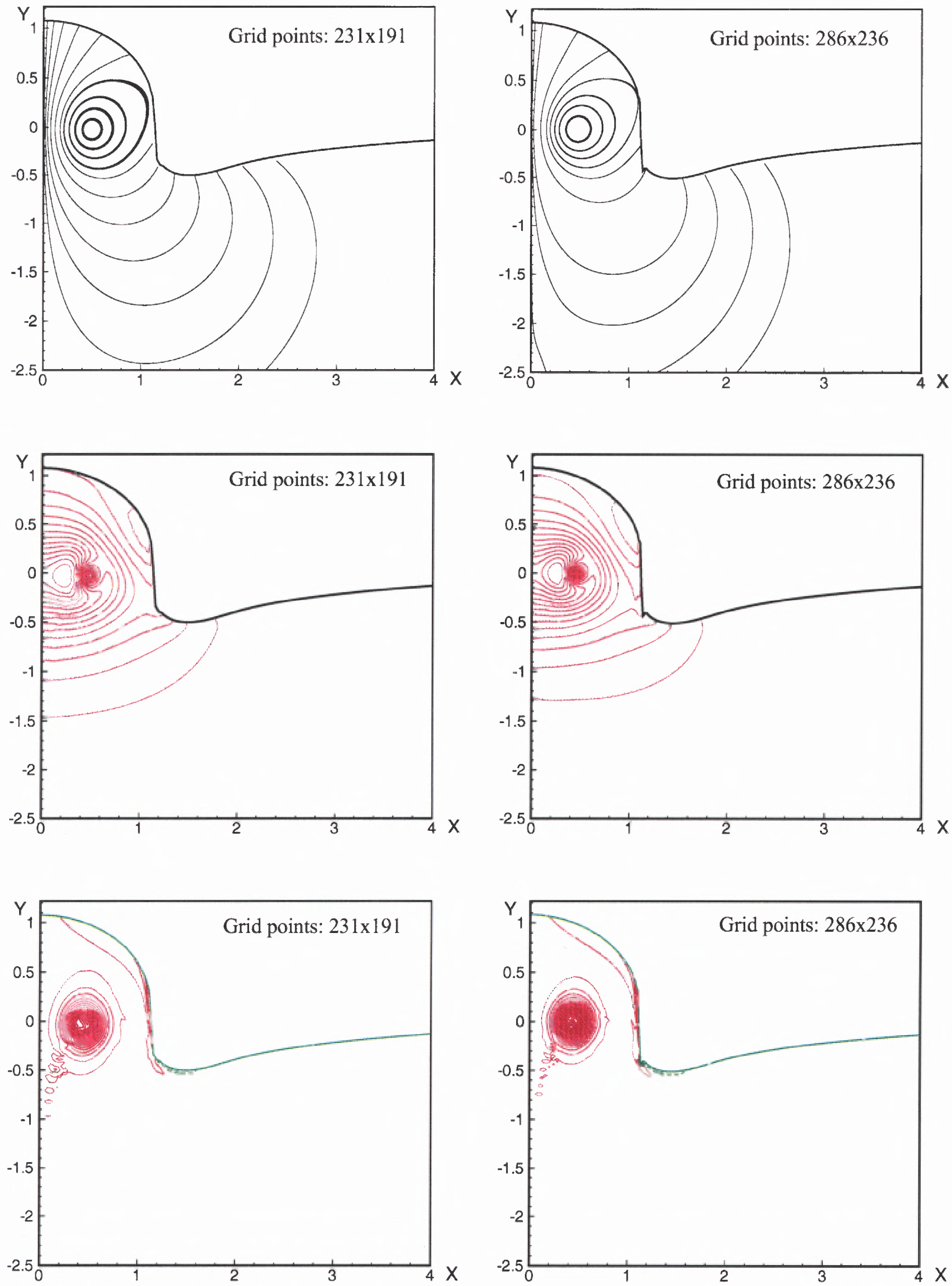

Figure 14b. Comparison of the flows computed with two computational grids displayed in Figure14a, showing good agreement between the two results. First row: streamlines of the flow, second row: contours of the square root of the kinetic energy of the flow, third row: equi-vorticity lines (solid lines: negative vorticity, dashed lines: positive vorticity).

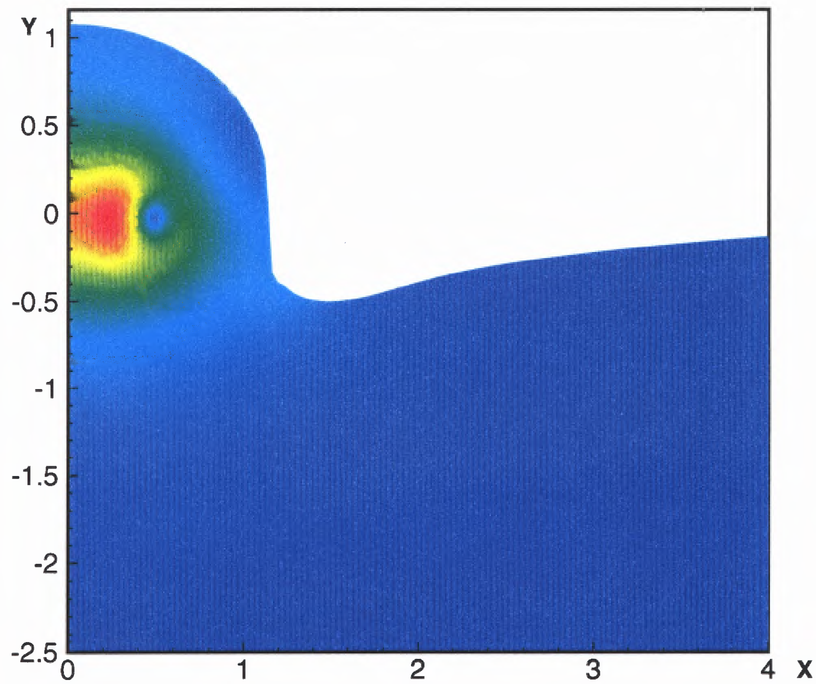

Grid points: 231x191

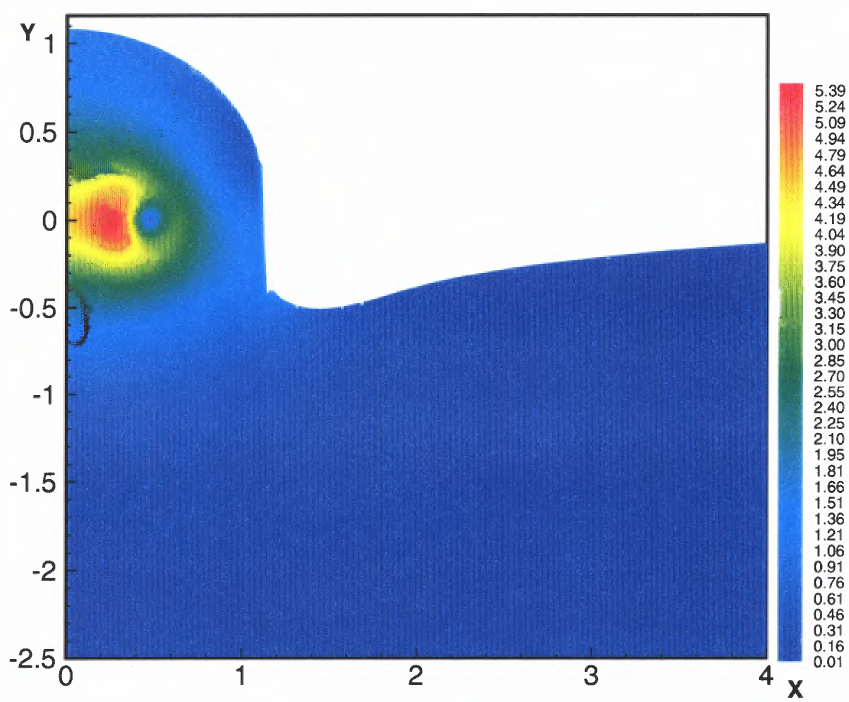

Grid points: 286x236

Figure 14c. Contours of the square root of the kinetic energy of the flow described in the caption of Figure14a, for the two different meshes displayed in Figure14a, showing the similarity of the flow computed by using different meshes.

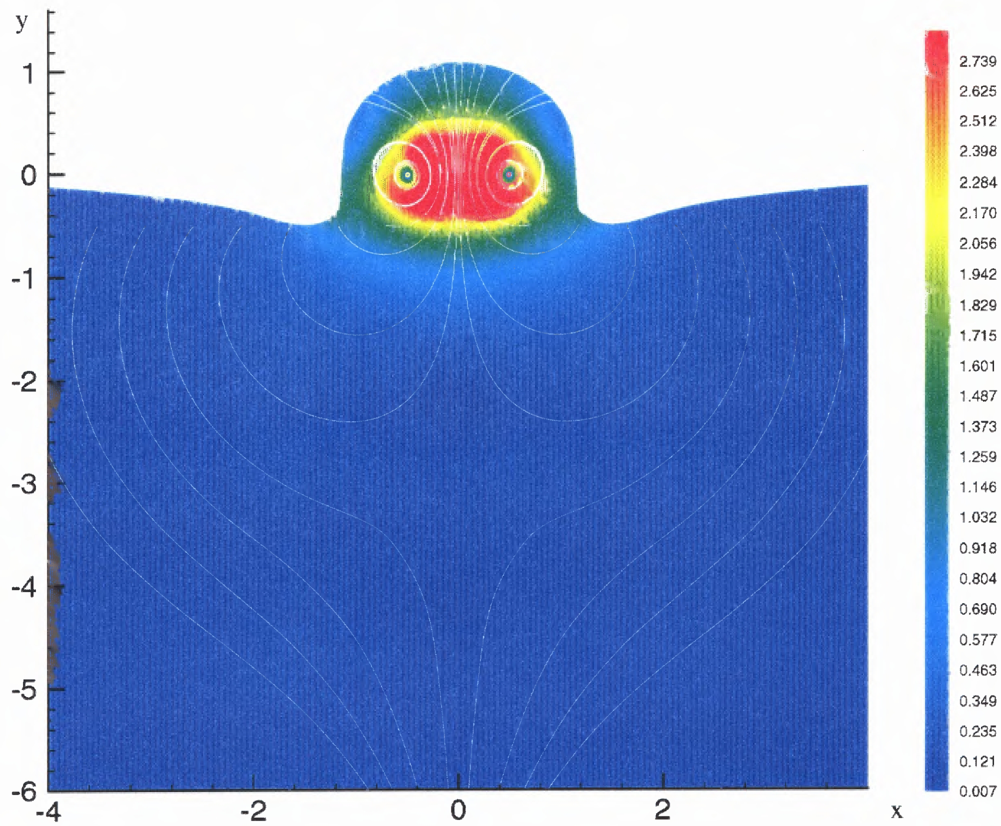

Figure 14d. Streamlines and square root of the kinetic energy distribution for the Reynolds and Froude number values Re = 500, Fr = 1.125 at time t = 3.00.

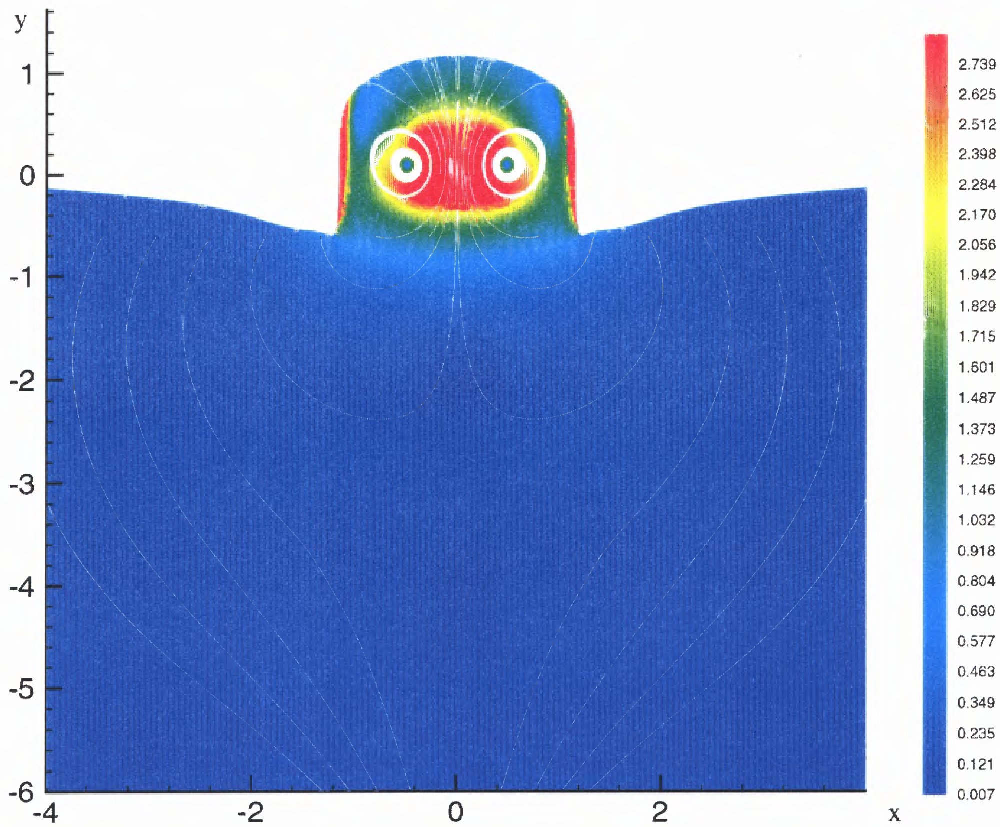

Figure 14e. Streamlines and square root of the kinetic energy distribution for the Reynolds and the Froude number values Re = 500, Fr = 1.125, at time t = 3.10.

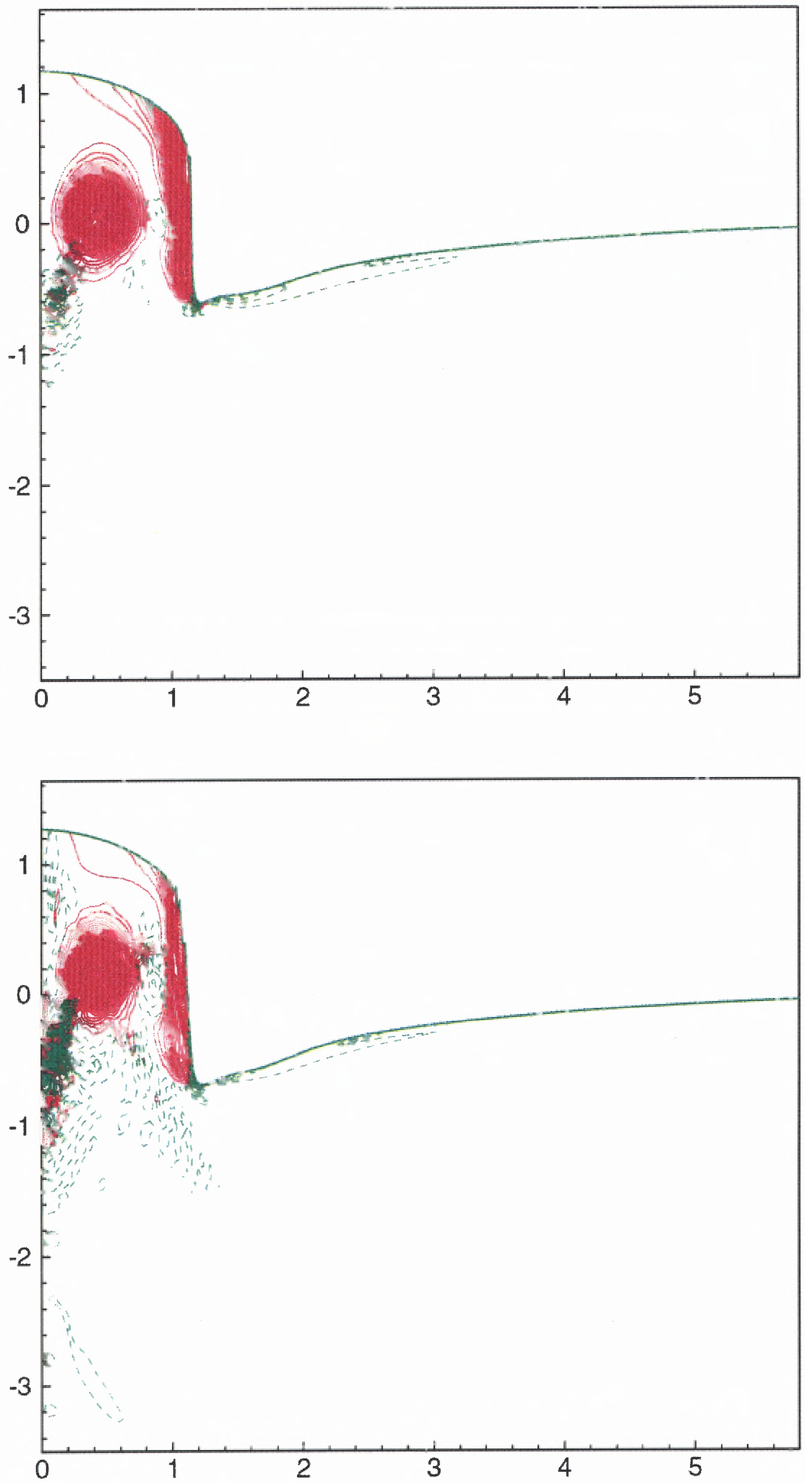

Figure 15. Equi-vorticity contours for the Reynolds and Froude number values Re = 500, Fr = 1.125 at time t = 3.10 at which the simulation stopped (top) and for the Reynolds and the Froude number values Re = 1000, Fr = 1.125 at time t = 3.196 at which the simulation stopped (bottom). Positive and negative vorticity are represented by dashed and solid lines, respectively.

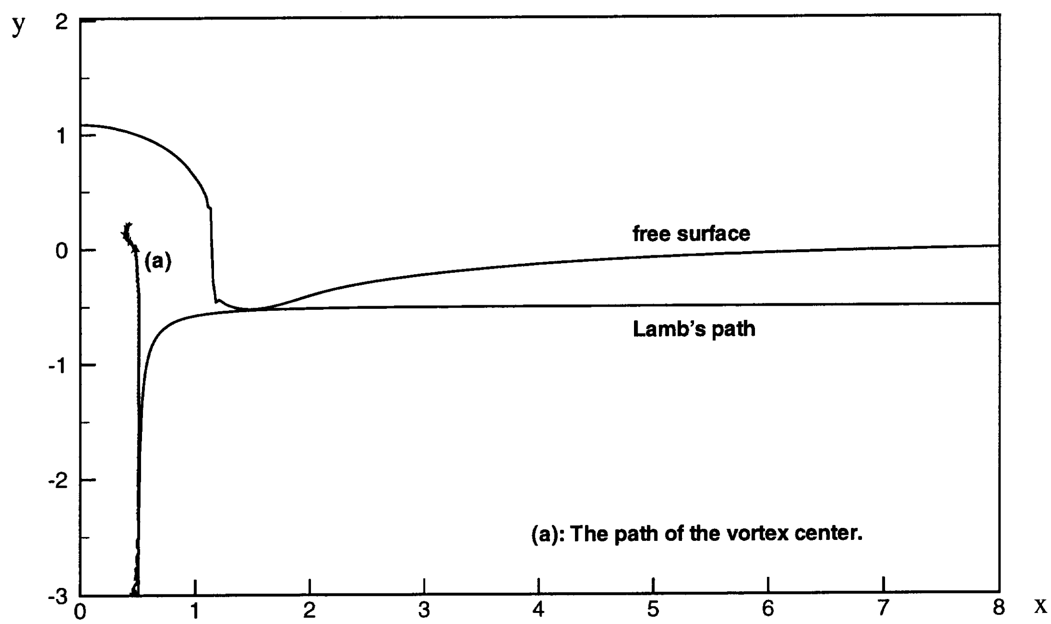

Figure 16. Path of the vortex center for Re = 1000, Fr = 1.125. For comparison, Lamb's potential flow solution for flat surface is included. The free-surface is plotted at time t = 3.0 for a 231x191 computational grid.

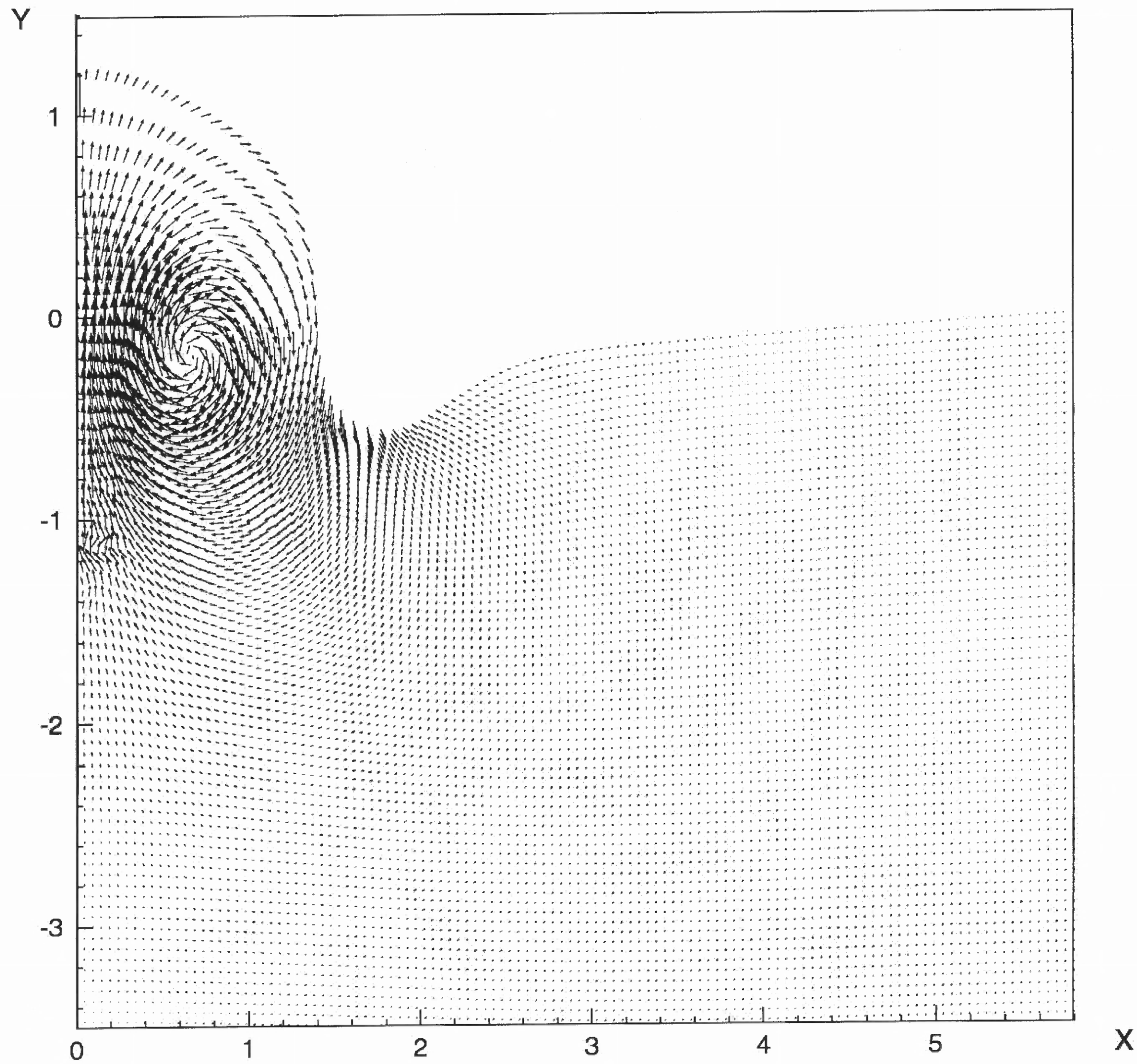

Figure 17a. Vectorial representation of the velocity field for the Reynolds and Froude number values Re = 1000, Fr = 1.125, at time t = 3.8.

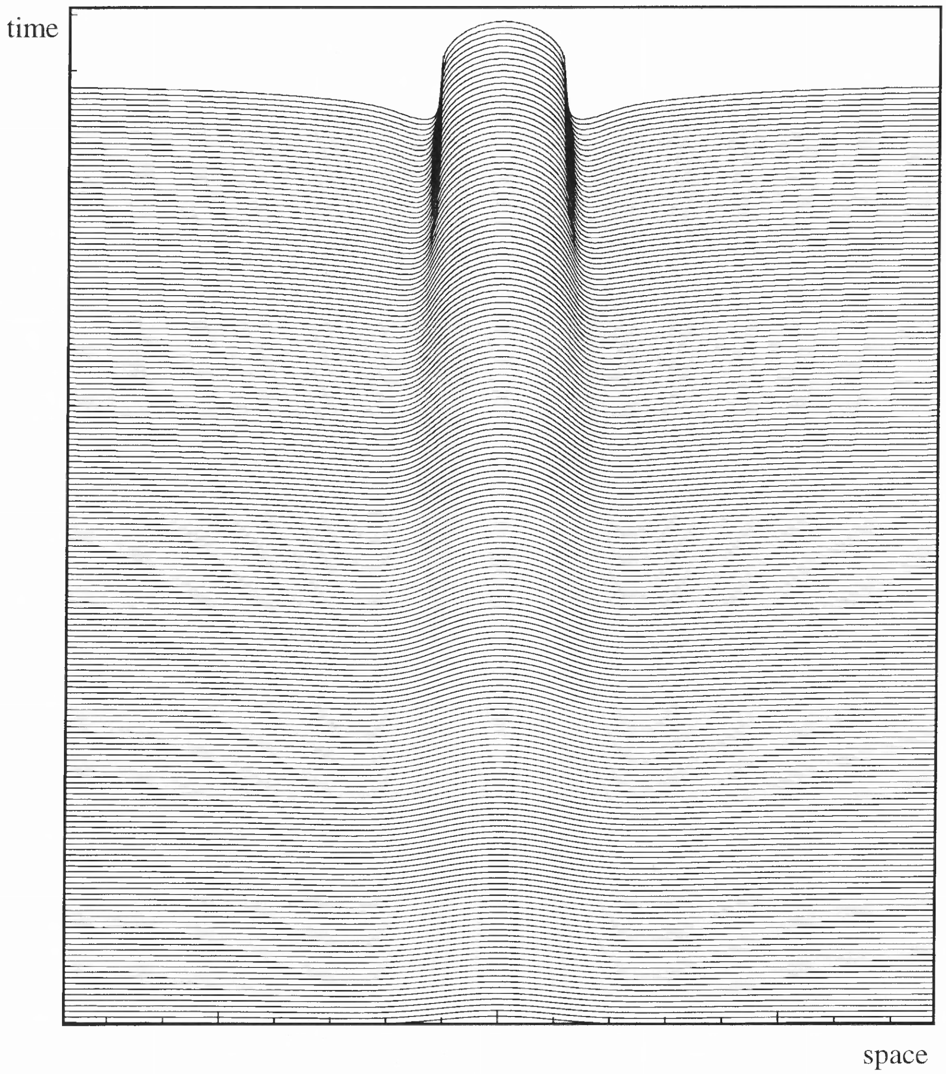

Figure17b. Space-time representation of the free-surface elevation at the Reynolds and Froude number values Re = 1000, Fr = 1.125.

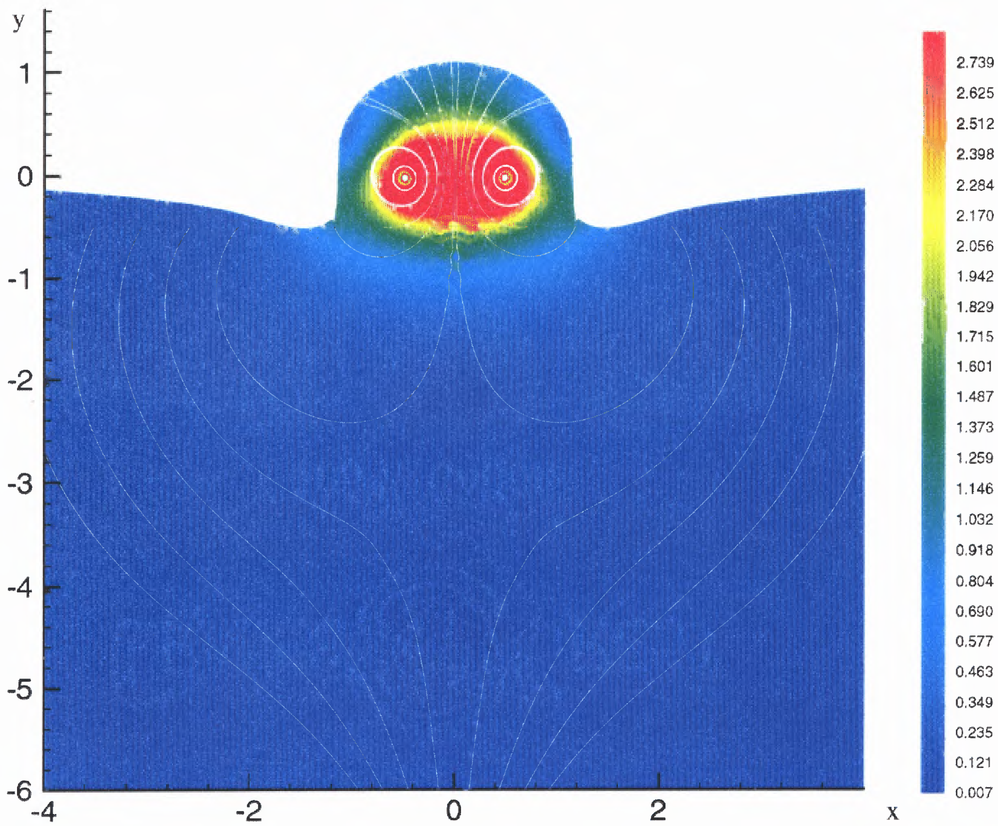

Figure 18a. Streamlines and square root of the kinetic energy distribution for the Reynolds and Froude number values Re = 1000, Fr = 1.125, at time t = 3.00. The size of the computational grid is 231x191.

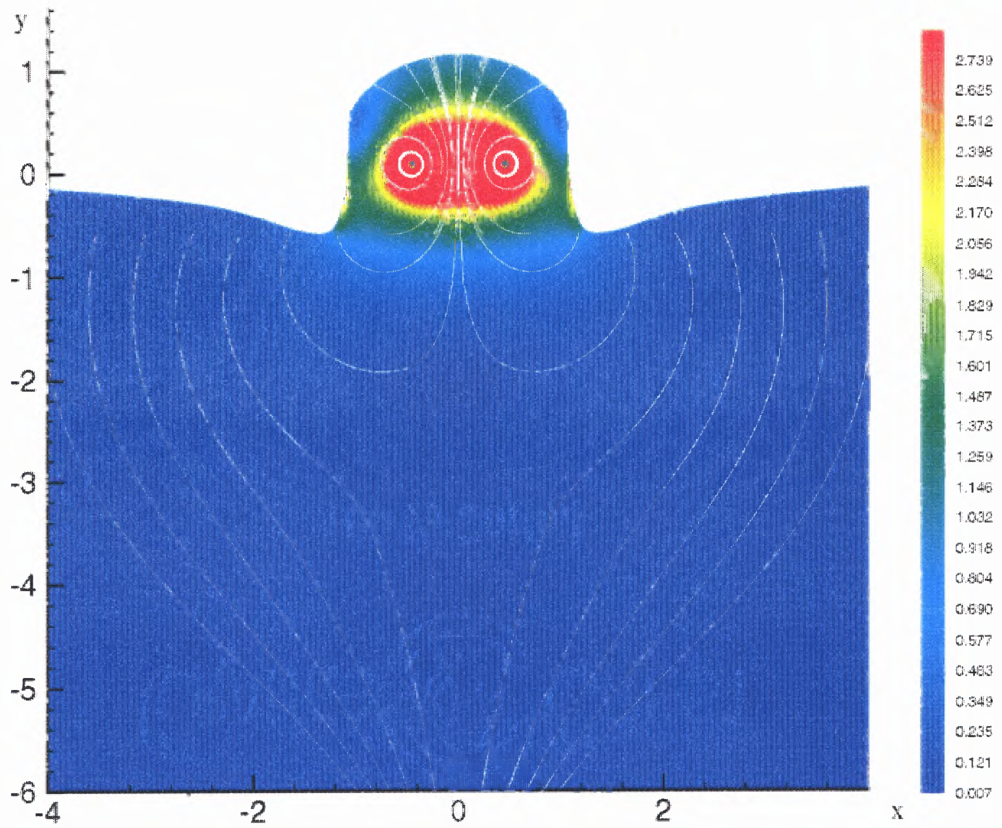

Figure 18b. Streamlines and square root of the kinetic energy contours of the flow for the Reynolds and Froude number values Re = 1000, Fr = 1.125, at time t = 3.04, corresponding to a 271x226 computational grid.

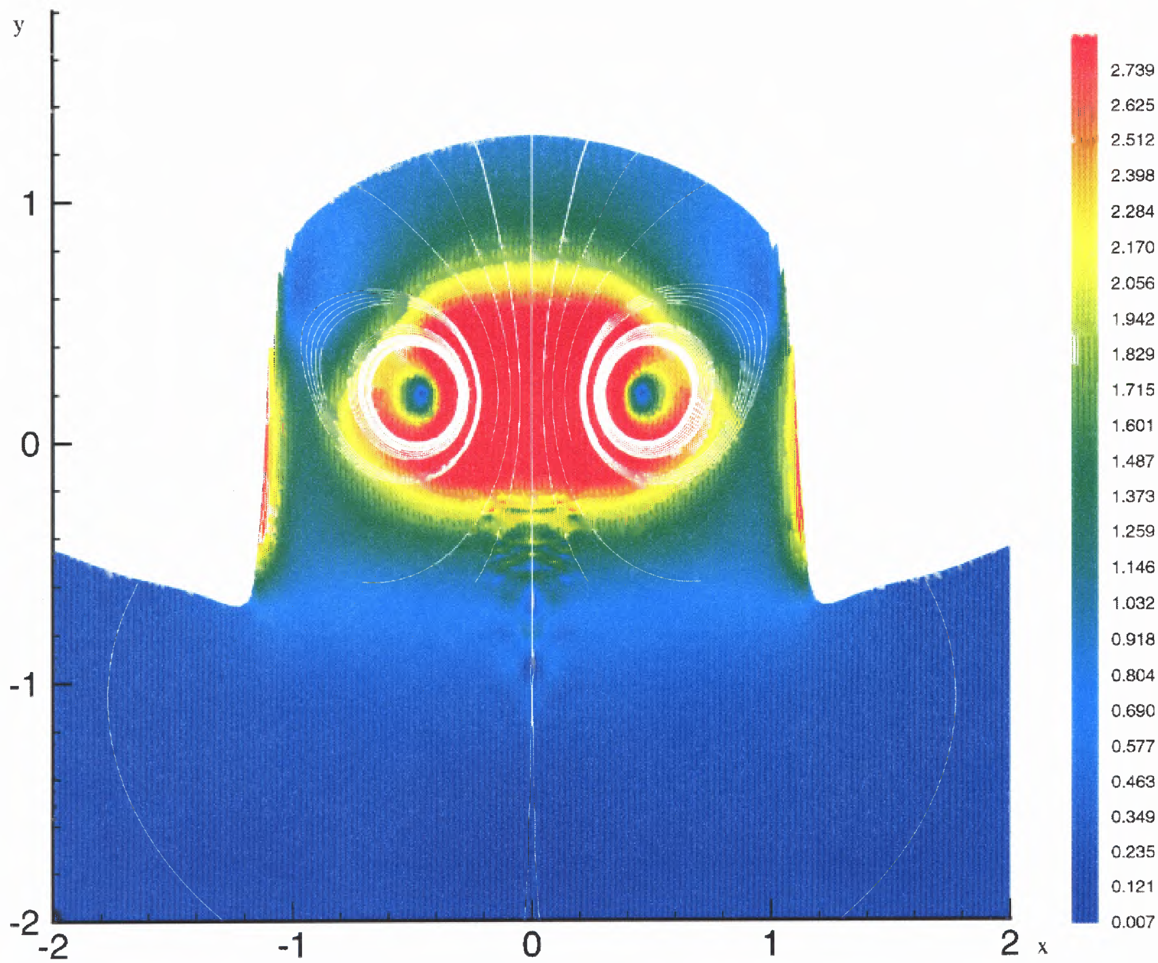

Figure 18c. Streamlines and square root of the kinetic energy distribution for the Reynolds and Froude number values Re = 1000, Fr = 1.125, at time t = 3.196.

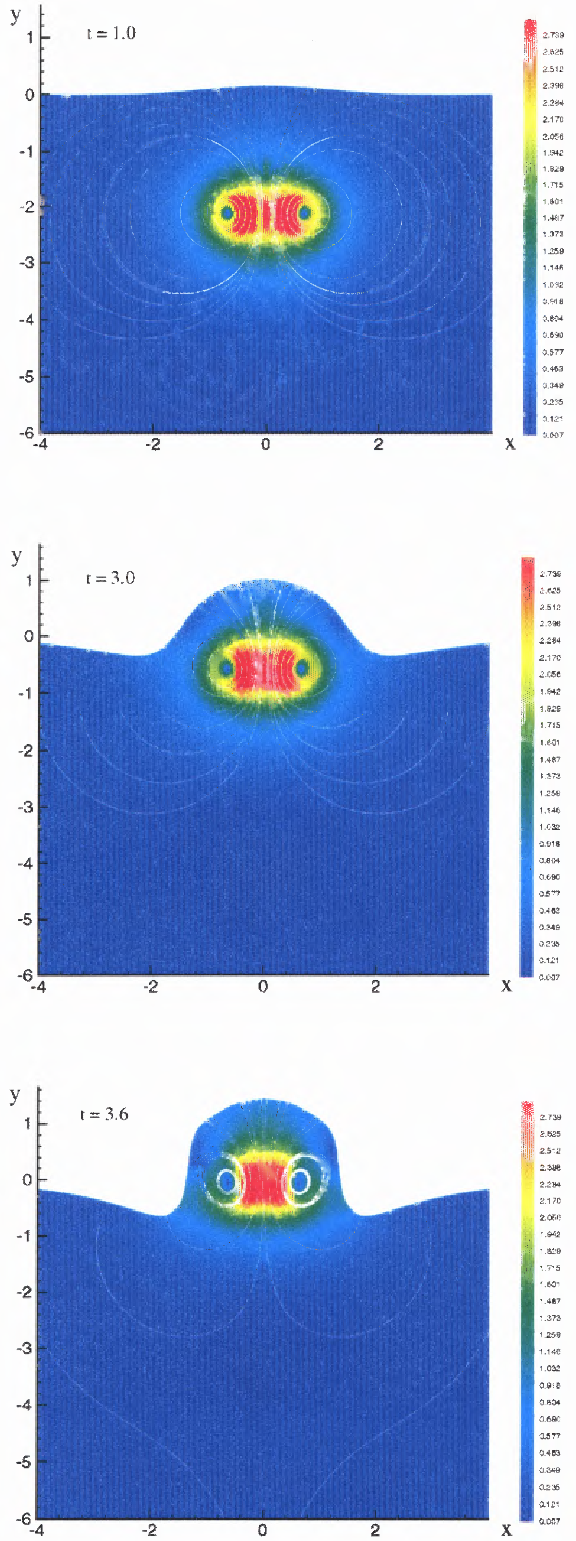

Figure 19. Streamlines and square root of the kinetic energy distribution for the Reynolds and Froude number values Re = 1000, Fr = 2.0 at different times.

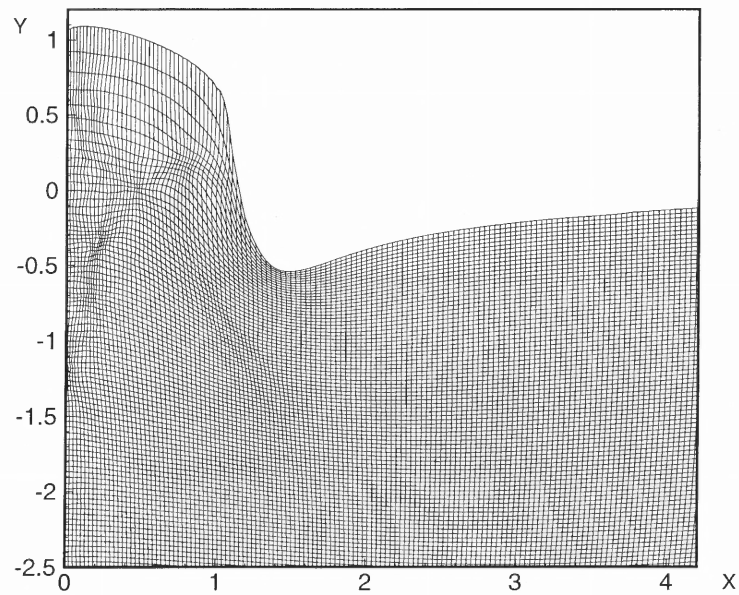

section of the grid (mesh: 231x191).

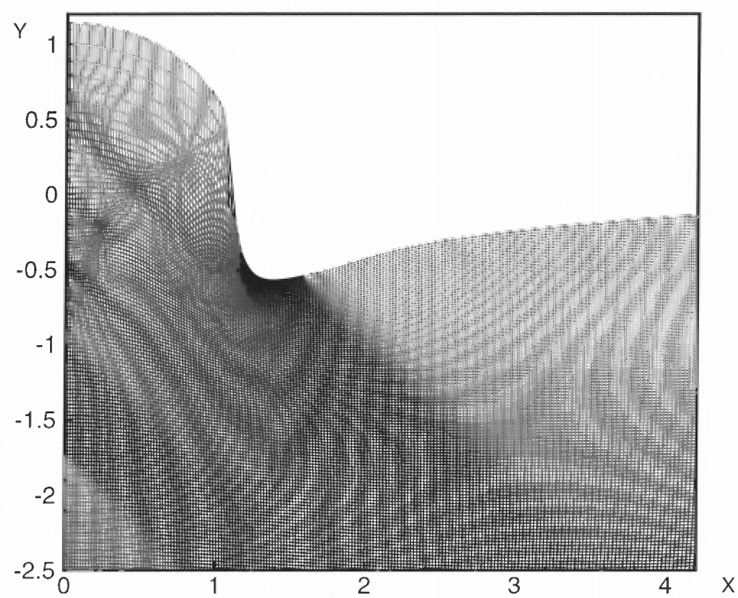

section of the grid (mesh: 311x261).

Figure 20a. Section of the computational grids used for the study of numerical convergence at the Reynolds and Froude number values Re = 2000, Fr = 1.125, at time t = 3.00.

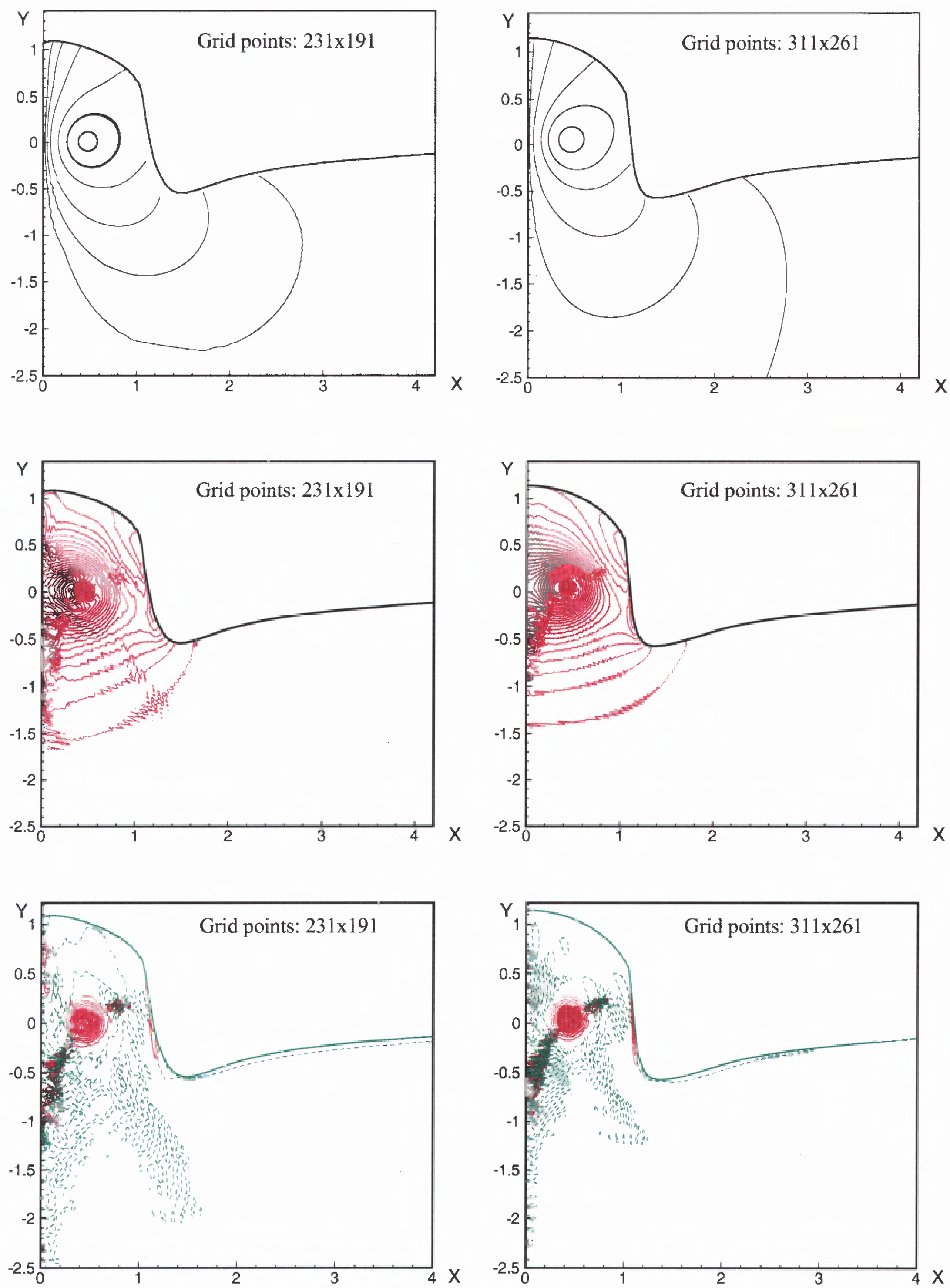

Figure 20b. Comparison of the flows computed with the two computational grids displayed in Figure 20a, showing good agreement between the two computations. First row: streamlines of the flow, second row: contour lines of the square root of the kinetic energy of the flow, third row: equi-vorticity lines (solid lines: negative vorticity, dashed lines: positive vorticity).

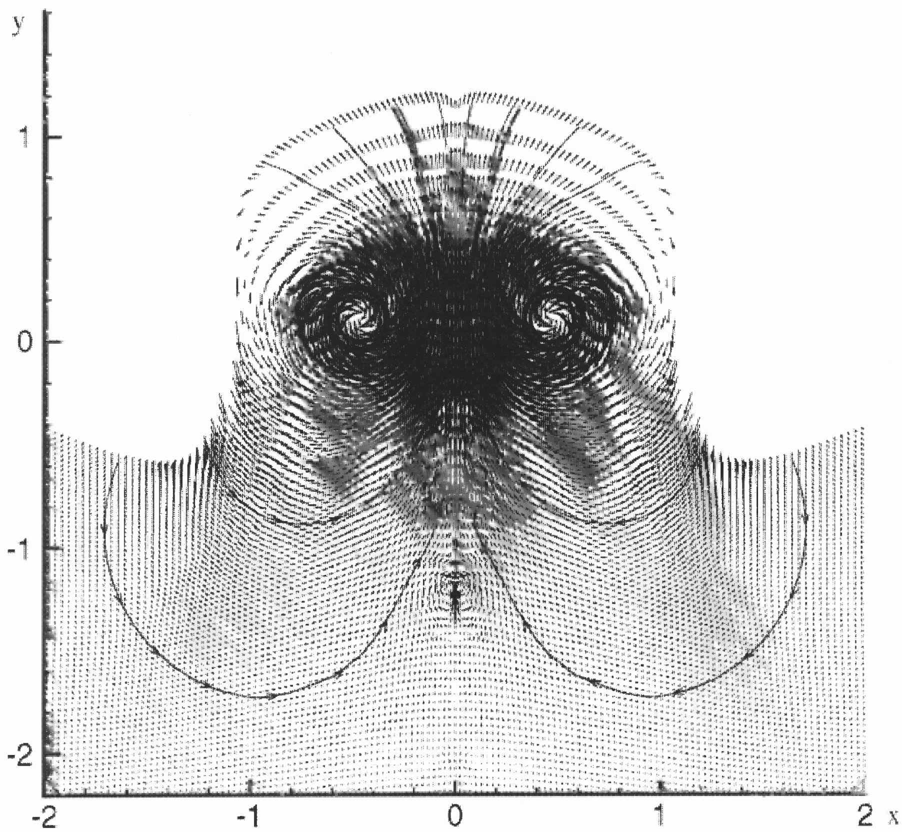

Figure 20c. Vectorial representation of the velocity field and streamlines of the flow for the Reynolds and Froude number values Re = 2000, Fr = 1.125, at time t = 3.082.

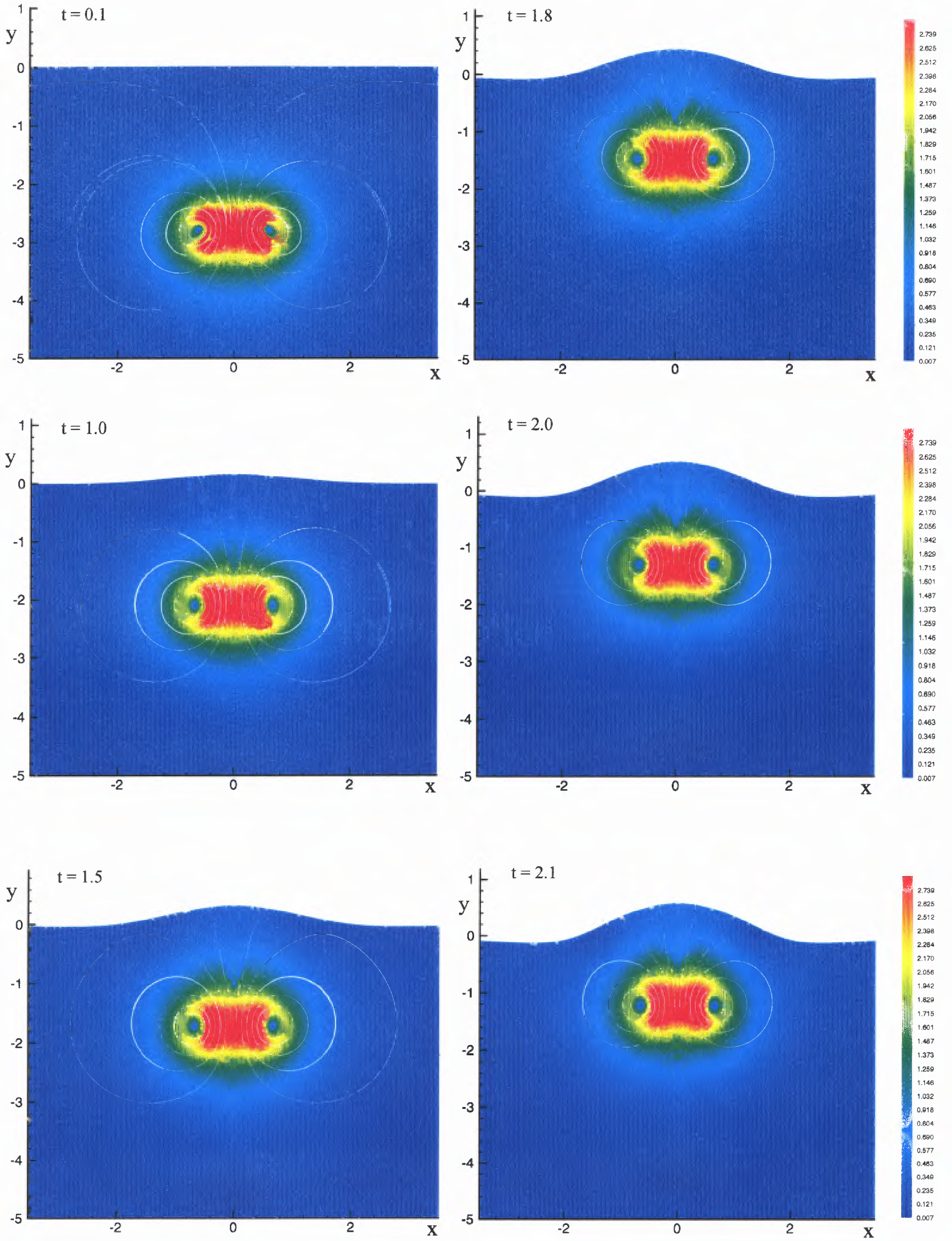

Figure 20d. Time evolution of the flow for the Reynolds and Froude number values Re = 2000, Fr = 3.00. Here, the streamlines and contours of the square root of the kinetic energy of the flow are displayed at different times.

CHAPTER 5

GENERATION OF TURBULENCE

In this chapter, we investigate the turbulent field developed in the free-surface flow at relatively high Reynolds number values, during the interaction between the vortex pair and the deformed free-surface. As Reynolds number increases, more and more secondary vortices are produced and turbulence develops.

In order to investigate the turbulence field, we need to explore the statistics of the flow. Hereafter, the latter are computed by considering the average over the horizontal (x-) direction. For any variable $\phi(x,y,t)$, $\overline{\phi}(y,t)$ denotes the average over the horizontal direction, while $\phi'(x,y,t)=\phi(x,y,t)-\overline{\phi}(y,t)$ denotes the instantaneous fluctuation.

As a rough estimate based on the theory of isotropic homogeneous turbulence (Tennekes & Lumley 1972), we can obtain the (dimensionless) Kolmogorov scale:

$$\tilde{\kappa} \sim \ell Re^{-3/4} \approx 0.034 \qquad (5\text{-}1)$$

for Re = 1000, where ℓ stands for the integral (large eddy) scale. In our numerical simulation, the grid size in the main part of the domain is

$$\Delta x = \Delta y = 0.025 \text{ for a 231x191 grid,} \qquad (5\text{-}2)$$

which is of the same order as the Kolmogorov scale.

It is clear that turbulence has developed at the Reynolds number value $Re = 1000$ (see also L. Shen, X. Zhang, D. K. P. Yue and G. S. Triantafyllou 1999). Figure 21 displays the turbulence kinetic energy dissipation, turbulence intensity distribution, the turbulence intensities and the mean flow profiles for the Reynolds and Froude number values $Re = 1000$, $Fr = 1.125$.

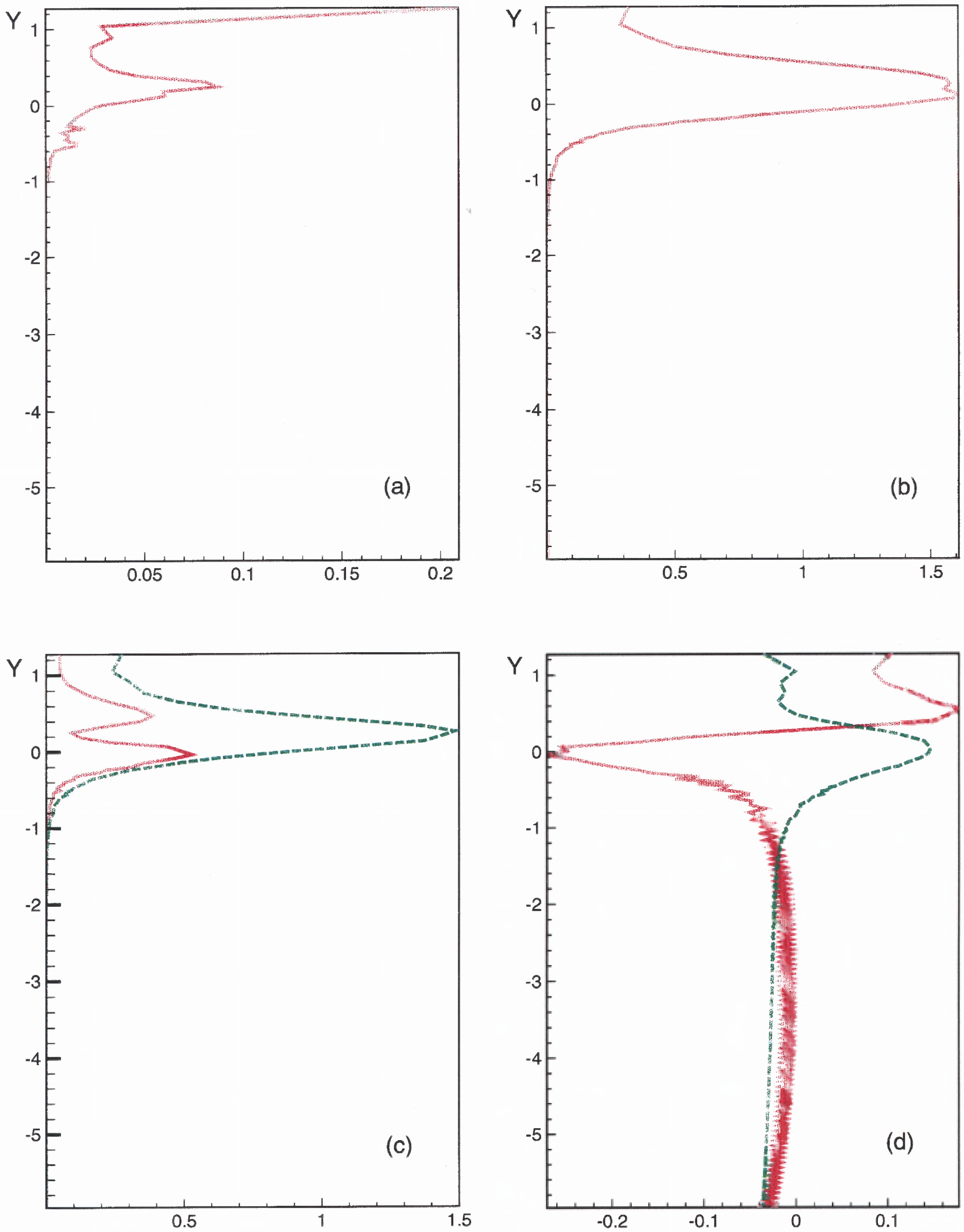

Figure 21. Characteristics of the turbulent field for the Reynolds and Froude number values Re = 1000, Fr = 1.125, at time t = 3.196. (a) Turbulent kinetic energy dissipation, (b) Turbulence intensity, (c) Mean square of the velocity fluctuation components (horizontal component: solid line; vertical component: dashed line), (d) Mean flow velocity profile (horizontal component: solid line; vertical component: dashed line).

It is interesting to notice that the turbulence kinetic energy dissipation

$$D = \frac{1}{Re}\overline{\frac{\partial u_i^{'}}{\partial x_j}\cdot\frac{\partial u_i^{'}}{\partial x_j}} \tag{5-3}$$

increases rapidly as the distance to the free-surface decreases and reaches its maximal value at the free-surface. This is in agreement with the weakening of the strong kinetic energy at the free-surface.

Furthermore, the turbulence intensity distribution

$$q'^2 = \overline{u'^2 + v'^2} \tag{5-4}$$

is close to zero at large depths below the center of the primary vortices where the fluid is quiescent. As one approaches the free-surface, it increases and reaches two maxima, one at the level of the center of the point vortex, the other one (higher than the first one) at the free-surface.

Finally, it is worth mentioning that the turbulence intensity (or turbulence kinetic energy) mainly consists of its vertical component, $\overline{v'^2}$, whose maximal value is also reached at the level of the center of the primary vortices. This is somewhat contradictory with the following "feature" of free-surface turbulence previously reported by other authors. Others have indeed observed an increase in the horizontal velocity fluctuation at the expense of the vertical velocity fluctuation at the free-surface. This discrepancy is due to the fact that our Froude number is relatively large and that our treatment of the free-surface permits large vertical deformations of the latter.

Finally, we summarize our results as follows:

1) the turbulence region is concentrated in a surface layer located below the free-surface and around the center of the primary vortices;

2) The maximal turbulent kinetic energy dissipation occurs at the highly deformed free-surface, while a second local maximum is observed near the center of the primary vortices;

3) The turbulence intensity reaches its maximal value near the center of the primary vortices, and it is non-zero at the free-surface;

4) The turbulence intensity at the free-surface and in the surface layer mainly consists of its vertical component, $\overline{v'^2}$, which has a sharp maximum near the center of the primary vortices;

5) Below the center of the primary vortices, both the turbulence dissipation and turbulence intensity decrease to zero rapidly as the distance to the free-surface increases.

CHAPTER 6

CONCLUDING REMARKS

In conclusion, the interaction between a pair of vortices and a highly deformable free-surface has been numerically simulated by using a finite difference scheme with an adaptive grid technique. The Froude and Reynolds numbers considered here are larger than those considered in past numerical simulations. The success of our numerical scheme is due to an adaptive mesh and a highly implicit technique. In addition, we gave careful consideration to numerical stability which was crucial to the successful numerical simulation of the highly nonlinear, unsteady and moving boundary fluid flow problem considered in this thesis. The free-surface boundary condition is fully non-linear, thus allowing the free-surface to deform until its slope becomes very large (corresponding, in nature, to wave breaking). Reynolds numbers higher than those reached by previous numerical simulations are considered, up to $Re = 1000$. In most cases, Froude number is kept at the value of $Fr = 1.125$, although runs at different values were also performed in order to determine the influence of the latter on the flow.

For all parameter values explored in this work, the vortex pair always starts its motion by approaching the free-surface, following Lamb's solution during the early stage of its ascension. At very low Reynolds numbers, the vortices turn around and rebound away from the free-surface. The rebounding phenomenon, however, is absent in high Reynolds number flows; in this case, the vortex pair trajectory is almost vertical.

As the vortex pair ascends, it deforms the free-surface, forming a domed area around the symmetric line until the slope of the free-surface becomes so steep that the free-surface breaks down (which, of course, does not happen in the computation due to the presence of the singularity in the derivative of the free-surface elevation). The larger the Reynolds number is, the higher the (almost) vertical part of the free-surface becomes.

Meanwhile, the curved part of the free-surface flattens. Above a certain Reynolds number threshold, the elevation of the free-surface is accompanied by depressions on both sides of the dome. The depressions become more and more pointed, forming a cusp-like shape at the highest Reynolds number values.

At high Reynolds number values, the large free-surface deformation triggers the generation of strong vorticity at the free-surface. While the vorticity is negative below the domed area, the vorticity is positive at the scar. This sign difference can be explained by the change of curvature of the free-surface elevation. One can observe the generation of vorticity in Figure 22 where the free-surface vorticity is plotted as a function of position, at three various times, for Re = 100, Fr = 0.8 and Fr = 1.125. The vorticity at the interface is initially zero and develops a significant jump from negative to positive values at later times. Figure 23 displays similar plots at various Reynolds number values, Re = 100, 500, 1000, and Fr = 1.125. It is clear that as Reynolds number increases, the vorticity jump becomes narrower. In addition, the formation of positive vorticity below the scar increases significantly with Reynolds number, the peak being at about ξ = 5 at $Re = 100$, ξ = 100 and larger at Re = 500 and 1000. The negative vorticity corresponding to the domed area also increases as Reynolds number increases to Re = 500, but decreases from Re = 500 to Re = 1000. This decrease of vorticity may be due to vortex interaction as many small vortices are generated at this high Reynolds number. It is also interesting to notice that the vorticity at the free-surface is always higher in absolute value than the vorticity which has generated it, that is below the free-surface. The variation of the kinetic energy at the free-surface with the Reynolds number can be can be observed in Figure 24. In all cases, the kinetic energy is very small, except over small distance. In this short interval, the kinetic energy is rather small at Re = 100, increasing significantly at Re = 500, but decreases again as Reynolds number increases beyond Re = 500. This decrease is due to the increase of the turbulent kinetic energy dissipation, as described in Chapter 5.

Regarding the generation of turbulence, the following remarks could be made:

- the turbulence region is concentrated in a surface layer located below the free-surface and around the center of the primary vortices.
- The maximal turbulence kinetic energy dissipation occurs at the highly deformed free-surface, while a second local maximum is observed near the center of the primary vortices;
- The turbulence intensity reaches its maximal value near the center of the primary vortices, and it is non-zero at the free-surface;
- The turbulence intensity at the free-surface and in the surface layer mainly consists of its vertical component, $\overline{v'^2}$, which has a sharp maximum near the center of the primary vortices;
- Below the center of the primary vortices, both the turbulence dissipation and turbulence intensity decrease to zero rapidly as the distance to the free-surface increases.

Finally, the effect of Froude number can be understood as follows. At low Froude numbers, the free-surface is stiff, acting as a barrier to the ascending vortex pair. In contrast, larger Froude numbers correspond to a highly deformable free-surface. At large Reynolds numbers for which the surface deformation is very large, a way to decrease such a deformation is to decrease Froude number. In this case, the free-surface deformation can be considered very small, as in many previous works. In the latter, the free-surface is assumed to remain either flat or deform linearly. This assumption breaks as Froude number increases.

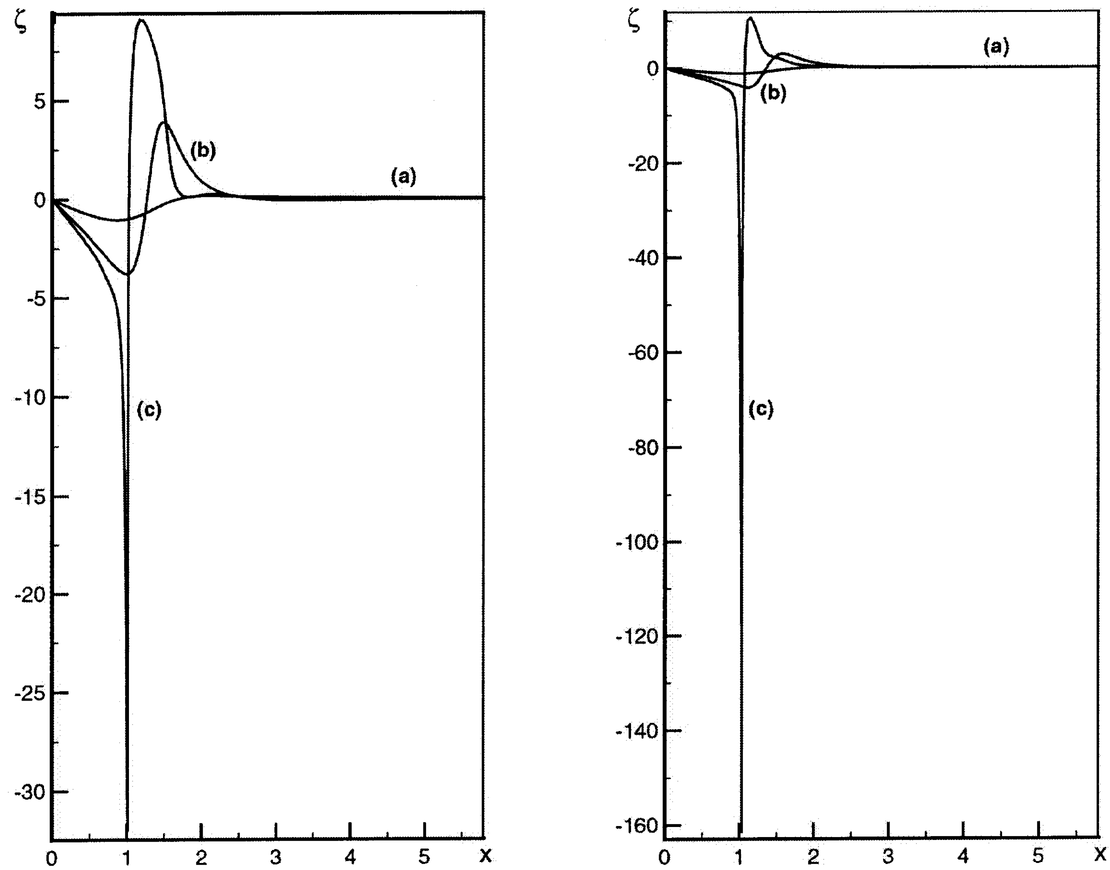

Figure 22. Free-surface vorticity versus horizontal position for different Froude numbers at the Reynolds number value. Left: Free-surface vorticity for the Froude number value Fr = 0.8, at times (a) t = 2.0, (b) t = 3.0, (c) t = 3.65 (the last moment). The extremal vorticity value below the free-surface is: -23.54 at t = 2.0, -16.77 at t = 3.0, -13.89 at t = 3.65, right: Free-surface vorticity for the Froude number value Fr = 1.125, at times (a) t = 2.0, (b) t = 3.0, (c) t = 3.57 (the last moment). The extremal vorticity value below the free-surface is: -24.40 at t = 2.0, -17.20 at t = 3.0, -14.61 at t = 3.57.

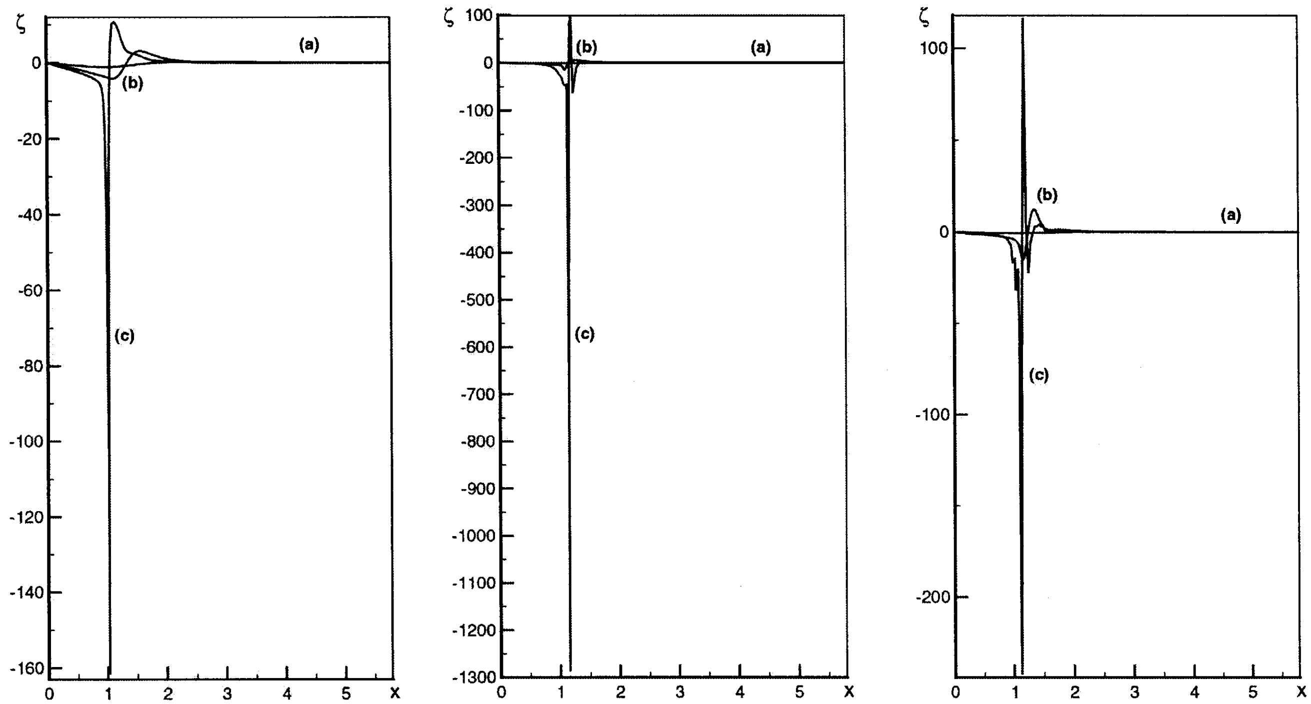

Figure 23. Free-surface vorticity versus horizontal position for the Froude number value Fr = 1.125 for different Reynolds numbers. It can be observed that for higher Reynolds number, the free-surface vorticity can be much larger than the vorticity values below the free-surface. Left: Free-surface vorticity for the Reynolds number value Re = 100, at times (a) t = 2.0, (b) t = 3.0, (c) t = 3.57 (the last moment). The extremal vorticity value below the free-surface is: = -24.40 at t = 2.0, -17.20 at t = 3.0, -14.61 at t = 3.57. Center: Free-surface vorticity for the Reynolds number value Re = 500, at times (a) t = 1.5, (b) t = 3.0, (c) t = 3.1 (the last moment). The extremal vorticity value below the free-surface is: -80.39 at t = 1.5, -54.65 at t = 3.0, -53.30 at t = 3.1. Right: Free-surface vorticity for the Reynolds number value Re = 1000, at times (a) t = 1.5, (b) t = 3.0, (c) t = 3.196 (the last moment). The extremal vorticity value below the free-surface is: -102.4 at t = 1.5, -80.42 at t = 3.0, -59.38 at t = 3.196.

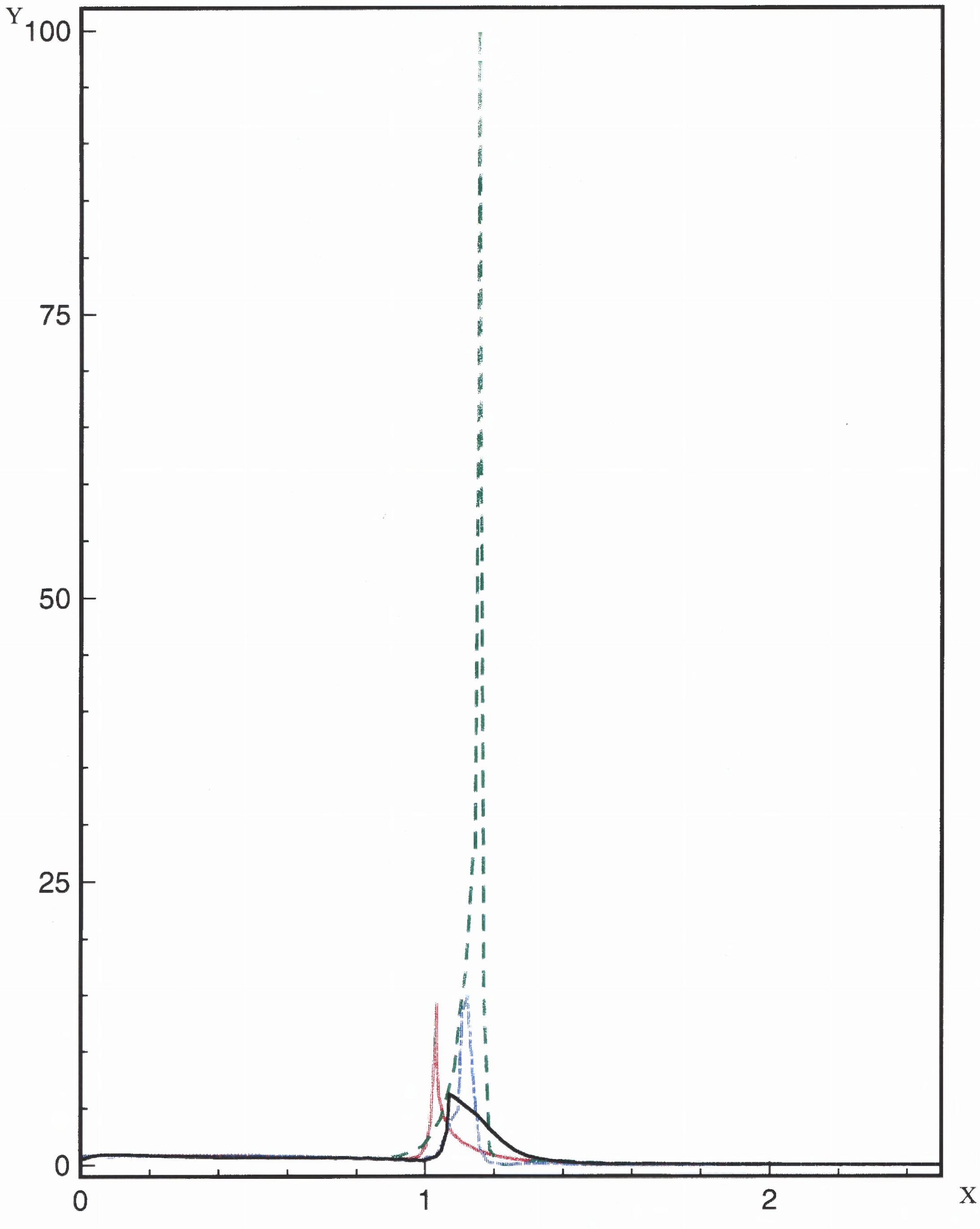

Figure 24. Free-surface kinetic energy as a function of horizontal position x for the following Reynolds and Froude numbers, and at the following times: (1) Re = 100, Fr = 1.125 at t = 3.57 (blue dashdot line),
(2) Re = 500, Fr = 1.125 at t = 3.10 (green dashed line), (3) Re = 1000, Fr = 1.125 at t = 3.196 (red solid line), and (4) Re = 2000, Fr = 1.125 at t = 3.082 (black dotted line).

APPENDIX A

DERIVATION OF EQUATIONS (2.6) AND (2.7)

Here, we consider curvilinear coordinates (ξ,η) and physical-space coordinates (x,y). We assume that there is a unique, single-valued relationship between the coordinates (ξ,η) and (x,y), which can be written as

$$\xi = \xi(x,y), \qquad \eta = \eta(x,y) \tag{A-1}$$

or

$$x = x(\xi,\eta), \qquad y = y(\xi,\eta). \tag{A-2}$$

J denotes the Jacobian matrix, that is

$$J = \frac{D(x,y)}{D(\xi,\eta)} = \begin{vmatrix} x_\xi & x_\eta \\ y_\xi & y_\eta \end{vmatrix}, \tag{A-3}$$

We now set

$$J^* = \frac{D(\xi,\eta)}{D(x,y)} \tag{A-4}$$

such that

$$J \cdot J^* = 1 \tag{A-5}$$

From Equation (A-1), we can write the following equations

$$\left.\begin{aligned} \xi_x x_\xi + \xi_y y_\xi &= 1 \\ \eta_x x_\xi + \eta_y y_\xi &= 0 \end{aligned}\right\} \tag{A-6}$$

$$\left.\begin{aligned} \xi_x x_\eta + \xi_y y_\eta &= 0 \\ \eta_x x_\eta + \eta_y y_\eta &= 1 \end{aligned}\right\} \tag{A-7}$$

which imply

$$x_\xi = \frac{1}{J^*}\begin{vmatrix} 1 & \xi_y \\ 0 & \eta_y \end{vmatrix} = \frac{\eta_y}{J^*},$$

and

$$y_\xi = -\frac{\eta_x}{J^*}, \quad x_\eta = -\frac{\xi_y}{J^*} \quad \text{and} \quad y_\eta = \frac{\xi_x}{J^*}.$$

We thus obtain

$$\xi_x = \frac{1}{J} y_\eta, \quad \xi_y = -\frac{1}{J} x_\eta, \quad \eta_x = -\frac{1}{J} y_\xi, \quad \eta_y = \frac{1}{J} x_\xi. \tag{A-8}$$

We now consider the conservative form of the x-component of the momentum equation

$$\frac{\partial u}{\partial t} + \frac{\partial (u)^2}{\partial x} + \frac{\partial (uv)}{\partial y} = -\frac{\partial p}{\partial x} + \frac{1}{Re}\left(\frac{\partial^2 u}{\partial x^2} + \frac{\partial^2 u}{\partial y^2}\right) \tag{2.4}$$

and express each of its terms in curvilinear coordinates, i.e.

$$\frac{\partial (u^2)}{\partial x} = (u^2)_\xi \xi_x + (u^2)_\eta \eta_x J$$

$$= (u^2)_\xi y_\eta J^* + (u^2)_\eta (-y_\xi J^*)$$

$$= [y_\eta (u^2)_\xi - y_\xi (u^2)_\eta]/J,$$

$$\frac{\partial (uv)}{\partial y} = (uv)_\xi \xi_y + (uv)_\eta \eta_y$$

$$= [-x_\eta (uv)_\xi + x_\xi (uv)_\eta]/J,$$

$$\frac{\partial p}{\partial x} = p_\xi \xi_x + p_\eta \eta_x$$

$$= (y_\eta p_\xi - y_\xi p_\eta)/J\,,$$

$$\frac{\partial u}{\partial x} = u_\xi \xi_x + u_\eta \eta_x\,,$$

$$\frac{\partial^2 u}{\partial x^2} = \frac{\partial}{\partial x}(u_\xi \xi_x + u_\eta \eta_x)$$

$$= u_{\xi\xi}\xi_x^2 + u_{\xi\eta}\xi_x\eta_x + u_\xi \xi_{xx} + u_{\xi\eta}\xi_x\eta_x + u_{\eta\eta}\eta_x^2 + u_\eta \eta_{xx}$$

$$\frac{\partial^2 u}{\partial y^2} = \frac{\partial}{\partial y}(u_\xi \xi_y + u_\eta \eta_y)$$

$$= u_{\xi\xi}\xi_y^2 + u_{\xi\eta}\xi_y\eta_y + u_\xi \xi_{yy} + u_{\xi\eta}\xi_y\eta_y + u_{\eta\eta}\eta_y^2 + u_\eta \eta_{yy}\,.$$

Regrouping the two terms contributing to the viscous force, we obtain

$$\frac{\partial^2 u}{\partial x^2} + \frac{\partial^2 u}{\partial y^2} = (\xi_x^2 + \xi_y^2)u_{\xi\xi} + 2(\xi_x\eta_x + \xi_y\eta_y)u_{\xi\eta} + (\eta_x^2 + \eta_y^2)u_{\eta\eta}$$

$$+ (\xi_{xx} + \xi_{yy})u_\xi + (\eta_{xx} + \eta_{yy})u_\eta\,.$$

Since

$$\xi_x^2 = y_\eta^2 / J^2\,, \qquad \xi_y^2 = (-x_\eta J^*)^2 = x_\eta^2 / J^2\,, \qquad \text{etc.}$$

and

$$\xi_{xx} + \xi_{yy} = (\xi_x^2 + \xi_y^2)P^*(\xi,\eta) \tag{3.12}$$

$$\eta_{xx} + \eta_{yy} = (\eta_x^2 + \eta_y^2)Q^*(\xi,\eta) \tag{3.13}$$

$$\left.\begin{aligned} \alpha &= x_\eta^2 + y_\eta^2 \\ \beta &= x_\xi x_\eta + y_\xi y_\eta \\ \gamma &= x_\xi^2 + y_\xi^2 \end{aligned}\right\} \tag{2.8}$$

$$\left.\begin{array}{l}\sigma^* = \gamma Q^*(\xi,\eta) \\ \tau^* = \alpha P^*(\xi,\eta)\end{array}\right\}, \tag{2.9}$$

we can write the viscous term as follows.

$$\frac{\partial^2 u}{\partial x^2}+\frac{\partial^2 u}{\partial y^2} = (y_\eta^2+x_\eta^2)u_{\xi\xi}/J^2 + 2(-y_\xi y_\eta - x_\xi x_\eta)u_{\xi\eta}/J^2 + (y_\xi^2+x_\xi^2)u_{\eta\eta}/J^2$$

$$+(\xi_x^2+\xi_y^2)P^*(\xi,\eta)u_\xi + (\eta_x^2+\eta_y^2)Q^*(\xi,\eta)u_\eta$$

$$=(y_\eta^2+x_\eta^2)u_{\xi\xi}/J^2 + 2(-y_\xi y_\eta - x_\xi x_\eta)u_{\xi\eta}/J^2 + (y_\xi^2+x_\xi^2)u_{\eta\eta}/J^2$$

$$+(y_\eta^2+x_\eta^2)P^*(\xi,\eta)u_\xi/J^2 + (x_\xi^2+y_\xi^2)Q^*(\xi,\eta)u_\eta/J^2$$

$$=(\alpha u_{\xi\xi} - 2\beta u_{\xi\eta} + \gamma u_{\eta\eta} + \tau^* u_\xi + \sigma^* u_\eta)/J^2 .$$

Similarly, the time derivative term can be expanded

$$u_t\big|_{in(\xi,\eta)} = u_t\big|_{in(x,y)} + u_x x_t + u_y y_t$$

$$= u_t\big|_{in(x,y)} + (u_\xi \xi_x + u_\eta \eta_x)x_t + (u_\xi \xi_y + u_\eta \eta_y)y_t$$

$$= u_t\big|_{in(x,y)} + (y_\eta u_\xi - y_\xi u_\eta)x_t/J + (x_\xi u_\eta - x_\eta u_\xi)y_t/J .$$

This implies

$$u_t\big|_{in(x,y)} = u_t\big|_{in(\xi,\eta)} - x_t(y_\eta u_\xi - y_\xi u_\eta)/J - y_t(x_\xi u_\eta - x_\eta u_\xi)/J .$$

We thus deduce the expression of the x-component of the momentum equation in curvilinear coordinates, or Equation (2.4), that is

$$u_t - x_t(y_\eta u_\xi - y_\xi u_\eta)/J - y_t(x_\xi u_\eta - x_\eta u_\xi)/J$$

$$+[y_\eta(u^2)_\xi - y_\xi(u^2)_\eta]/J + [x_\xi(uv)_\eta - x_\eta(uv)_\xi]/J + (y_\eta p_\xi - y_\xi p_\eta)/J$$

$$= (\alpha u_{\xi\xi} - 2\beta u_{\xi\eta} + \gamma u_{\eta\eta} + \sigma^* u_\eta + \tau^* u_\xi) / \mathrm{Re} J^2 . \tag{2.6}$$

Similarly, we express the y-component of the momentum equation, i.e.

$$\frac{\partial v}{\partial t} + \frac{\partial (uv)}{\partial x} + \frac{\partial (v)^2}{\partial y} = -\frac{\partial p}{\partial y} + \frac{1}{R}\left(\frac{\partial^2 v}{\partial x^2} + \frac{\partial^2 v}{\partial y^2}\right) \tag{2.5}$$

in curvilinear coordinates and obtain Equation (2.7)

$$v_t - x_t (y_\eta v_\xi - y_\xi v_\eta)/J - y_t (x_\xi v_\eta - x_\eta v_\xi)/J$$

$$+ [y_\eta (uv)_\xi - y_\xi (uv)_\eta]/J + [x_\xi (v^2)_\eta - x_\eta (v^2)_\xi]/J + (x_\xi p_\eta - x_\eta p_\xi)/J$$

$$= (\alpha v_{\xi\xi} - 2\beta v_{\xi\eta} + \gamma v_{\eta\eta} + \sigma^* v_\eta + \tau^* v_\xi) / \mathrm{Re} J^2 . \tag{2.7}$$

APPENDIX B

DERIVATION OF THE EQUATIONS TO DETERMINE THE PHYSICAL-SPACE COORDINATES

As mentioned above, the relation between the curvilinear coordinates (ξ, η) and the physical-space coordinates (x, y) is defined in the present work by Poisson equations

$$\xi_{xx} + \xi_{yy} = (\xi_x^2 + \xi_y^2) P^*(\xi, \eta) \tag{3.12}$$

$$\eta_{xx} + \eta_{yy} = (\eta_x^2 + \eta_y^2) Q^*(\xi, \eta) . \tag{3.13}$$

Since the expression of the Jacobian matrix is

$$J = \frac{D(x,y)}{D(\xi,\eta)} = \begin{vmatrix} x_\xi & x_\eta \\ y_\xi & y_\eta \end{vmatrix} = x_\xi y_\eta - x_\eta y_\xi , \tag{A-3}$$

with

$$\xi_x = \frac{1}{J} y_\eta , \qquad \xi_y = -\frac{1}{J} x_\eta , \qquad \eta_x = -\frac{1}{J} y_\xi , \qquad \eta_y = \frac{1}{J} x_\xi , \tag{A-8}$$

we obtain the second derivative of ξ with respect to x as follows.

$$\begin{aligned}
\xi_{xx} &= (\frac{1}{J} y_\eta)_\xi \xi_x + (\frac{1}{J} y_\eta)_\eta \eta_x \\
&= \frac{1}{J} y_{\xi\eta} \xi_x - \frac{1}{J^2} J_\xi y_\eta \xi_x + \frac{1}{J} y_{\eta\eta} \eta_x - \frac{1}{J^2} J_\eta y_\eta \eta_x \\
&= \frac{1}{J} y_{\xi\eta} \cdot \frac{1}{J} y_\eta - \frac{1}{J^2} (x_{\xi\xi} y_\eta + x_\xi y_{\xi\eta} - x_{\xi\eta} y_\xi - x_\eta y_{\xi\xi}) y_\eta \cdot \frac{1}{J} y_\eta \\
&\quad + \frac{1}{J} y_{\eta\eta} \cdot (-\frac{1}{J} y_\xi) - \frac{1}{J^2} (x_{\xi\eta} y_\eta + x_\xi y_{\eta\eta} - x_{\eta\eta} y_\xi - x_\eta y_{\xi\eta}) y_\eta \cdot (-\frac{1}{J} y_\xi) \\
&= \frac{1}{J^3} y_{\xi\eta} y_\eta (J - x_\xi y_\eta) - \frac{1}{J^3} (x_{\xi\xi} y_\eta^3 - x_{\xi\eta} y_\xi y_\eta^2 - x_\eta y_\eta^2 y_{\xi\xi})
\end{aligned}$$

$$+\frac{1}{J^3}y_{\eta\eta}y_\xi\cdot(-J+x_\xi y_\eta)+\frac{1}{J^3}(x_{\xi\eta}y_\xi y_\eta^2-x_{\eta\eta}y_\xi^2 y_\eta-x_\eta y_\xi y_\eta y_{\xi\eta})$$

$$=\frac{1}{J^3}(-y_\eta^3 x_{\xi\xi}+2y_\xi y_\eta^2 x_{\xi\eta}-y_\xi^2 y_\eta x_{\eta\eta}+x_\eta y_\eta^2 y_{\xi\xi}-2x_\eta y_\xi y_\eta y_{\xi\eta}+x_\eta y_\xi^2 y_{\eta\eta}),$$

(B-1)

Similarly, the manipulation of the second derivative of ξ with respect to y gives

$$\xi_{yy}=\frac{1}{J^3}(-x_\eta^2 y_\eta x_{\xi\xi}+2x_\xi x_\eta y_\eta x_{\xi\eta}-x_\xi^2 y_\eta x_{\eta\eta}+x_\eta^3 y_{\xi\xi}-2x_\xi x_\eta^2 y_{\xi\eta}+x_\xi^2 x_\eta y_{\eta\eta}).$$

(B-2)

Likewise, we obtain the second derivatives of η with respect to x and y:

$$\eta_{xx}=\frac{1}{J^3}(y_\xi y_\eta^2 x_{\xi\xi}-2y_\xi^2 y_\eta x_{\xi\eta}+y_\xi^3 x_{\eta\eta}-x_\xi y_\eta^2 y_{\xi\xi}+2x_\xi y_\xi y_\eta y_{\xi\eta}-x_\xi y_\xi^2 y_{\eta\eta})$$

(B-3)

$$\eta_{yy}=\frac{1}{J^3}(x_\eta^2 y_\xi x_{\xi\xi}-2x_\xi x_\eta y_\xi x_{\xi\eta}+x_\xi^2 y_\xi x_{\eta\eta}-x_\xi x_\eta^2 y_{\xi\xi}+2x_\xi^2 x_\eta y_{\xi\eta}-x_\xi^3 y_{\eta\eta}).$$

(B-4)

Taking into account the identities

$$\xi_x^2=\frac{1}{J^2}y_\eta^2 \quad \text{(B-5)}$$

$$\xi_y^2=\frac{1}{J^2}x_\eta^2 \quad \text{(B-6)}$$

$$\eta_x^2=\frac{1}{J^2}y_\xi^2 \quad \text{(B-7)}$$

$$\eta_y^2 = \frac{1}{J^2} x_\xi^2 , \tag{B-8}$$

and denoting A and B the following quantities

$$\mathrm{A} = \alpha x_{\xi\xi} - 2\beta x_{\xi\eta} + \gamma x_{\eta\eta} \tag{B-9}$$

$$\mathrm{B} = \alpha y_{\xi\xi} - 2\beta y_{\xi\eta} + \gamma y_{\eta\eta} , \tag{B-10}$$

Equations (3.12) and (3.13) become

$$\begin{cases} -\dfrac{y_\eta}{J^3}\mathrm{A} + \dfrac{x_\eta}{J^3}\mathrm{B} = \dfrac{1}{J^2}(x_\eta^2 + y_\eta^2)P^* = \dfrac{1}{J^2}\alpha P^* \\ \dfrac{y_\xi}{J^3}\mathrm{A} - \dfrac{x_\xi}{J^3}\mathrm{B} = \dfrac{1}{J^2}(x_\xi^2 + y_\xi^2)Q^* = \dfrac{1}{J^2}\gamma Q^* \end{cases} \tag{B-11}$$

Solving (B-11) leads to

$$\mathrm{A} = -(\alpha P^* x_\xi + \gamma Q^* x_\eta) \tag{B-12}$$

$$\mathrm{B} = -(\alpha P^* y_\xi + \gamma Q^* y_\eta) , \tag{B-13}$$

that is

$$\alpha x_{\xi\xi} - 2\beta x_{\xi\eta} + \gamma x_{\eta\eta} + \alpha P^* x_\xi + \gamma Q^* x_\eta = 0 , \tag{B-14}$$

$$\alpha y_{\xi\xi} - 2\beta y_{\xi\eta} + \gamma y_{\eta\eta} + \alpha P^* y_\xi + \gamma Q^* y_\eta = 0 , \tag{B-15}$$

which are precisely Equations (3.2) and (3.3) mentioned in the text .

APPENDIX C

THE BOUNDARY CONDITIONS FOR FREE-SURFACE FLOW DERIVATIONS OF EQUATIONS (2.14), (2.15) AND (2.16)

Equations (2.11), (2.12)

In order to obtain the free-surface velocity boundary condition, continuity of stress is required. Neglecting the viscous stresses of the atmosphere, the non-dimensional stress at the free-surface can be written as

$$t_i = -(p - \frac{Y}{Fr^2})n_i + \frac{1}{Re}(\frac{\partial u_i}{\partial x_j} + \frac{\partial u_j}{\partial x_i})n_j = -p_s n_i \tag{C-1}$$

where

n_i --- unit normal vector,

p_s --- atmospheric pressure,

p --- flow free-surface pressure,

$i, j = 1,2$ in 2D.

This implies

$$\frac{1}{Re}(\frac{\partial u_i}{\partial x_j} + \frac{\partial u_j}{\partial x_i})n_j = (p - \frac{Y}{Fr^2} - p_s)n_i \tag{C-2}$$

which can be written in the form of the two equations

$$\frac{1}{Re}(\frac{\partial u}{\partial x} + \frac{\partial u}{\partial x})n_1 + \frac{1}{Re}(\frac{\partial u}{\partial y} + \frac{\partial v}{\partial x})n_2 = (p - \frac{Y}{Fr^2} - p_s)n_1$$

$$\frac{1}{Re}(\frac{\partial v}{\partial x} + \frac{\partial u}{\partial y})n_1 + \frac{1}{Re}(\frac{\partial v}{\partial y} + \frac{\partial v}{\partial y})n_2 = (p - \frac{Y}{Fr^2} - p_s)n_2 \ ,$$

or,

$$\frac{2}{Re}\frac{\partial u}{\partial x}n_1 + \frac{1}{Re}(\frac{\partial u}{\partial y} + \frac{\partial v}{\partial x})n_2 = (p - \frac{Y}{Fr^2} - p_s)n_1 \tag{C-3}$$

$$\frac{1}{Re}(\frac{\partial v}{\partial x} + \frac{\partial u}{\partial y})n_1 + \frac{2}{Re}\frac{\partial v}{\partial y}n_2 = (p - \frac{Y}{Fr^2} - p_s)n_2 \tag{C-4}$$

Equations (C-3) and (C-4) can also be written as

$$(p - \frac{Y}{Fr^2} - p_s - \frac{2}{Re}\frac{\partial u}{\partial x})\frac{n_1}{n_2} - \frac{1}{Re}(\frac{\partial u}{\partial y} + \frac{\partial v}{\partial x}) = 0 \tag{C-5}$$

$$(p - \frac{Y}{Fr^2} - p_s - \frac{2}{Re}\frac{\partial v}{\partial y}) - \frac{1}{Re}(\frac{\partial v}{\partial x} + \frac{\partial u}{\partial y})\frac{n_1}{n_2} = 0\,. \tag{C-6}$$

Assuming that the atmospheric pressure is zero, i.e. $p_s = 0$, Equations (C-5) and (C-6) become

$$(p - \frac{Y}{Fr^2} - \frac{2}{Re}\frac{\partial u}{\partial x})\frac{n_1}{n_2} - \frac{1}{Re}(\frac{\partial u}{\partial y} + \frac{\partial v}{\partial x}) = 0 \tag{C-7}$$

$$(p - \frac{Y}{Fr^2} - \frac{2}{Re}\frac{\partial v}{\partial y}) - \frac{1}{Re}(\frac{\partial v}{\partial x} + \frac{\partial u}{\partial y})\frac{n_1}{n_2} = 0 \tag{C-8}$$

Considering that

$$\frac{\partial Y}{\partial x} = -\frac{n_1}{n_2},$$

Equations (C-7) and (C-8) give

$$(p - \frac{Y}{Fr^2} - \frac{2}{Re}\frac{\partial u}{\partial x})\frac{\partial Y}{\partial x} + \frac{1}{Re}(\frac{\partial u}{\partial y} + \frac{\partial v}{\partial x}) = 0 \tag{2.11}$$

and

$$(p - \frac{Y}{Fr^2} - \frac{2}{Re}\frac{\partial v}{\partial y}) + \frac{1}{Re}(\frac{\partial v}{\partial x} + \frac{\partial u}{\partial y})\frac{\partial Y}{\partial x} = 0 \qquad (2.12)$$

These are precisely Equations (2.11) and (2.12) we mentioned earlier.

Equations (2.14), (2.15) and (2.16)

We now consider the free-surface boundary condition for the velocity components u and v, that is derive Equations (2.14) and (2.15). In this derivation, all the equations are written at the free-surface, i.e. at $y = Y$.

Because the unit normal to an η-line is

$$\vec{n}^{(\eta)} = \frac{\text{sgn}(J)}{\sqrt{\gamma}}(-y_\xi \vec{i} + x_\xi \vec{j}), \qquad (C-9)$$

we can write

$$\frac{n_1}{n_2} = [-\text{sgn}(J)(\frac{y_\xi}{\sqrt{\gamma}})]/[\text{sgn}(J)(\frac{x_\xi}{\sqrt{\gamma}})] = -\frac{y_\xi}{x_\xi}. \qquad (C-10)$$

Substituting the identity (C-10) into equations (C-7) and (C-8), we obtain

$$(p - \frac{Y}{Fr^2} - \frac{2}{Re}\frac{\partial u}{\partial x})(-\frac{y_\xi}{x_\xi}) - \frac{1}{Re}(\frac{\partial u}{\partial y} + \frac{\partial v}{\partial x}) = 0$$

and

$$(p - \frac{Y}{Fr^2} - \frac{2}{Re}\frac{\partial v}{\partial y}) - \frac{1}{Re}(\frac{\partial v}{\partial x} + \frac{\partial u}{\partial y})(-\frac{y_\xi}{x_\xi}) = 0,$$

which can be rewritten as

$$(p - \frac{Y}{Fr^2} - \frac{2}{Re}u_x)y_\xi + \frac{1}{Re}(u_y + v_x)x_\xi = 0 \qquad (C-11)$$

and

$$(p-\frac{Y}{Fr^2}-\frac{2}{Re}v_y)x_\xi+\frac{1}{Re}(v_x+u_y)y_\xi=0\,. \tag{C-12}$$

In the computational domain, Equation (C-11) gives

$$(p-\frac{Y}{Fr^2})y_\xi-\frac{2}{Re}(y_\eta u_\xi-y_\xi u_\eta)y_\xi/J$$

$$+\frac{1}{Re}(x_\xi u_\eta-x_\eta u_\xi+y_\eta v_\xi-y_\xi v_\eta)x_\xi/J=0\,,$$

and therefore,

$$-2(y_\eta u_\xi-y_\xi u_\eta)y_\xi+(x_\xi u_\eta-x_\eta u_\xi+y_\eta v_\xi-y_\xi v_\eta)x_\xi$$

$$=-ReJ(p-\frac{Y}{Fr^2})y_\xi\,.$$

This implies

$$2(y_\xi y_\eta+x_\xi x_\eta)u_\xi-(2y_\xi^2+x_\xi^2)u_\eta-x_\xi y_\eta v_\xi-x_\xi y_\xi v_\eta=ReJy_\xi(p-\frac{Y}{Fr^2})\,. \tag{C-13}$$

Equation $(C-13)+x_\eta y_\xi v_\xi-x_\eta y_\xi v_\xi \Rightarrow$

$$y_\xi(y_\eta u_\xi-y_\xi u_\eta+x_\xi v_\eta-x_\eta v_\xi)+\beta u_\xi-\gamma u_\eta-Jv_\xi=ReJy_\xi(p-\frac{Y}{Fr^2})\,. \tag{C-14}$$

From the continuity equation, we can write

$$y_\eta u_\xi-y_\xi u_\eta+x_\xi v_\eta-x_\eta v_\xi=0\,.$$

Taking this into account, Equation (C-14) becomes

$$\beta u_\xi-\gamma u_\eta-Jv_\xi=ReJy_\xi(p-\frac{Y}{Fr^2})\,.$$

This leads to the expression of the u-component of the velocity at the free-surface in the computational domain

$$u_\eta = \frac{1}{\gamma}[\beta u_\xi - Jv_\xi - ReJy_\xi(p - \frac{Y}{Fr^2})]. \tag{2.14}$$

Similarly, the v-component of the velocity at the free-surface can be obtained from Equation (C-12):

$$v_\eta = \frac{1}{\gamma}[Ju_\xi + \beta v_\xi + ReJx_\xi(p - \frac{Y}{Fr^2})]. \tag{2.15}$$

Multiplying Equation (2.15) by x_ξ and Equation (2.14) by y_ξ leads to the final expression of the pressure.

$$x_\xi \cdot (2.15) - y_\xi \cdot (2.14) \quad \Rightarrow$$

$$x_\xi v_\eta - y_\xi u_\eta = \frac{1}{\gamma}[J(u_\xi x_\xi + v_\xi y_\xi) + \beta(v_\xi x_\xi - u_\xi y_\xi) + ReJ(x_\xi^2 + y_\xi^2)(p - \frac{Y}{Fr^2})].$$

Since $x_\xi^2 + y_\xi^2 = \gamma$, we finally obtain

$$p = \frac{Y}{Fr^2} + \frac{1}{ReJ}(x_\xi v_\eta - y_\xi u_\eta) - \frac{1}{\gamma Re}[u_\xi x_\xi + v_\xi y_\xi + \frac{\beta}{J}(v_\xi x_\xi - u_\xi y_\xi)]. \tag{2.16}$$

APPENDIX D

DERIVATION OF THE INITIAL INDUCED VELOCITY OF THE POINT VORTEX.

For a single line vortex as shown, we have

$$u = \frac{\Gamma}{4\pi} \int \frac{Y - y}{r^3} ds$$

$$v = \frac{\Gamma}{4\pi} \int \frac{X - x}{r^3} ds$$

$$w = 0 .$$

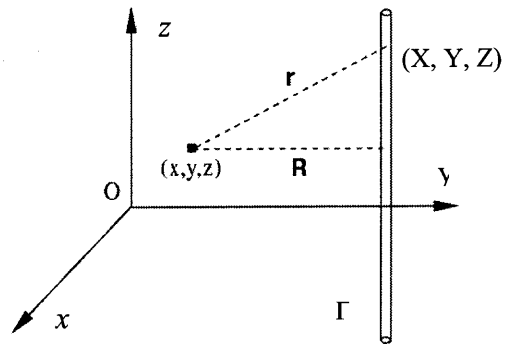

Letting $R^2 = (x - X)^2 + (y - Y)^2$ and

integrating the above equations,

we obtain

$$u = -\frac{\Gamma}{2\pi} \frac{y - Y}{R^2} \qquad \text{(D-1)}$$

$$v = \frac{\Gamma}{2\pi} \frac{x - X}{R^2} \qquad \text{(D-2)}$$

and

$$w = 0 \qquad \text{(D-3)}$$

We now restrict ourselves to the two-dimensional situation. In this case, Equations (D-1) and (D-2) imply that the velocity induced by the k-th point vortex at any arbitrary point $M(x, y)$ can be written as

$$\begin{cases} u_k(M) = -\dfrac{\Gamma_k}{2\pi}\dfrac{y-Y_k}{R_k^2} \\ v_k(M) = \dfrac{\Gamma_k}{2\pi}\dfrac{x-X_k}{R_k^2} \end{cases} \tag{D-4}$$

in the case where there are n simultaneously existing point vortices, the induced velocity at the point $M(x,y)$ becomes

$$\begin{cases} u(M) = \sum_{k=1}^{n} u_k(M) = \sum_{k=1}^{n}\left(-\dfrac{\Gamma_k}{2\pi}\dfrac{y-Y_k}{R_k^2}\right) \\ v(M) = \sum_{k=1}^{n} v_k(M) = \sum_{k=1}^{n}\left(\dfrac{\Gamma_k}{2\pi}\dfrac{x-X_k}{R_k^2}\right) \end{cases} \tag{D-5}$$

If the point M coincides with the location of the j-th point vortex, then, according to Equation (D-5), the remaining $n-1$ point vortices will make this point vortex move with the induced velocity

$$\begin{cases} u_j = \dfrac{dX_j}{dt} = -\sum_{\substack{k=1 \\ k\neq j}}^{n}\dfrac{\Gamma_k}{2\pi}\dfrac{Y_j-Y_k}{R_{jk}^2} \\ v_j = \dfrac{dY_j}{dt} = \sum_{\substack{k=1 \\ k\neq j}}^{n}\dfrac{\Gamma_k}{2\pi}\dfrac{X_j-X_k}{R_{jk}^2} \end{cases} \quad (j = 1,2,\ldots,n) \tag{D-6}$$

Choosing $n=2$ in Equation (D-6), we obtain the velocity of the point vortex due to the two point vortex's interaction as follows:

$$\begin{cases} u_1 = \dfrac{dX_1}{dt} = -\dfrac{\Gamma_2}{2\pi}\dfrac{Y_1-Y_2}{R_{12}^2} \\ v_1 = \dfrac{dY_1}{dt} = \dfrac{\Gamma_2}{2\pi}\dfrac{X_1-X_2}{R_{12}^2} \end{cases} \tag{D-7}$$

and

$$\begin{cases} u_2 = \dfrac{dX_2}{dt} = -\dfrac{\Gamma_1}{2\pi}\dfrac{Y_2 - Y_1}{R_{21}^2} \\ v_2 = \dfrac{dY_2}{dt} = \dfrac{\Gamma_1}{2\pi}\dfrac{X_2 - X_1}{R_{21}^2} \end{cases} \tag{D-8}$$

For the particular case where $Y_1 = Y_2$ and $\Gamma_1 = -\Gamma_2 = -\Gamma$, we can write

$$\begin{cases} u_1 = u_2 = 0 \\ v_1 = v_2 = \dfrac{\Gamma}{2\pi}\dfrac{X_1 - X_2}{R^2} \end{cases} \tag{D-9}$$

This illustrates why the vortex pair moves vertically towards the free-surface.

We now show that it is possible to calculate the initial speed of the vortex pair from our initial condition (given by Equations (D-1) and (D-2)):

$$\begin{cases} u_1 = \dfrac{dX_1}{dt} = -\dfrac{\Gamma_3}{2\pi}\dfrac{Y_1 - Y_3}{R_{13}^2} - \dfrac{\Gamma_4}{2\pi}\dfrac{Y_1 - Y_4}{R_{14}^2} = \dfrac{\Gamma}{2\pi}(Y_1 - Y_3)(\dfrac{1}{R_{13}^2} - \dfrac{1}{R_{14}^2}) \\ v_1 = \dfrac{dY_1}{dt} = \dfrac{\Gamma_2}{2\pi}\dfrac{X_1 - X_2}{R_{12}^2} + \dfrac{\Gamma_3}{2\pi}\dfrac{X_1 - X_3}{R_{13}^2} = \dfrac{\Gamma}{2\pi}(X_1 - X_2)(\dfrac{1}{R_{12}^2} - \dfrac{1}{R_{13}^2}) \end{cases} . \tag{D-10}$$

REFERENCES

1. Batchelor, G. K., 1967, *An Introduction to Fluid Dynamics*. p. 336, Cambridge University Press.

2. Barker, S. J. & Crow, S. C., 1977, The motion of two-dimensional vortex pairs in a ground effect. *J. Fluid Mech.* 82, 659-671.

3. Bernal, L. P., Hirsa, A., Kwon, J. T. & Willmarth, W. W., 1989, On the interaction of vortex rings and pairs with a free surface for varying amounts of surface active agent *Phys. Fluids* A 1, 2001-2004.

4. Borue, V., Orszag, S. A. & Staroselsky, I. 1995 Interaction of surface waves with turbulence: direct numerical simulations of turbulent open-channel flow. *J. Fluid Mech.* 286,1-23.

5. Bradshaw, P. & Kon, Y. M. 1981 A note on Poisson's equation for pressure in a turbulent flow. *Phys. Fluids* 24, 777.

6. Couder, Y. & Basdevant, C., 1986, Experimental and numerical study of vortex couples in two-dimensional flows. *J. Fluid Mech.* 173, 225-251.

7. Chorin, A. J., "The numerical solution of the Navier-stokes equations for incompressible fluid," AEC Research and Development Report No. NYO-1480-82, New York Univ., Nov. 1967.

8. Dagan, A., 1989, Pseudo-spectral and asymptotic sensitivity investigation of counter- rotating vortices. *Computers & Fluids* 17, 509-525.

9. Fletcher, A. J., "Computational Techniques for Fluid Dynamics", Second Edition, Springer-Verlag, 1991.

10. Fish, S., 1990, Ambient free surface wave modification by a submerged vortex pair. David Taylor Research Center Rep. DTRC-90/004.

11. Floryan, J. M. & Rasmcssen, H. 1989, Numerical methods for viscous flows with moving boundaries. *Appl. Mech. Rev.* 42, 323-341.

12. Handler, R. A., Swean, T. F. Jr., Leighton, R. I. & Swearingen, J. D. 1991 Length scales of turbulence near a free surface. *AIAA Paper* 91-1775.

13. Handler, R. A., Swean, T. F. Jr., Leighton, R. I. & Swearingen, J. D. 1993 Length scales and the energy balance for turbulence near a free surface. *AIAA J.* 31, 1998-2007.

14. Harvey, J. K. & Perry, F. J. 1971, Flow field produced by trailing vortices in the vicinity of the ground. *AIAA J.* 9, 1659-1660.

15. Kochin, N. E., Kibel, I. A., & Roze, N. V. , 1964, *Theoretical Hydromechanics*. Wiley.

16. Lam, K. & Banerjee, S. 1988 Investigation of turbulent flow bounded by a wall and a free surface. In *Fundamentals of Gas-Liquid Flows* (ed. E. Michaelides & M. P. Sharma), pp. 29-38. ASME.

17. Lamb, H. 1932 *Hydrodynamics*, 6th edn. Cambridge University Press.

18. Leighton, R. I., Swean, T. F. & Handler, R. A. 1991 Interaction of vorticity with a free surface in turbulent open channel flow. *AIAA Paper* 91-0236.

19. Lugt, H. J., 1983, Vortex Flow in Nature and Technology. Wiley-Interscience.

20. Marcus, D. L., and Berger, S. A., 1989 The Interaction Between a Counter-Rotating Vortex Pair in Vertical Ascent and a Free Surface, *Physics of Fluids*, A-1, Vol. 12, pp. 1988-2000.

21. Nguyen Duc, J. & Sommeria, J., 1988, Experimental characterization of steady two-dimensional vortex couples. *J. Fluid Mech.* 192, 175-192.

22. Ohring, S. & Lugt, H. J., 1989, Two counter-rotating vortices approaching a free surface in a viscous fluid. David Taylor Research Center Rep. DTRC-89/013.

23. Ohring, S. & Lugt, H. J. 1991, Interaction of a viscous vortex pair with a free surface. *J. Fluid Mech.* 227, 47-70.

24. Orlandi, P., 1990, Vortex dipole rebound from a wall. *Phys. Fluids* A 2, 1429-1436. Peace, A. J. & Riley, N., 1983, A viscous vortex pair in ground effect. *J. Fluid Mech.* 129, 409-426.

25. Pan, Y. & Banerjee, S. 1995 A numerical study of free-surface turbulence in channel flow. *Phys. Fluids* 7, 1649-1664.

26. Perot, B. & Moin, P. 1995 Shear-free turbulent boundary layers. Part 1. Physical insights into near-wall turbulence. *J. Fluid Mech.* 295, 199-227.

27. Saffman, P. G., 1979, The approach of a vortex pair to a plane surface in inviscid fluid. *J. Fluid Mech.* 92, 497-503.

28. Sarpkaya, T., 1986, Trailing-vortex wakes on the free surface. *In Proc. 16th Symp. On Naval Hydrodynamics*, Berkeley, pp. 38-50.

29. Sarpkaya, T., Elnitsky, J. & Leeker, R. E., 1988, Wake of a vortex pair on the free surface. In *Proc, 17th Symp. on Naval Hydrodynamics*, pp. 47-54. Washington: Naval Studies Board.

30. Sarpkaya, T. & Henderson, D. O., 1984, Surface disturbances due to trailing vortices. Naval Postgraduate School, Monterey. California, Rep. NPS-69-84-004.

31. Saffman, P. G. 1979 The approach of a vortex pair to a plane surface in inviscid fluid. *J. Fluid Mech*. 92, 497-503.

32. Scott, J. C. 1975 The preparation of water for surface clean fluid mechanics. *J. Fluid Mech.* 69, 339-351.

33. Scott, J. C. 1982 Flow beneath a stagnant film on water: the Reynolds ridge. *J. Fluid Mech.* 116, 283-296.

34. Shen, L., Zhang, X., Yue, D. K. P., & Triantafyllou, G. S. 1999 The surface layer for free-surface turbulent flows. *J. Fluid Mech.* 386, 167-212.

35. Swean, T. F., Jr., Leighton, R. I., Handler, R. A. & Swearingen, J. D. 1991 Turbulence modeling near the free surface in open channel flow. *AIAA Paper* 91-0613.

36. Tennekes, H. & Lumley, J. L., *A First Course in Turbulence*, The MIT press, Cambridge, Massachusetts, and London, England.

37. Telste, J. G., 1989, Potential flow about two counter-rotating vortices approaching a free surface. *J. Fluid Mech.* 201, 259-278.

38. Thompson, J. F. & Shanks, S. P., 1977, Numerical solution of the Navier-Stokes equations for 2D surface hydrofoils. Mississippi State University Rep. MSSU-EIRS-AES-77-4.

39. Tryggvason, G., Deformation of a Free Surface as a Result of Vortical flows, *Physics of Fluids* 31, 1988, pp.955-957.

40. Tyvand, A., Motion of a vortex near a free surface, *J. Fluid Mech.* 1991, vol.225, pp. 673-686.

41. Walker, D. T, Leighton, R. I. & Garza-Rios, L. O. 1996 Shear-free turbulence near a flat free surface. *J. Fluid Mech.* 320, 19-51.

42. Walker, J. D. A., Smith, C. R., Cerra, A. W. & Doligalski, T. L., 1987, The impact of a vortex ring on a wall. J. Fluid Mech. 181, 99-140.

43. Weigand, A. and Gharib, M., Turbulent Vortex Ring/Free Surface Interaction, FED-Vol. 181, Free-Surface Turbulence, ASME 1994.

44. Willmarth, W. W., Tryggvason, G., Hirsa, A. & Yu, D., 1989, Vortex pair generation and interaction with a free surface. *Phys. Fluids* A 1, 170-172.

45. Yamada, H. & Honda, Y. 1989 Wall vortex induced by and moving with a confined vortex pair. *Phys. Fluids* A 1, 1280-1282.

46. Yu, D. & Tryggvason G. 1990 The free-surface signature of unsteady, two-dimensional vortex flows. *J. Fluid Mech*, 218, 547-572.